Characteristics of Strong Ground Motions and Fragility Curves of Buildings during the 2011 off the Pacific coast of Tohoku Earthquake

by

Hao Wu

A thesis submitted in partial fulfillment of the requirements
for the degree of

Doctor of Engineering

in the

Aichi Institute of Technology

September, 2013

Abstract

The 2011 off the Pacific coast of Tohoku Earthquake was an Mw9.0 mega thrust interplate earthquake. It was the largest earthquake in Japan and the fifth largest one in the world since seismology records began in 1900. The coastal area, especially in the Iwate and Miyagi Prefecture, was subjected to great damage by huge tsunami. Many villages and towns including the buildings and people were entirely flushed away. Except the damage caused by tsunami, the ground shaking during this earthquake also brought about the damage to buildings over the east Tohoku and Kanto regions. It is essential to investigate the relationships between building damage ratios and ground motion characteristics, i.e., fragility curves, during this earthquake, which will be useful for disaster mitigation and damage assessment in future disastrous earthquakes.

First, the relationships between building damage ratios in administrative districts, such as city, town and village (*shi, cho, mura in Japanese*), and observed ground motions during the 2011 Tohoku Earthquake are investigated. Three different damage ratios, i.e., total collapse ratio (TCR), collapse ratio (CR) and damage ratio (DR), are related to four ground motions indices, i.e., peak ground acceleration (PGA), peak ground velocity (PGV), JMA instrumental seismic intensity (I_{JMA}) and spectral ratio (SI), respectively.

However, the ground motions are sensitive to geological conditions in administrative districts, it suggests that the ground motions should be estimated within a smaller administrative unit, e.g., subdistrict (subdivision of an administrative unit), to be related to the damage ratios. Therefore, in this study, the method of estimating ground motions during the mainshock is proposed and verified. This method indicates that the ground motions at the sites where no strong motion stations were installed can be estimated with the underground velocity structures identified from the microtremor H/V spectral ratios and the ground motions at the bedrock during the mainshock calculated by use of the short-period source model.

The underground velocity structures at damaged sites are identified from microtremor H/V spectral ratios. By applying the proposed method, the ground motions in subdistricts are estimated with the identified underground velocity structures and the bedrock motions during the mainshock. Fragility curves based on the damage ratios and estimated ground motions in the subdistricts of Osaki and Kurihara cities, and Wakuya town, Miyagi prefecture during the mainshock are then investigated.

Acknowledgements

I would like to show my gratitude to Prof. Yingzheng Guo, the supervisor of my master course in Southeast University of China. Under his recommendation and encouragement, I obtained this precious opportunity to pursue my doctoral degree in Japan.

I am grateful to Prof. Kazuaki Masaki, the supervisor of my doctoral course. He always enlightened me whenever I encountered problems, encouraged and helped me out if I felt frustration. What's more important was that he often spared some time to tell me some interesting things more than what I can anticipate. His extensive knowledge about everything greatly expanded my horizons.

I would like to show my great gratitude to Adjunct Prof. Kojiro Irikura who have been supervising my study in the past three years. He enlightened me in the study step by step. His deep insight into seismology wiped out all of my confusions. His persistent enthusiasm and prudent attitude towards academics moved me so much that I doubted whether I could keep the same energy as him if I were at his age.

I would like to thank Dr. Susumu Kurahashi for many important discussions about my study and some meaningful conversations on how to be a qualified doctor. Also, he was always able to help me solve any problems I came across in the programming. He even generously sent me some of his programs from which I learned a lot.

I also would like to thank Assistant Prof. Xin Wang. She helped me prepare many kinds of files in order to obtain the visa before I came to Japan. She always patiently explained to me whenever I asked questions before she transferred to Tohoku University in Japan.

I also thank postdoctoral fellow Koichiro Saguchi in Tokyo Institute of Technology for teaching me the simulated annealing algorithm and sending his code to me.

Thanks should also be owed to Mr. Yoshida in Kurihara city hall and Mr. Irinoda in Osaki city hall for their corporations on providing important damage data of buildings in each subdistrict.

The NIED organization is appreciated for providing the strong-motion data, together with the PS-logging data at K-NET and KiK-net stations. The Generic Mapping Tools (Wessel and Smith, 1998) are also appreciated for plotting some figures in this thesis.

At last, but it is not the least important, I would like to show my great gratitude to my family. I am proud of being born in such a family that the hard working spirit passed on from my grandparents and parents convinces me to overcome any difficulties and step forward bravely.

Contents

List of Figures

List of Tables

Chapter 1

Introduction

1.1 Background

On March 11, 2011, an Mw 9.0 mega thrust interplate earthquake, named as "the 2011 off the Pacific coast of Tohoku Earthquake" by Japan Meteorological Agency (JMA) occurred. It was the largest in Japan and the fifth largest in the world since seismology records began in 1900. The hypocenter was situated in the depth of approximately 30 km. The epicenter was approximately 70 km east of the Oshika Peninsula of Tohoku. Fault region was very wide that the length was as long as 400 km extending from Sanriku-Oki to Boso peninsula, and the width was about 200 km. The highest acceleration and maximum instrumental seismic intensity observed at Tsukidate station in the Kurihara city were 2933 gal and 7 (largest scale issued by JMA) respectively. Powerful tsunami triggered by this earthquake flushed away considerable villages and towns in some coastal cities along the east coast of Japan. Plenty of buildings, infrastructures and lifelines were subjected to heavy damage. In addition, the leakage of radioactive from the Fukushima Daiichi Nuclear Power Station operated by Tokyo Electric Power Company in the Fukushima Prefecture which was caused by tsunami indirectly intensified the tragedy of the aftermath. Oil tanks in some petrochemical industrial complex (Nishi, 2012) fell down due to the strong motion and caused fire or explosion.

According to the Fire and Disaster Management Agency (FDMA, 2012) as of March 11, 2012, as many as 16,278 people lost their lives, and 2,994 people were missed, as well as 6,179 people injured. Meanwhile, 129,198 residential buildings were totally collapsed, 254,238 residential buildings were partially collapsed (or half-collapsed), and 715,192 residential buildings were partially damaged.

On the other hand, more than 1200 strong motion stations, e.g., K-NET (Kinoshita, 1998) and KiK-net (Aoi, 2000) stations which have been installed since 1995 Kobe earthquake and were operated by National Research Institute for Earth Science and Disaster Prevention (NIED, 2012) recorded the ground motions during this earthquake. Therefore, it is urgent and necessary to clarify the relationship between buildings damage ratios and characteristics of ground motions, i.e., fragility curve, which can be used to investigate the damage assessment in the future for the same scale of earthquake.

1.2 Review of previous studies about fragility curves since the Hyogo-ken Nanbu Earthquake in 1995

Fragility curves describe the probability of exceeding a specific damage level as a function of a ground motion index. They can be used to assess the damage risk of buildings from potential earthquakes and predict the economic loss for the future earthquakes.

In Japan, extensive studies on fragility curves were implemented during the Hyogo-ken Nanbu Earthquake (the 1995 Kobe earthquake hereafter) in 1995. Instant and comprehensive on-site investigation about the buildings damage data were conducted by many organizations (e.g. AIJ, 1996, BRI, 1996, Kinki brach of AIJ, 1995) shortly after that destructive earthquake. These damage data were also classfied by structural type and construction age and were arranged into digital disk (BRI, 1996). These plentiful damage data greatly facilitated the studies on fragility curves and were helpful for estimation of ground motions.

Hayashi, Miyakoshi and Tamura (1997), Hayashi, Miyakoshi, Tamura and Kawase (1997) examined the relationship between damage ratio and peak ground velocities estimated with a two dimensional finite element method, for residential buildings. They then applied the fragility curves to estimate the distribution of peak ground velocities where the damage data were known. Finally they constructed the fragility curves in consideration of different stories and utilities of buildings. Miyakoshi et al. (1997) calculated the damage ratios based on the statistical damage data conducted by different organizations and constructed the fragility curves with estimated peak ground velocities by Hayashi, Miyakoshi, Tamura and Kawase (1997). They revealed the difference of fragility curves due to different damage data source and proved that the building damage ratio is influenced by construction age and structural type. Hasegawa (1998) suggested the damage prediction should not be confined to independent administration unit but implemented as one unified unit in the perspective of a wide area. He proposed one method to estimate the number of buildings classified by construction age on the basis of statistical data in meshes, then calculated the damage ratio in studied area, and finally obtained the fragility curves by relating the damage ratio with peak ground velocities. Yamaguchi and Yamazaki (1999) constructed the fragility curves with observed strong motion data, but the damage data were not classified by structural type or construction age. They further applied the constructed fragility curves to estimate the distribution of ground motion in the Hanshin area. Murao (1999) used the similar method to estimate the ground motions in Nada Ward, Kobe City and then constructed the fragility curves in consideration of different construction age and structural type. Yamaguchi and Yamazaki (2000) investigated the fragility curves with the damage data collected by Nishinomiya City and estimated ground motions.

Except Kobe earthquake in Japan, Tong et al. (1994) collected the number of damaged households in five earthquakes from 1978 Miyagi-Oki earthquake to 1993 Hokkaido-Nansei-Oki earthquake. They studied the relationship between damage ratio and spectral intensity (SI), peak ground acceleration (PGA). They pointed out that PGA may not be a good ground motion index to be related with damage ratio. Midorikawa et al. (2011) examined the fragility curves with damage data of seven earthquakes from 2003 Northern Miyagi Earthquake to 2008 Iwate-hokubu Earthquake. They suggested that the instrumental seismic intensity by JMA (I_{JMA}) and PGV have a better correlation with damage ratio than PGA.

The fragility curves are also studied during other destructive earthquakes occurred around the circum-Pacific seismic belt except in Japan. During the Chi-Chi Earthquake, Taiwan in 1999, Miyakoshi and Hayashi (2000) constructed the fragility curves, and then compared the difference with 1995 Kobe Earthquake. They concluded that seismic performance of reinforced concrete buildings in Taiwan was lower than that in Kobe. Wu, Yih-Min et al. (2002) constructed the fragility curves with PGA and PGV. They suggested PGV was a better index for seismic damage assessment and developed the rapid reporting system based on the relationship between damage ratio and PGV. For the Wenchuan Earthquake in 2008, Sichuan Province in China, Wang et al. (2011) constructed the fragility curves based on ten strong motion records and collapse ratios in the stricken districts near the source fault zone.

1.3 Outline of this thesis

Shortly after the 2011 Tohoku Earthquake, Fire and Disaster Management Agency published the damage data classified by three damage levels, i.e., totally collapsed, partially collapsed (or half-collapsed) and partially damaged, in each administrative district every few months with the proceeding of survey. These damage data, although were not classified by structural type and construction age, can be used to calculate the damage ratio, provided the total number of sound buildings in each district is known. The calculated damage ratios can then be related with the characteristics of ground motions in those districts where strong motion stations are installed. In general, only a couple of stations are installed in each district. The uncertainties of ground motions with the geological condition suggests that it is preferable to discuss the relationship in a smaller administrative unit. Supposing that the damage data in some subdistricts can be obtained, it is necessary to investigate the method to estimate the ground motions at the damaged sites where the strong-motion stations were not installed during the mainshock. Therefore, the thesis is composed of the following chapters.

Chapter 1 is an introduction about the damage during the mainshock and reviewed the previous studies about fragility curves.

Chapter 2 examines the relationships between building damage ratios in adminstrative districts, such as city, town and village (*shi, cho, mura in Japanese*) and the characteristics of observed ground motions during this earthquake. Damage data classified by three damage levels, i.e., totally collapsed, partially collapsed and partially damaged will be used to calculate the damage ratios, i.e., total collapse ratio, collapse ratio and damage ratio.

Chapter 3 presents a method to estimate ground motions at those sites where no strong motion data were observed during the mainshock by taking the short-period source model and underground velocity structures identified from microtremor H/V spectral ratios into account. First, the effectiveness of identifying underground velocity structures from microtremor H/V spectral ratio will be investigated by comparing the transfer functions estimated with the underground velocity structures identified from microtremor H/V spectral ratio and earthquake H/V spectral ratio. Then this method will be examined by comparing the ground motions estimated from the bedrock motions considering the short-period source model and identified underground velocity structures with the observed ones at some strong-motion stations.

Chapter 4, the proposed method will be applied at the damaged sites of subdistricts in the Osaki and Kurihara cities, and in the Wakuya town, Miyagi prefecture where the building damage data classified by three damage levels in subdistricts can be obtained from the local government. The estimated ground motions during the mainshock will be used to construct the fragility curves based on damage ratios in the subdistricts.

Chapter 5 is the conclusions of this thesis.

Chapter 2

Relationships between damage ratios and observed ground motions in administrative districts of east Tohoku and Kanto regions

For the same level of ground motions within a certain administrative district, e.g., a city, town or village (*shi, cho or mura in Japanese*), the buildings may subject to different kinds of damage, such as no damage, partial damage, partial collapse and total collapse etc.. Therefore, we can investigate the relationships of certain damage ratio with different levels of ground motions in all the damaged administrative districts. During the mainshock, the damage data in the administrative districts classified by three damage levels, i.e., totally collapsed, partially collapsed and partially damaged were published by the FDMA. Ground motion data can be obtained from the NIED. This chapter will clarify the relationships between three different damage ratios, i.e., total collapse ratios (TCRs), collapse ratios (CRs) and damage ratios (DRs) and characteristics of ground motions quantified by four kinds of indices, peak ground acceleration (PGA), peak ground velocity (PGV), JMA instrumental seismic intensity (I_{JMA}) and spectral intensity (SI).

2.1 Data Source used in this study

2.1.1 Building damage data

During this earthquake, buildings in coastal districts were mainly damaged by tsunami over the Tohoku and Kanto areas. At the same time, in the inland districts, numerous buildings were damaged by ground shaking. The building damage statistics, i.e., the numbers of totally collapsed, partially collapsed, and partially damaged buildings in the stricken districts, are obtained from the FDMA (2012). The total numbers of buildings in stricken districts are obtained from the Statistics Bureau and Director-General for Policy Planning of Japan (STAT, 2012). The administrative unit of the stricken districts is city, town, or village (*shi, cho, or mura in Japanese*). According to the FDMA, total collapse denotes buildings whose basic functions have been lost for the residents, i.e., the buildings are totally collapsed, washed away, or buried, or the damage to the buildings cannot be recovered through repair. Partial collapse denotes buildings whose basic functions for residents have been partly lost for the residents, i.e., the buildings can be recovered through repair. Partial damage means that the damage to buildings is not heavier than total and partial collapse, but that the buildings need repair. Slight damage such as cracks on several panes of glass is not classified as partial damage. On the other hand, because our objective is to elucidate damage by ground shaking, districts damaged by tsunami were excluded from the inundation maps provided by the Geospatial Information Authority of Japan (GSI, 2012). At the same time, according to a liquefaction survey report from the Ministry of Land, Infrastructure, Transport and Tourism and the Japanese Geotechnical Society (2011), buildings in districts such as Urayasu city, Chiba city and Katori city are significantly damaged by liquefaction. They are also excluded. On the other hand, some stricken districts in which strong-motion stations have not been installed are included if they satisfy the following two conditions:

- The geology of the stricken districts is similar to that of adjacent stricken districts in which strong-motion stations were installed
- The distance between the building-concentrated street in the stricken district and the strong-motion station in the adjacent stricken district is less than 10 km.

Fig. 2.1 shows all the stricken districts in the six prefectures along the east Pacific coast. The districts in yellow are the stricken ones in which a couple of strong-motion stations were installed. The districts in green are those satisfying the aforementioned two conditions. The districts in gray are excluded as the buildings inside them are thought to be mainly damaged by tsunami. The districts in red are also excluded as the buildings inside them are thought to be mainly affected by liquefaction. The shadowed districts with slashes are those lacking damage statistics.

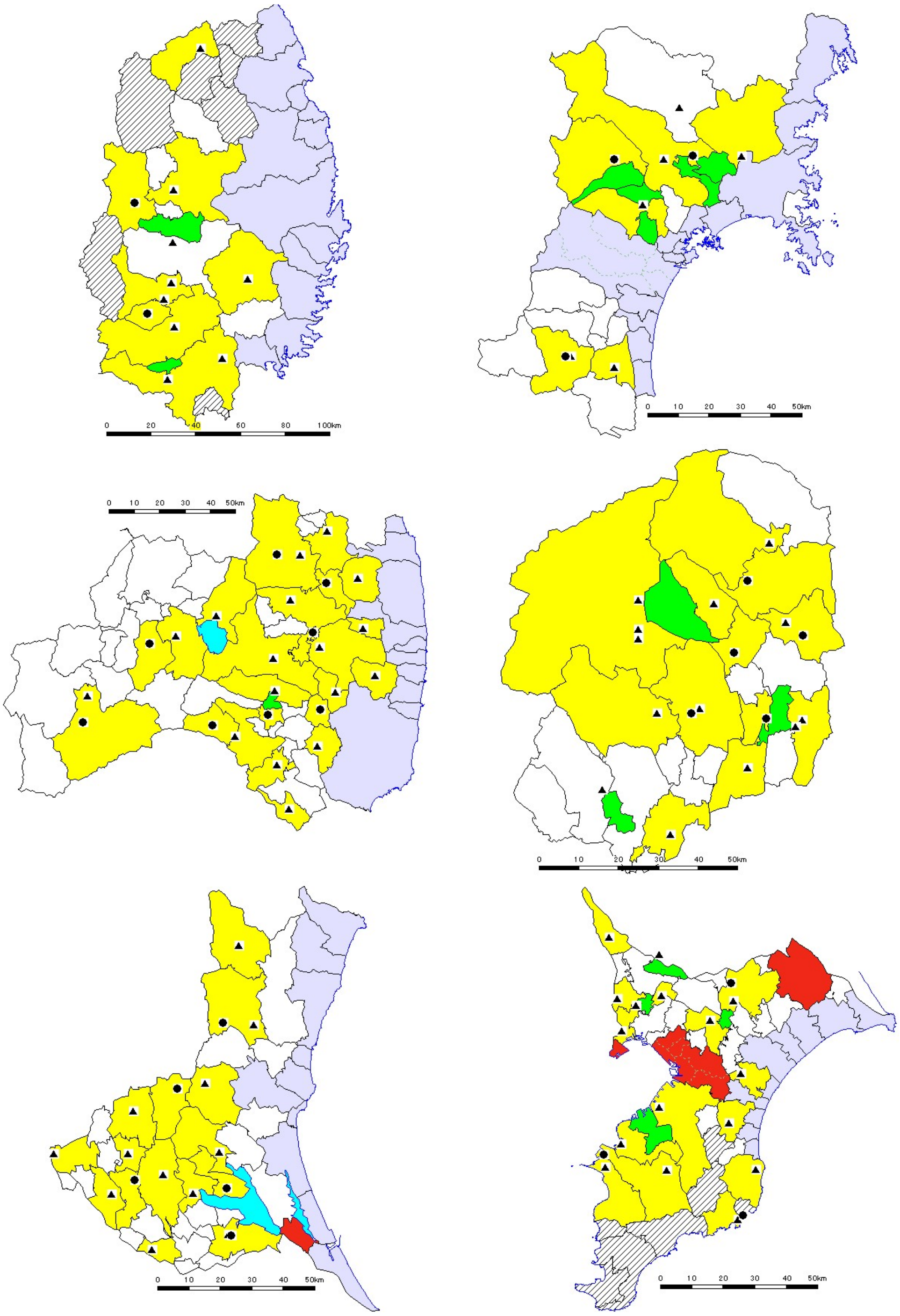

Fig. 2.1 Damaged districts used to calculate TCR, CR and DR in six prefectures. Districts shown with slashes are those in which damage data have not been published by FDMA; districts in yellow are those in which strong-motion stations were installed; districts in green are those in which ground motion data in their adjacent districts are used ; districts in gray are those in which buildings are mainly damaged by tsunami; districts in red are those in which buildings are affected by liquefaction; blank districts are those in which there are no representative ground motion data; cyan areas are lakes; solid triangles and circles denote the positions of K-NET stations and KiK-net stations, respectively. This figure is plotted by KenMap (2011)

2.1.2 Ground motion data

The strong-motion records at the K-NET and KiK-net stations were open to the public soon after this earthquake. In this study, the observation records in K-NET stations and KiK-net stations are used to analyze ground motion characteristics. The locations of the K-NET or KiK-net stations in the stricken districts are shown in Fig. 2.1. The solid triangles represent K-NET stations and the solid circles represent KiK-net stations. For those districts in which there is more than one strong-motion station, the arithmetic average of observed ground motion data at all of the strong-motion stations are taken as the ground motion characteristics for the entire district. In addition, the ground motion record at the Tsukidate station in Kurihara city is not included in the following analysis, as it is reported that the extremely large motion may be caused by partial uplifting of the instrumental foundation (Motosaka and Tsamba, 2011). On the other hand, the stations that were installed on rock and far from densely building-concentrated streets are also excluded regarding the representativeness of ground motions. The location of these stations are confirmed through Google earth.

2.2 Fragility curve based on damage ratios in stricken districts

2.2.1 Definitions of three building damage ratios

Three different building damage ratios, i.e., total collapse ratio (TCR), collapse ratio (CR), and damage ratio (DR) are studied. Each of them is defined as the ratio of number of damaged buildings to total number of buildings in damaged districts. Detailed definitions are given as follows:

$$TCR = A/D \times 100\% \tag{2.1}$$

$$CR = (A+B)/D \times 100\% \tag{2.2}$$

$$DR = (A+B+C)/D \times 100\% \tag{2.3}$$

where

A– the number of totally collapsed buildings in an administrative district;
B– the number of partially collapsed buildings in an administrative district;
C– the number of partially damaged buildings in an administrative district;

D– the total number of buildings regardless of damage and non-damage in an administrative district.

The unit of A, B, C and D may be the number of either households or buildings for a certain administrative district. In the previous studies, the number of households was adopted as the unit of damage data to calculate damage ratios. It might be explained by two reasons. First, the magnitudes of previous earthquake were not so large that the damaged areas were confined to several administrative districts. The number of buildings may be too limited to clarify the relationship between damage ratios and characteristics of ground motions. Second, the total numbers of households were well arranged in each local government and can be easily accessed. However, to the contrast, it may be reasonable to adopt the number of buildings as the unit of damage data, as it reflects the real numbers of damaged buildings due to ground shaking. The number of households is quite different from that of buildings for some those administrative districts with a large amount of apartments or mansions. During the 2011 Tohoku earthquake, the damaged area is so wide that the numbers of households may not reliable at present as the accuracy are affected by the credit of applicants whose buildings suffered damage. The accurate numbers might not be obtained in a couple of years until all of them are confirmed by local government staffs. Fortunately, the FDMA publishes the damage data by the number of buildings in each administrative district. Therefore, the number of buildings is adopted as the unit of damage data in this study. The total number of buildings can be obtained from the Statistics Bureau and Director-General for Policy Planning of Japan.

In addition, the total numbers of buildings in some small districts cannot be obtained from the Statistics Bureau, but the total numbers of households in such districts can be easily found from the homepages of local governments. Fig. 2.2 shows the relationship between the total numbers of buildings and the total numbers of households in the stricken districts where both kinds of data are available. It can be seen that the total number of households has a good linear correlation with the total number of buildings for each district, and the former is almost the same as the latter. This indicates that the total numbers of buildings can be approximately replaced with the total numbers of households in those small districts inside which the total number of households is fewer than 10,000.

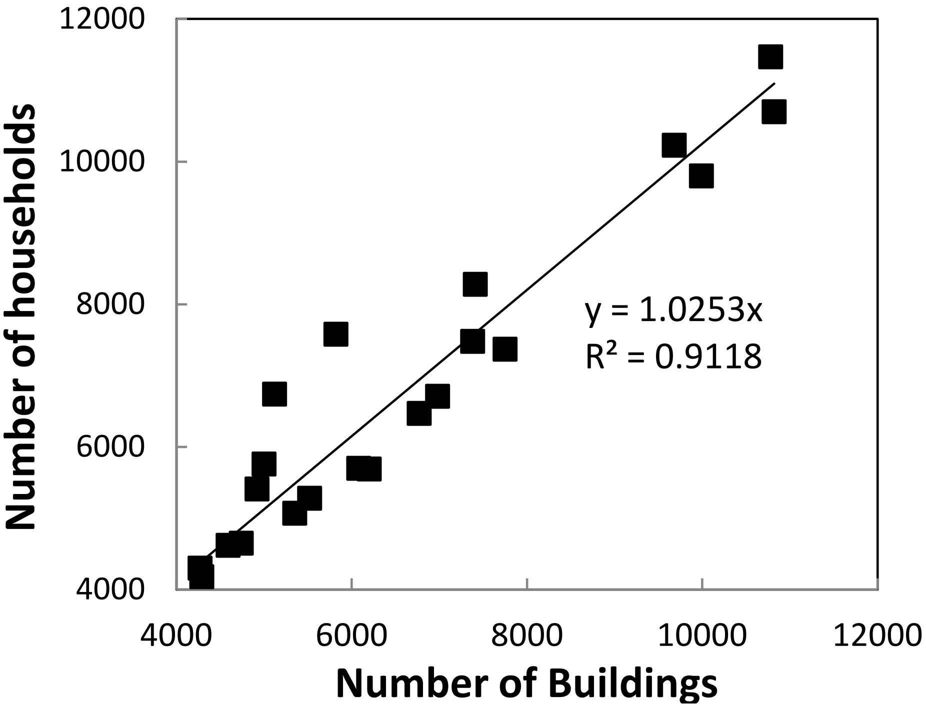

Fig. 2.2 Relationship between number of buildings and number of households

2.2.2 Representativeness of ground motions in stricken districts

As there are only a couple of strong-motion stations installed in an administrative district, it is advisable that the median of the ground motions is used as the representative ground motions for the entire district, if the distribution of ground motions within one district is known. In Japan, J-SHIS (2013) provides the distribution of amplification factors (Fujimoto and Midorikawa, 2006) for the peak ground velocity (PGV) from the layer equivalent to the engineering bedrock (400 m/s shear wave velocity) to ground surface based on the geomorphologic classification (Wakamatsu et al., 2004) all over the Japan. It suggests that we can evaluate the median of PGV by the following equation under the assumption that the PGV on the engineering bedrock of the entire district is the same.

$$(PGV)_m = (PGV)_{b400} \times (ARV)_m = \frac{(PGV)_o}{(ARV)_o} \times (ARV)_m \tag{2.4}$$

where

$(PGV)_m$ is the median PGV for the entire district;

$(PGV)_{b400}$ is the PGV on the engineering bedrock (400 m/s shear wave velocity);

$(PGV)_o$ is the PGV at the observation station;

$(ARV)_m$ is the median amplification factor (ARV) for the entire district;

$(ARV)_o$ is the ARV at the observation station.

We attempt to revise the PGVs at the strong-motion stations to the median PGV for each entire district by Eq. (2.4). Fig. 2.3 shows an example in the Fukushima city including FKSH16 and FKS003 strong-motion stations and Date city including FKS002 strong-motion station northern Fukushima prefecture. It can be seen that the amplification factors (ARVs) in the Fukushima city do not vary significantly, while ARVs take a obvious contrast near the FKS002 station in the Date city. It means that the median of PGV for Fukushima city is approximately the same as the arithmetic average of PGVs at two strong-motion stations, while the median of PGV for Date city will be lower than PGV at FKS002 station which is situated at the edge of large ARV area. Table 2.1 shows the median PGV by applying Eq. (2.4). The result is almost consistent with the our analysis that the median PGV of Date city is about one third of the observed PGV at FKS002. We should not have adopted the same method to obtain the median PGV of each stricken district until we found a big pitfall of this method. We realized that it was more suitable to take the median PGV of the areas within one stricken district where buildings are densely distributed as the representative PGV for the entire stricken district. However, it is difficult to grasp the exact distribution of buildings within a district at present. Generally, many buildings are concentrated in basins, or the warm-colored areas as shown in Fig. 2.3 with high amplification factors, and there are few buildings in hills, or the cold colored areas with low amplification factors. Therefore, the representative ground motions for an entire district might be underestimated if it is revised with the aforementioned method, just as Date city. Eventually, the observed ground motions are assumed to be representative for an entire stricken district, as long as the strong-motion stations are not located on the rock.

Table 2.1 Median of PGV in Fukushima and Date cities, Fukushima prefecture

District	Station	$(PGV)_o$	$(ARV)_o$	$(ARV)_m$	$(PGV)_m$
Fukushima	FKS003	24.5	1.189283		
	FKSH16	25.3	1.107937	0.812485	17.6
Date	FKS002	30.9	1.996663	0.668866	10.3

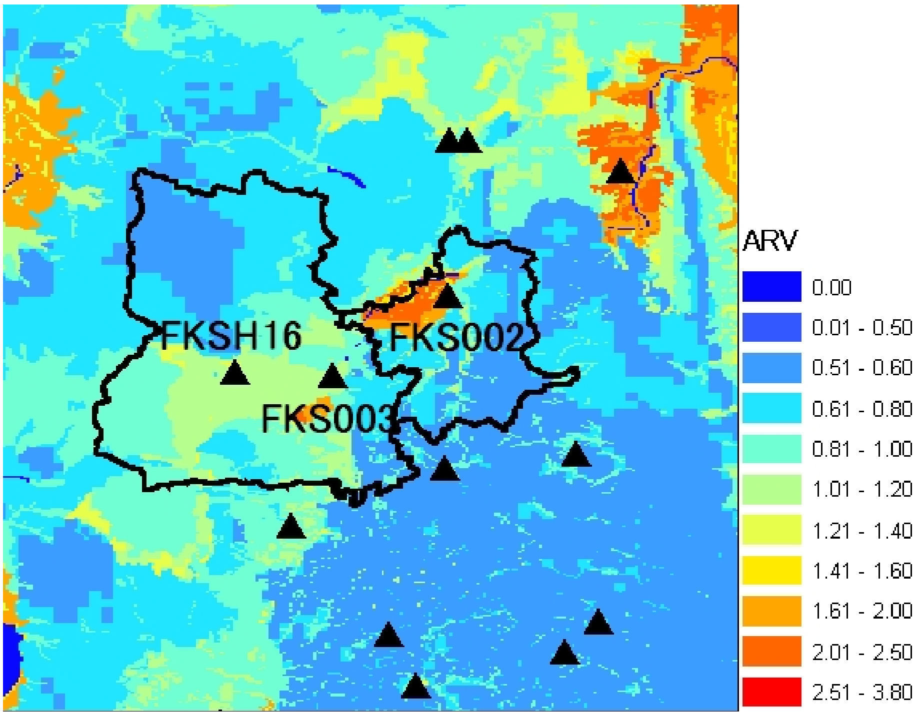

Fig. 2.3 Distribution of amplification factors (ARVs) in Fukushima (left) and Date (right) cities, Fukushima prefecture. Triangles denote the strong-motion stations

2.2.3 Construction of fragility curves based on the damage ratios and observed ground motions in the stricken districts

Fragility curves are constructed to examine the relationship between three kinds of building damage ratios and the ground motion characteristics, which are peak ground acceleration (PGA), peak ground velocity (PGV), Japan Meteorological Agency instrumental seismic intensity (I_{JMA}), and spectral intensity (SI). The damage ratios and the ground motion indices in all the studied administrative districts are listed in the Appendix A.1. The cumulative probability of building damage, $P(x)$, is assumed to be the normal cumulative distribution function, according to Okada and Kagami (1991).

$$P(x) = \Phi((x - \mu)/\sigma) \tag{2.5}$$

where

Φ is the standard normal cumulative distribution function;

x is a variable with respect to ground motion indices, such as I_{JMA}, natural logarithm of PGA, natural logarithm of PGV, or natural logarithm of SI;

μ and σ – the mean and standard deviation of x, they are determined through geometric mean regression method with the normal probability plot method. Fig. 2.4

shows the regression between DR and PGV in order to determine the parameters used to plot the fragility curve. σ is obtained from the reciprocal of slope of the regression equation and μ is obtained from the absolute ratio of intercept and slope of the regression equation.

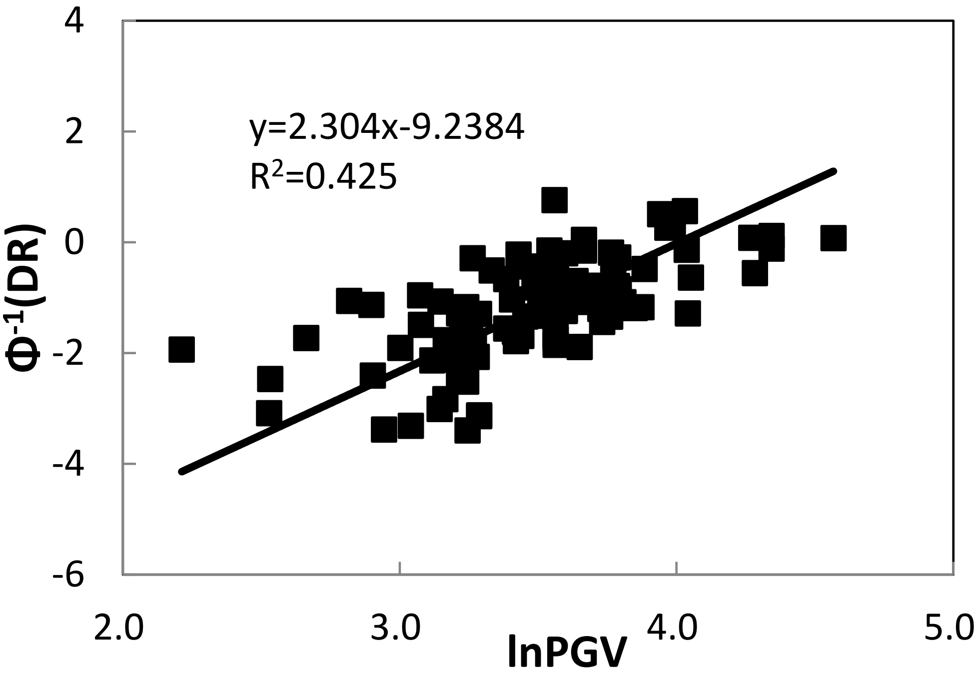

Fig. 2.4 Geometric mean regression between lnPGV and $\Phi^{-1}(DR)$

PGA, PGV, and SI are adopted to be the larger value between the NS and EW components. SI is the integral of the pseudo-velocity response spectrum with a damping ratio averaged over the period range from 0.1 s to 2.5 s, as is shown in Eq. (2.6). I_{JMA} is calculated based on the manual issued by the Japan Meteorological Agency (JMA, 1996).

$$SI(h,T) = \frac{1}{2.5-0.1}\int_{0.1}^{0.5} S_{pv}(h,T)dT \tag{2.6}$$

where

$S_{pv}(h,T)$ is the pseudo-velocity response spectrum for damping ratio h;

h is the damping ratio, h is set to be 0.20, according to Housner (1952);

T is the natural period of buildings.

Fig. 2.5 ∼ Fig. 2.7 show the fragility curves between three kinds of building damage ratios, i.e., TCR, CR, and DR, as well as the ground motion indices, i.e., PGA, PGV, I_{JMA}, and SI. The coefficients of μ and σ, and the determination coefficient R^2 (also referred to the square of correlation coefficient defined as Eq. (2.7)) used to assess the goodness of fit, are given in Table 2.2. Generally, the damage ratios increase with the ground motion indices, which suggests that they have a certain correlation. It can be seen from Table 2.2 that standard deviation between the DRs and any one of the ground motion indices is the smallest, and that corresponding determination coefficient R^2 is the largest among the three kinds of building damage ratios. This suggests that the correlation of ground motion indices with the DRs is the best. Therefore, the focus is put on the relationship between the DRs and the ground motion indices in the following analysis. From the values of R^2, it can be seen that the correlation of I_{JMA} with DR is best among four ground motion indices. Also, the correlation of SI with any kind of the damage ratios is similar to PGV. It can be explained by the well correlation between these two values, as shown in Fig. 2.8, the ratio between SI and PGV is approximately 0.983 which is smaller than 1.18 pointed by Tong et al. (1994). On the other hand, although the correlation of PGA with DR is well, the relatively large standard deviation coefficient and less correlation with TCR and CR suggests that PGA may not a good indicator to be related with damage ratios, which is in agreement with the conclusion of Midorikawa et al. (2011). This can be attributed to the sensitivity of PGAs to the short predominant period characteristics of ground motions. Fig. 2.9 shows the damage data categorized by predominant period determined from the pseudo-velocity response spectra (pSv). It can be seen that damage data with a short predominant period of less than 0.4 s are mostly distributed beneath the fragility curve. That is to say large PGAs with a short predominant period of less than 0.4 s will not cause much damage to buildings. In contrast, the PGVs seem to be insensitive to short periods of less than 0.4 s. Furthermore, both the PGAs and PGVs are not sensitive to longer periods of over 2.0 s which will not cause much damage to buildings.As a result, we conclude that I_{JMA} , SI, PGV have a better correlation with damage ratios than PGA.

$$R^2 = \frac{\left(\sum_{i=1}^{N}(y_i - \bar{y})(f_i - \bar{f})\right)^2}{\sum_{i=1}^{N}(y_i - \bar{y})^2 \sum_{i=1}^{N}(f_i - \bar{f})^2} \tag{2.7}$$

where

y_i and f_i are called the observed and predicted values respectively;

$\bar{y}$ and $\bar{f}$ are the mean value of all observed and predicted values respectively.

However, uncertainty exists for DR versus any one of the four ground motion indices. One of the reasons for this is that the damage data are not classified by the building

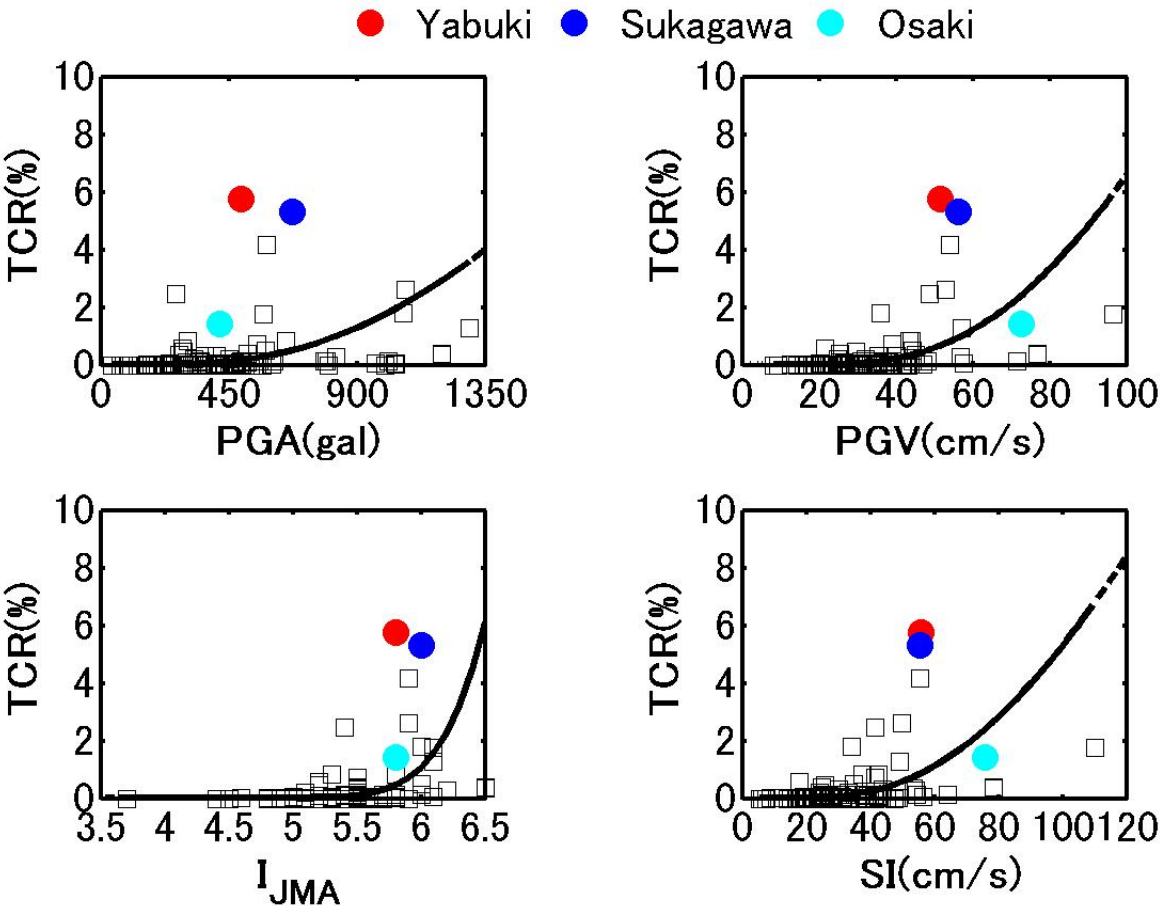

Fig. 2.5 Fragility curve for TCRs in 94 stricken districts

Table 2.2 Parameters about fragility curves of administrative districts

	PGA			PGV			I_{JMA}			SI		
	μ	σ	R^2	μ	σ	R^2	μ	σ	R^2	μ	σ	R^2
TCR	8.703	0.853	0.148	5.637	0.684	0.351	7.520	0.660	0.282	5.843	0.766	0.308
CR	7.720	0.687	0.273	4.679	0.468	0.364	6.668	0.492	0.386	4.783	0.533	0.365
DR	6.738	0.639	0.481	4.009	0.434	0.425	5.971	0.465	0.546	4.030	0.503	0.435

construction date and structural type in each stricken district which are thought to be different from district to district. The different number of the building construction date or structural type in each stricken district can contribute to this uncertainty. Furthermore, the damage data in some districts may include the numbers of damaged buildings not directly caused by ground shaking, such as landslide. However, the uncertainty caused by these factors cannot be resolved unless comprehensive damage data can be obtained. Another reason may be that the representativeness of the ground motions, i.e., the ground motions at the strong-motion station, may not be appropriate for representing the ground motions for an entire stricken district. Take Yabuki town and Sukagawa city in Fukushima prefecture for example. The damage data of these

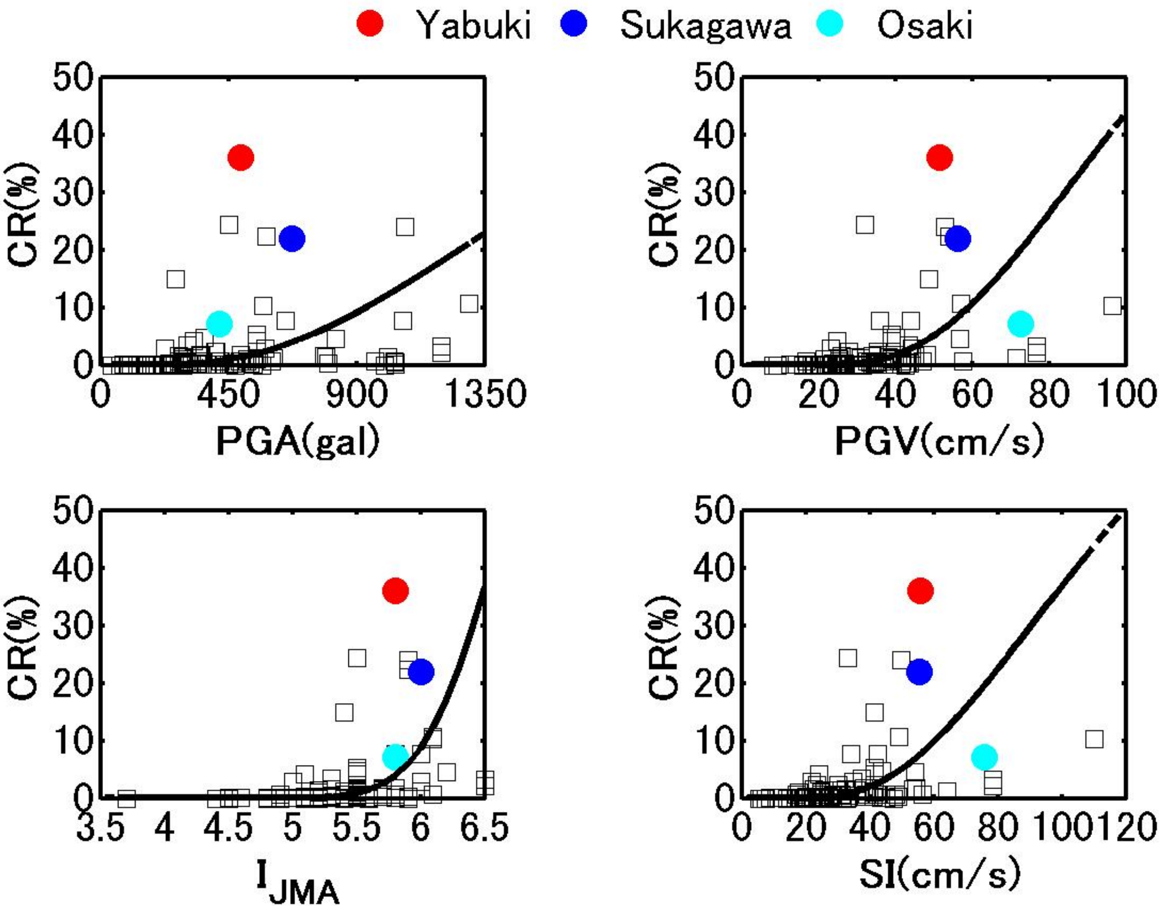

Fig. 2.6 Fragility curve for CRs in 94 stricken districts

two districts are shown with red and blue circles respectively in the Fig. 2.5 ∼ Fig. 2.7. It can be seen that both of these two districts have a relatively low level of ground motions, but the damage ratios are relatively large. According to the field survey by Muraibo et al. (2011), the DR of Ippongi subdistrict where the strong-motion station was installed was lowest among all the subdistricts in the Yabuki town as shown in Table 2.3. It means that the ground motions used at the strong-motion station may underestimate the overall level of ground motions for the entire Yabuki town. In other words, the ground motions at the strong-motion station are not representative for the Yabuki town. During the mainshock, the ground motions at one of the heavy damaged subdistricts, e.g., Yamatouchi subdistrict were estimated by Wu, Hao et al. (2012).The larger estimated ground motions agrees with the above supposition. Another example is Sukagawa city of Fukushima prefecture. We conducted the field survey centered the strong-motion station with a radius of about 500 m. The damage ratio of about 21.6% was also rather lower than the overall damage ratio–71.3%. It might also be explained by the representativeness of ground motions.

To the contrary, high level of ground motions can not account for the low damage

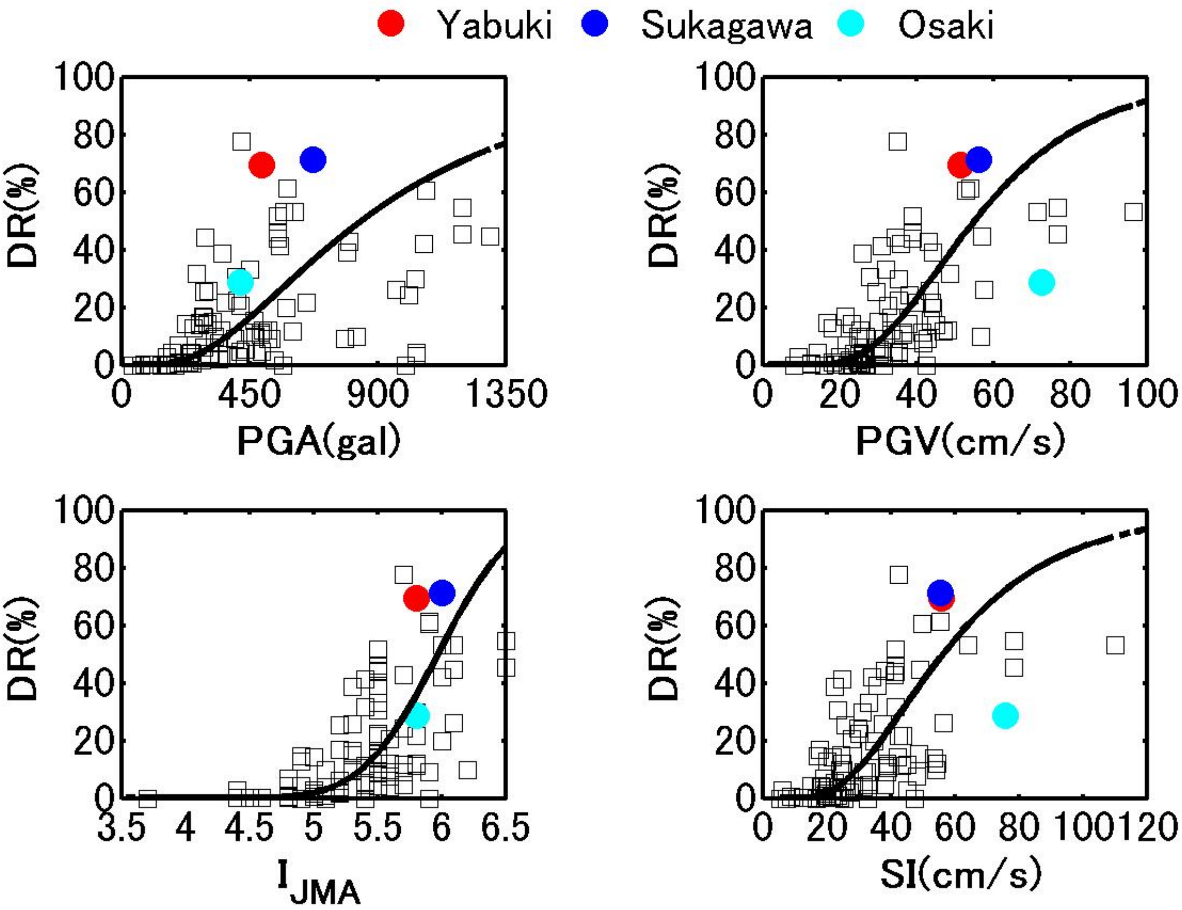

Fig. 2.7 Fragility curve for DRs in 94 stricken districts

Table 2.3 Number of damaged buildings and damage ratios in the subdistricts of Yabuki town, Fukushima prefecture

Subdistrict	Sound	Slight	Minor	Moderate	Heavy	Collapse	Unknown	DR(%)
Tatesaza	22	16	12	0	4	0	0	59.3
Ohmachi	40	38	20	3	3	0	1	61.0
Motomachi	101	73	27	16	14	2	9	54.5
Nakamachi	100	142	58	56	40	4	17	71.9
Shimachi	96	86	17	6	6	3	1	54.9
Yamatouchi	21	15	16	4	14	1	0	70.4
Ippongi	37	32	1	0	0	0	0	47.1

ratios, for instance, Osaki city in Miyagi prefecture. It can be explained from the distribution of amplification factors in Osaki city as shown in Fig. 2.10 that the observed ground motions at high amplification factors area may overestimated the level of ground motions for the entire district. It implies that the representative ground motions should be confined to a smaller administrative unit, such as subdistrict (i.e., subdivision of an administrative unit) shown in Fig. 2.11, which will be examined in chapter 4.

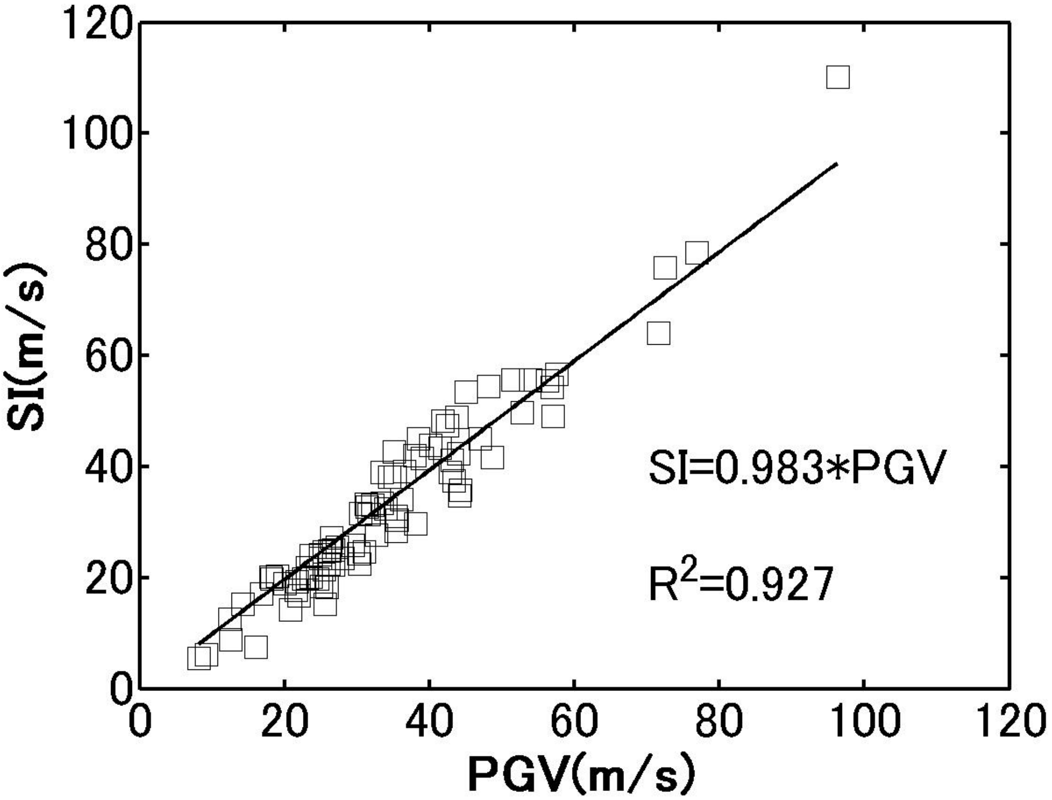

Fig. 2.8 Relationship between SI and PGV for the stricken districts

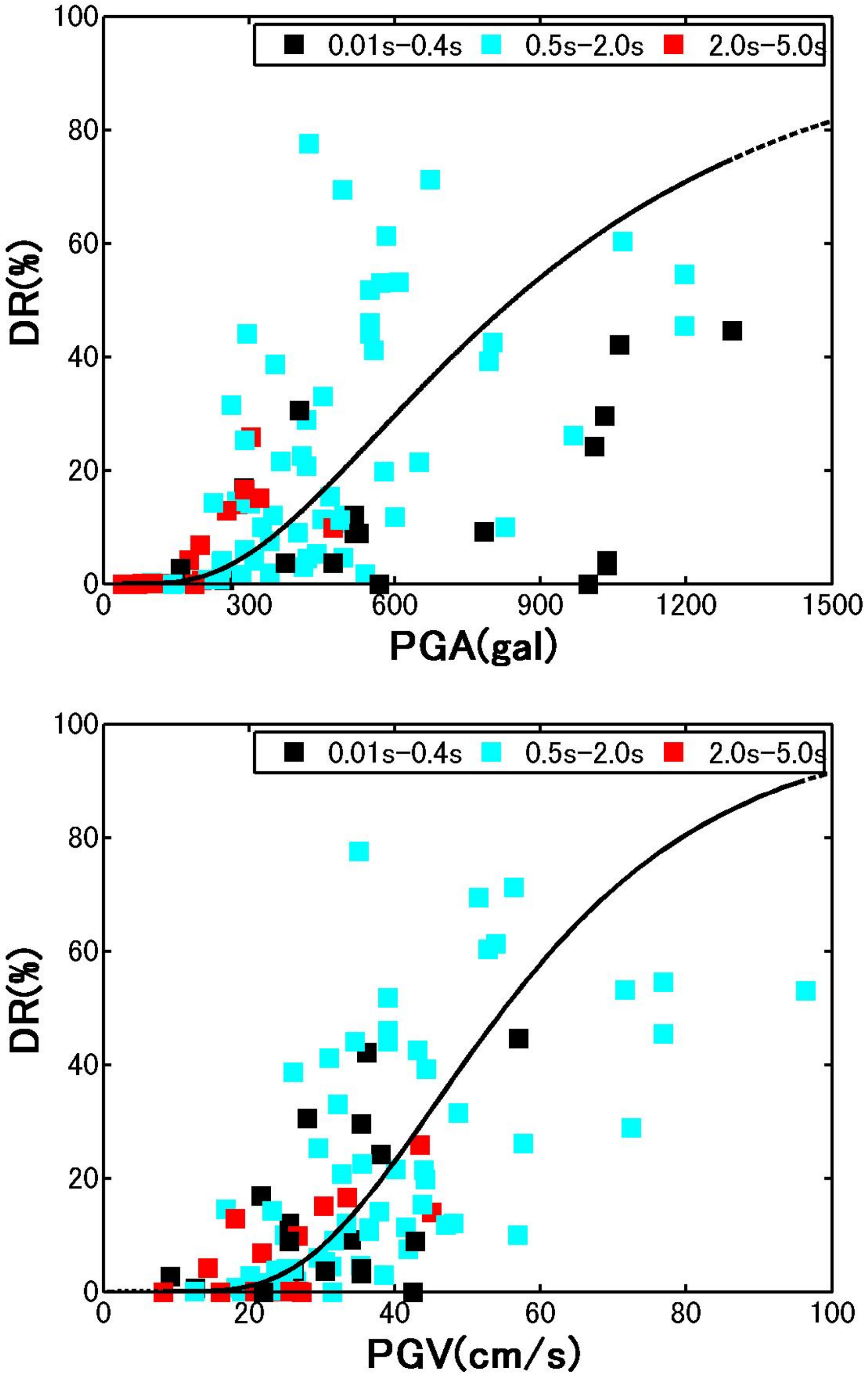

Fig. 2.9 Fragility curves for DR versus PGA and DR versus PGV. Damage data are classified by predominant period of pseudo-velocity response spectrum

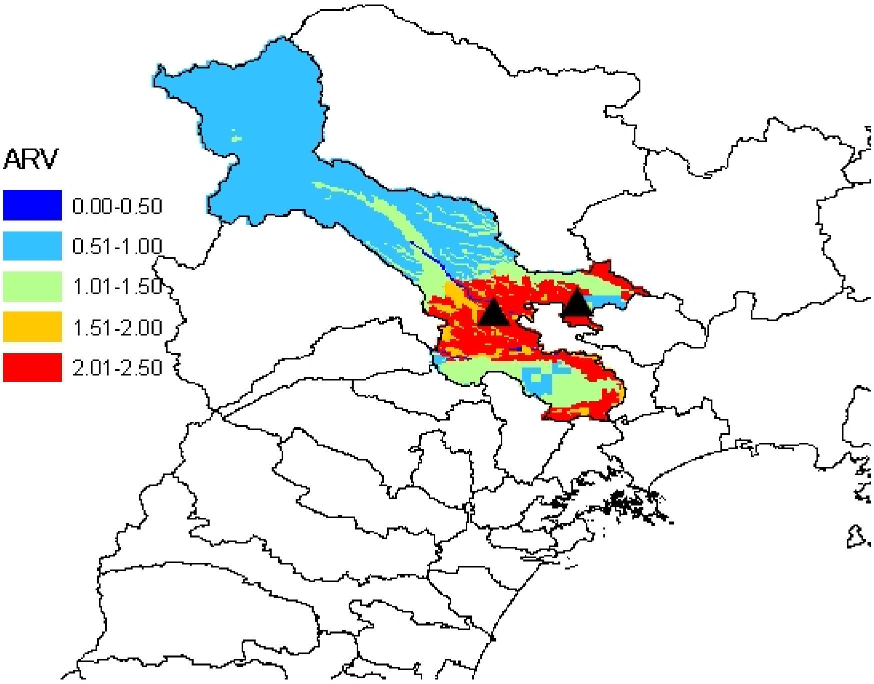

Fig. 2.10 Distribution of amplification factors in the Osaki city, Miyagi prefecture. Two triangles denote the location of strong-motion stations.

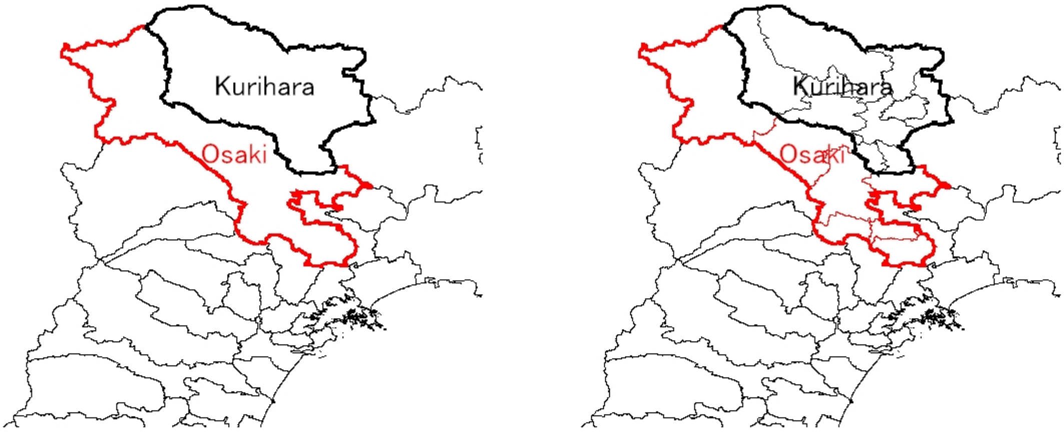

Fig. 2.11 Conception about districts (Left) and subdistricts (Right) in the Osaki and Kurihara cities, Miyagi prefecture

In addition, the period characteristics of ground motions for stricken districts are shown in Fig. 2.12. In this figure, PGA and PGV are the maximum values of vector summation in three components. The straight solid line is plotted according to the different equivalent predominant period, T_{eq}, which is defined as $T_{eq} = 2\pi PGV/PGA$. DR is divided into four levels, i.e., $0\% \leqslant DR < 20\%$, $20\% \leqslant DR < 40\%$, $40\% \leqslant DR < 60\%$, and $60\% \leqslant DR$. Three heavy damaged sites, i.e., JR-Takatori (DR=95.3%), JMA Kobe (DR=71.0%), and Fukiai (DR=48.7%) during the 1995 Kobe earthquake are also included. Kawase (1998) pointed out that heavy damage will occur for the ground motions with PGA greater than 800 gal, PGV greater than 100 m/s, and equivalent predominant period is around 1.0 s. It well accounts for the three heavy damaged sites during the 1995 Kobe earthquake. During the mainshock of the 2011 Tohoku Earthquake, it can be seen that PGAs in many stricken districts are larger than 800 gal, but there are almost no records over 100 cm/s, which result in the short equivalent predominant period of about 0.5 s. This can be partly used to explain the lower damage ratios compared with the heavy damaged sites during the 1995 Kobe earthquake. Fig. 2.13 shows the pseudo-velocity response spectra (pSv) of the ground motions used in the stricken districts. It can be seen that most of the amplitude is smaller than 200 cm/s, which may not cause much damage to buildings. The ground motions with large amplitude of pSv are predominant at about 0.5 s, which also will not cause much damage to buildings. The amplitude of pSv between 1.0 s and 2.0 s which is thought to be closely related with building damage is not large compared with that of pSv at JR-Takatori during the 1995 Kobe earthquake. It also accounts for the relatively low damage ratios during the 2011 Tohoku Earthquake.

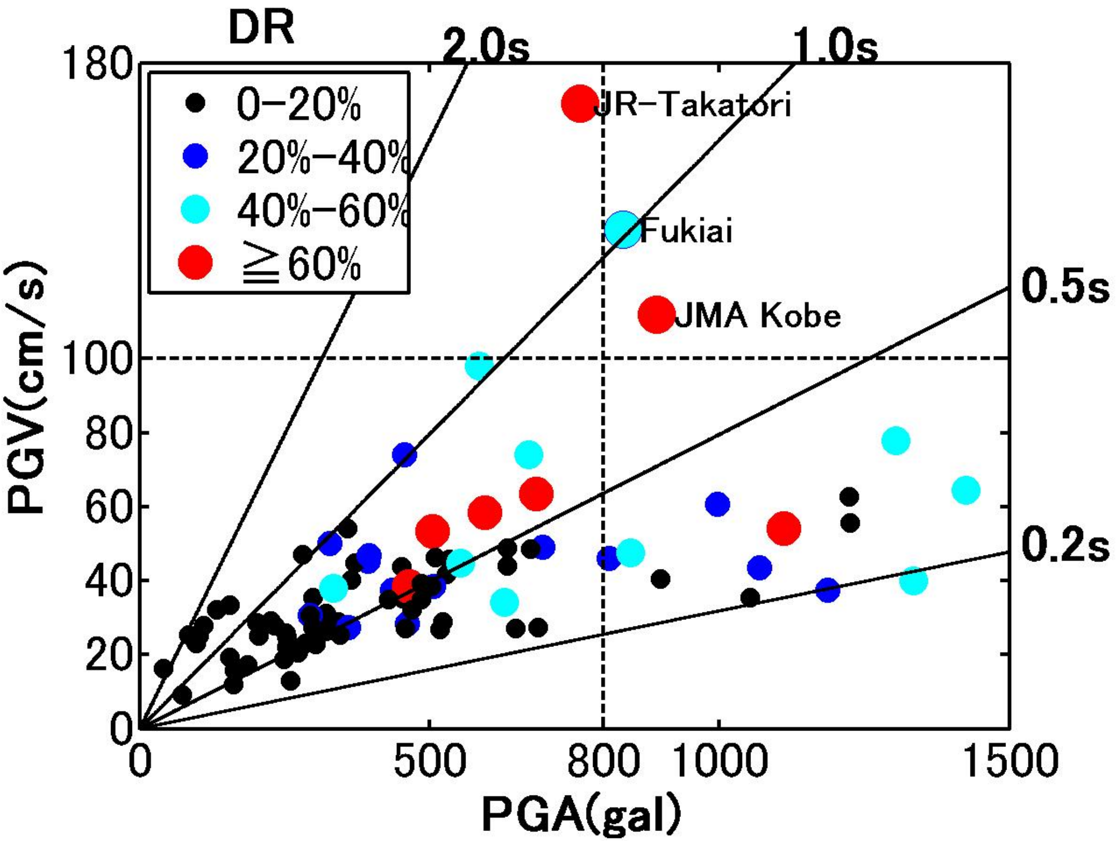

Fig. 2.12 Distribution of equivalent predominant periods of ground motions in the stricken districts. The straight lines correspond to 0.2 s, 0.5 s, 1.0 s, 2.0 s for T_{eq} ($T_{eq} = 2\pi PGV/PGA$) respectively. The broken line shows the threshold value for heavy damage after Kawase (1998). Three damaged sites, i.e., JR-Takatori, Fukiai and JMA-Kobe, in which the buildings were subjected to heavy damage during the 1995 Kobe Earthquake are also included.

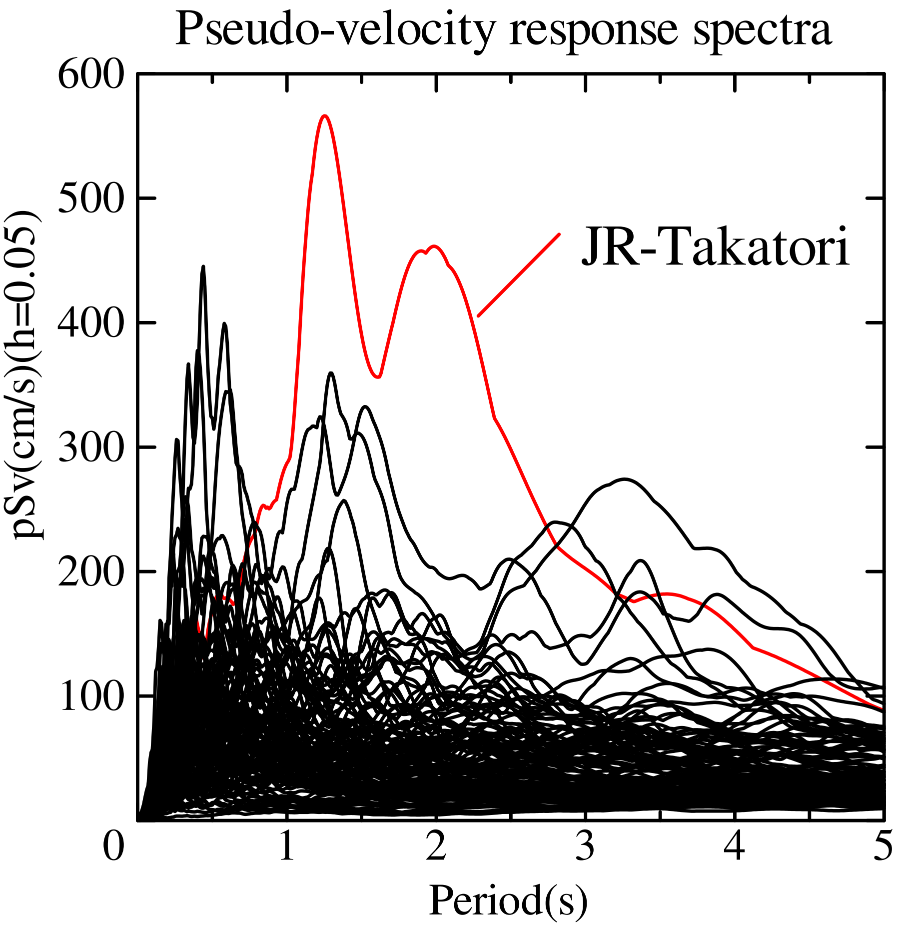

Fig. 2.13 Pseudo-velocity response spectra for ground motions analyzed in the stricken districts. Black curves are the pseudo-velocity response spectra during the 2011 Tohoku Earthquake; red curve is the pseudo-velocity response spectrum at JR-Takatori station during the 1995 Kobe Earthquake.

2.3 Summary

The relationships between three kinds of damage ratios, i.e., TCR, CR, and DR, and four ground motion indices based on observed records at strong-motion stations (i.e., K-NET or KiK-net stations) in the stricken districts, i.e., PGA, PGV, I_{JMA} and SI are investigated in this chapter. The following conclusions can be obtained.

Damage ratios calculated from damage data in administrative districts have a certain correlation with the observed ground motions. The relationship may be used for damage assessment over a wide damaged ares.

DR is the best index to be related with ground motion indices among three damage ratios. I_{JMA}, PGV and SI have a better correlation with damage ratios than PGA, which can be explained by the sensitivity of PGA to ground motions with short predominant period characteristics. SI and PGV have a good correlation relationship, they are similar to each other from the viewpoint of value. Because of this, the correlation for SI versus damage ratios and PGV versus damage ratios is similar.

The short equivalent predominant period characteristics of ground motions or short predominant period of pseudo-velocity response spectra can be used to explain the relatively low damage ratios during the mainshock.

The ground motions in some stricken districts are not representative. It is one of the reasons for low level of ground motions versus large DRs or high level of ground motions versus low DRs in some districts.

Chapter 3

Verification of identifying velocity structures by use of microtremor H/V spectral ratio and estimating ground motions at target sites during the mainshock

As ground motions varies with geological condition, the ground motions determined by averaging a couple of ground motion data at strong-motion stations within each administrative district may not always represent the overall level for each administrative district, just as pointed out in chapter 2. Therefore, it is necessary to examine the relationships between the damage ratios evaluated in areas smaller than the administrative districts, such as subdistricts, subdivisions of the administrative districts, and the ground motion indices there. We can obtain damage data such as totally collapsed, partially collapsed and partially damaged buildings in subdistricts of the administrative districts from the local governments. However, there were no strong-motion stations in most of the subdistricts during the mainshock. Therefore, it is essential to find a method to properly estimate the ground motions in the subdistricts where strong-motion stations were not installed. This chapter aims at developing one effective method to properly estimate ground motions during the mainshock by use of underground velocity structures and short-period source model. The proposed method will be verified by the following three steps.

First, we compare the difference of identified underground velocity structures between H/V spectral ratios of observed earthquake motions and those of measured microtremor data. Then we examine the difference of transfer functions evaluated from the identified velocity structures.

Second, we confirm whether the underground velocity structures identified from microtremor H/V spectral ratios can be used to estimate surface motions for small earthquakes. The bedrock motions are estimated from the surface observed motions at one of the strong-motion stations with the underground velocity structures identified from microtremor H/V spectral ratio. Then the surface motions are estimated from the bedrock motions with the identified underground velocity structures at one of the other strong-motion stations. If the estimated surface motions coincide with the observed surface motions, it indicates the effectiveness of underground velocity structures identified from microtremor H/V spectral ratios.

Third, we verify whether the estimation method on ground motions is applicable for the mainshock by considering the short-period (0.1 s $\sim$ 10.0 s) source model (Kurahashi and Ikikura, 2013) and underground velocity structures. The surface motions at one strong-motion station are estimated with the underground velocity structures identified from microtremor H/V spectral ratios from the synthesized bedrock motions during the mainshock. Then we examine whether the estimated surface motions coincide with the observed surface motions for the mainshock.

3.1 Methodology on estimating ground motions with underground velocity structures and source model

Generally, the surface motions $O(\omega)$ can be expressed as the product of bedrock motions $B(\omega)$ and transfer function $TF(\omega)$ which is defined as the surface response with respect to incident motions, as shown in Eq. (3.1). Then the bedrock motions $B(\omega)$ can be expressed as the ratio of observed surface motions $O(\omega)$ to transfer function $TF(\omega)$, as shown in Eq. (3.2).

$$O(\omega) = B(\omega) \times TF(\omega) \tag{3.1}$$

$$B(\omega) = O(\omega)/TF(\omega) \tag{3.2}$$

Considering that there are a strong-motion station X where surface motions are observed and a target site Y where the surface motions are unknown, as shown in Fig. 3.1, Y is located near X. By assuming the bedrock motions under both sites to be the same, the surface motions $E_Y(\omega)$ at the target site Y can be estimated from the bedrock motions at X and transfer functions $TF_Y(\omega)$ at the target site Y, as shown in

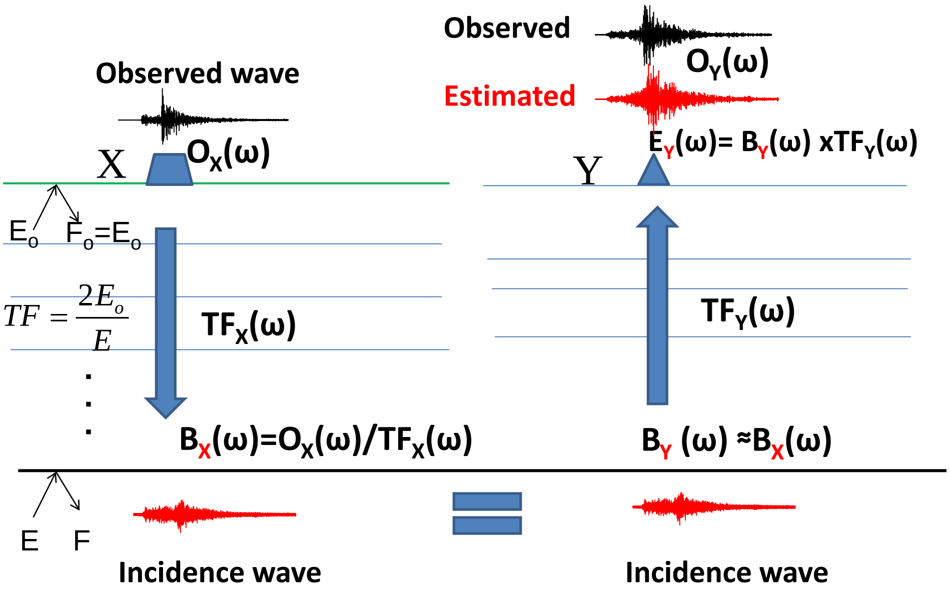

Fig. 3.1 Illustration about verification of estimating ground motions for small earthquakes

Eq. (3.3). The assumption about common bedrock motions may be reasonable if the distance between X and Y is much shorter than the hypocenter distance.

$$E_Y(\omega) = B_Y(\omega) \times TF_Y(\omega) = B_X(\omega) \times TF_Y(\omega) = E_X(\omega)/TF_X(\omega) \times TF_Y(\omega) \qquad (3.3)$$

However, for the 2011 Tohoku Earthquake, the soft soil at some sites may behave nonlinear near the surface which suggests the bedrock motions may not be directly estimated by Eq. (3.2). In order to avoid the potential nonlinear effect on the surface motions, we firstly estimate the bedrock motions under the strong-motion station during a small earthquake as shown in Fig. 3.2, then synthesize them into the ones for the mainshock with "modified empirical Green's function method" by use of the source model. Then the ground motions for the mainshock on the surface at the target sites can be estimated just as shown in Eq. (3.3) if the nonlinear effect is limited.

Attention should be paid to the difference between "modified empirical Green's function method" and empirical Green's function method. The formulation for empirical Green's function method can be expressed as Eq. (3.4) according to Irikura (1986).

$$U(t) = \sum_{i=1}^{N} \sum_{j=1}^{N} \frac{r}{r_{ij}} F(t - t_{ij}) * \{c \cdot u(t)\} \qquad (3.4)$$

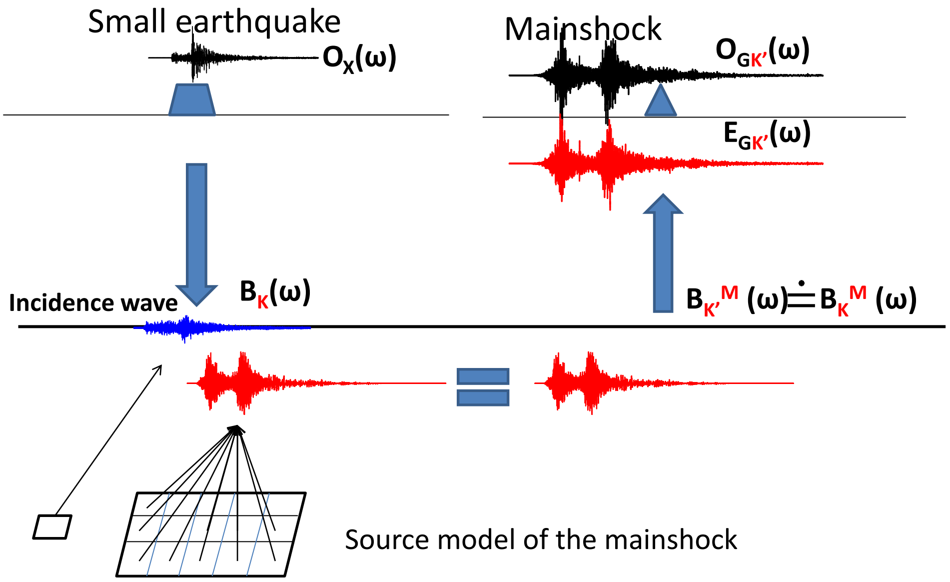

Fig. 3.2 Illustration about estimating ground motions during the mainshock

where

$U(t)$ is the simulated waveform for mainshock;

r is the distance between small fault and the strong-motion station;

r_{ij} is the distance between small fault and the strong-motion station;

$F(t - t_{ij})$ is the correction function used to adjust for the difference in the slip velocity time functions between the large and small events.

$u(t)$ is the observed waveform during a small earthquake.

From this equation, we can see that the observed waveform is the crucial element for this method. However, in order to avoid the nonlinear effect near the surface, the estimated bedrock waveform is taken as the Green's function, then it is synthesized into the one during the mainshock. We call it as "modified empirical Green's function method" to distinguish it from the conventional one.

For the estimation of ground motions during the mainshock, three elements are needed, i.e., the source model and underground velocity structures under the strong-motion stations and target sites. Because many researchers, such as Kurahashi and Irikura (2011),Asano and Iwata (2012),Kawabe et al. (2012),Kurahashi and Ikikura (2013) have presented the short-period source model for the mainshock, what is left is how to evaluate the transfer functions which depend on the underground velocity structures. Next section will focus on how to obtain the reliable underground velocity structures.

3.2 Verification of identifying underground velocity structures from microtremor H/V spectral ratio

Underground velocity structures can be determined by reflection method, refraction method, inversion method from surface-wave dispersion data, inversion method from H/V spectral ratio of microtremor or earthquake ground motions and so on. Either the reflection or refraction method needs artificial sources usually imposed by vibrator or impactor on the surface. On the other hand, inversion method from surface wave dispersive curve needs array observation of microtremors at the same time at several fixed sites. Identification of underground velocity structures from H/V spectral ratio is considered to be the most convenient and efficient methods as it just needs observation with three components sensors at a single station. It has been suggested by many researchers that the underground velocity structures can be identified from either earthquake H/V spectral ratio or microtremor H/V spectral ratio. However, hitherto not so many studies have been done on how the different of the two underground velocity structures identified from these two kinds of H/V spectral ratios at the same site. Therefore, we attempt to identify the underground velocity structures from H/V spectral ratios of earthquake motions and microtremors respectively at the same site. Then we can investigate not only the difference of underground velocity structures but also the effect of this difference on the transfer functions of ground motions between bedrock and ground surface.

3.2.1 Identification of underground velocity structures from earthquake H/V spectral ratio

3.2.1.1 Theoretical calculation of earthquake H/V spectral ratio

Earthquake motions can be observed at permanent strong-motion stations. The characteristics of earthquake ground motions are affected by magnitude, depth of source, propagation path, soil condition near the surface and so on. The spectral ratio of horizontal to vertical component, i.e., H/V, can eliminate the effect from source and propagation path effectively. Therefore, H/V can be regarded as the intrinsic property of velocity structure under the site, which implies that it can be used to identify the underground velocity structures. Phinney (1964) determined the crustal structure using spectral ratio of the radial component to vertical component of teleseismic P waves. Lermo and Chávez-García (1993) explored the Nakamura technique (Nakamura, 1989) which was originally proposed for microtremor to evaluate the empirical transfer function response from earthquake H/V spectral ratio. Satoh et al. (2001) investigated the differences of site characteristics obtained from S-waves, P-waves and codas, as well as microtremors. However, the theoretical basis was not clarified until Kawase et al. (2011) applied the diffuse theory to express the earthquake H/V spectral ratio shown in Eq. (3.5) as the amplitude ratio between transfer functions for the horizontally polarized S-wave incidence and the vertically polarized P-wave incidence, both calculated at the observation point with a coefficient depending on the bedrock property. Ducellier et al. (2012, 2013) proved the validation of identifying underground velocity structures from the earthquake H/V spectral ratio proposed by Kawase et al. (2011).

$$\frac{H}{V}(\omega) = \sqrt{\frac{2V_P^H}{V_S^H}}\left|\frac{TF_S(\omega)}{TF_P(\omega)}\right| \tag{3.5}$$

where

V denotes the body wave velocity;

TF denotes transfer function which is defined as the surface response with respect to incident wave from the half-space;

superscript H denotes the half-space;

subscripts P and S denotes P-wave and S-wave respectively.

3.2.1.2 Data processing of observed earthquake H/V spectral ratio

The earthquake H/V spectral ratios are different at the specified site depending on the direction of propagation from the source if the underground velocity structures are not approximated to be a one-dimension (1D) model. It is reasonable to take an average over many earthquake records. On the other hand, the H/V spectral ratio of small earthquakes is different from that of large earthquakes due to the nonlinear effect. As a result, the underground velocity structures should be identified from the H/V spectral ratio averaged over many small earthquakes records. Here, we choose the records of small earthquakes with magnitude ranging from 4.0 to 6.5, PGA smaller than 100 gal, and the epicenter distance of less than 200 km. In addition, earthquake H/V spectral ratios are different depending on the portion of waveforms used. As Kawase et al. (2011) suggested that H/V spectral ratio of earthquake motions is stable whichever the part of record is used except P-wave portion, we adopt the records with a duration of 40.96 s from S-wave onset time to calculate the H/V spectral ratio. The S-wave onset time is determined by eye judgement for sake of simplicity, approximately the time after which the amplitude of acceleration waveforms reaches the largest as shown in Fig. 3.3. After obtaining H/V spectral ratio of three components record at each site, smoothing is imposed in the logarithmic scale proposed by Konno and Ohmachi (1998). Finally, the H/V spectral ratio at the strong-motion station is obtained by averaging all the smoothed H/V spectral ratios over the total number of records.

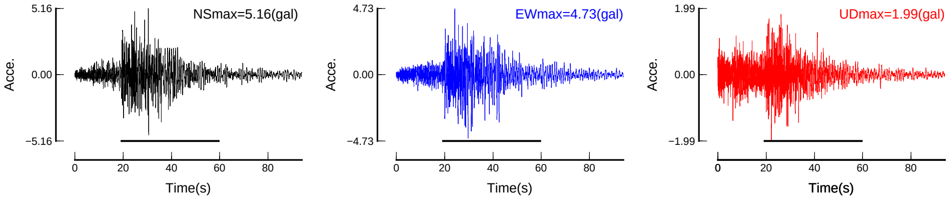

Fig. 3.3 An example waveform during an earthquake. The solid line under the waveforms show the wave portion used to calculate earthquake H/V spectral ratio

Now we show an example to calculate the earthquake H/V spectral ratio at a strong-motion station, MYG006, in the Furukawa city of Miyagi prefecture. Fig. 3.4 shows the distribution of epicenters of seven small earthquakes. The source information about the small earthquakes used in this study is listed in Table 3.1. The duration of these records ranges from 60 s $\sim$ 120 s. Fig. 3.5 shows the H/V spectral ratios of the records from the seven earthquakes with thin black line and the average of them with red. It is reasonable to adopt the average H/V spectral ratio at the target site for identification of underground velocity structures, because the variation of H/V spectral ratios exists for the seven small earthquakes.

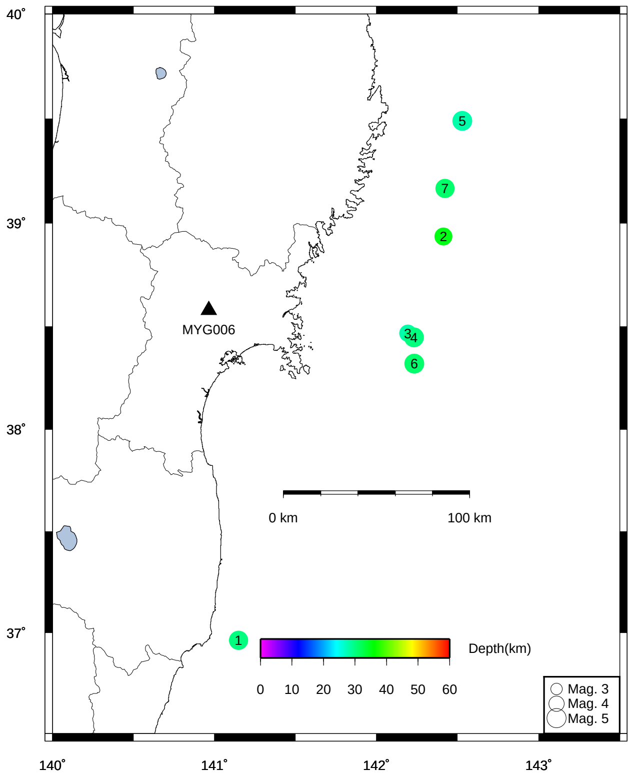

Fig. 3.4 Distribution of epicenters for small earthquakes around MYG006

Table 3.1 Small earthquake information used in the analysis for MYG006

Order	Date-time	Latitude (°E)	Longitude (°N)	Depth (km)	M_{JMA}*	PGA (gal)	Ts** (s)
01	2011/10/26-02:08	36.962	141.147	30	5.0	5.2	19.0
02	2011/09/13-23:14	38.935	142.413	35	4.7	6.0	13.0
03	2011/08/17-12:14	38.468	142.193	28	4.5	9.5	29.0
04	2011/08/11-22:31	38.448	142.230	30	5.3	14.2	28.5
05	2011/06/14-23:56	39.490	142.528	28	5.3	15.5	16.0
06	2011/04/21-17:18	38.320	142.232	31	5.2	20.7	15.0
07	2011/04/15-23:34	39.167	142.422	31	5.0	11.6	15.0

* M_{JMA} is a magnitude determined by Japan Meteorological Angency

** T_S is the onset time of S-wave determined by eye judgement.

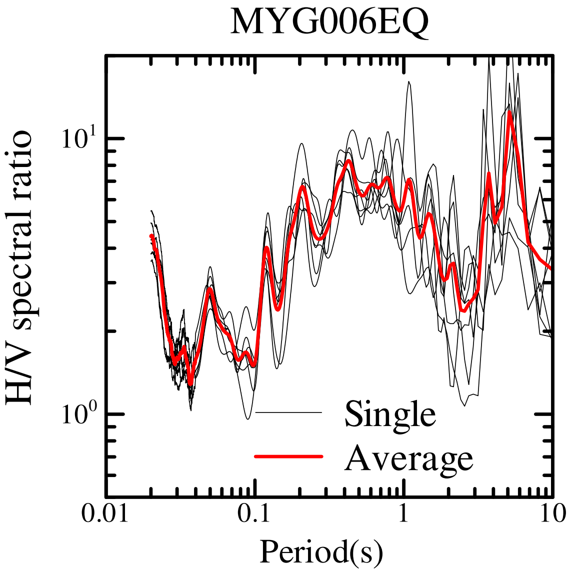

Fig. 3.5 Earthquake H/V spectral ratios of MYG006

3.2.1.3 Identification of velocity structures from earthquake H/V spectral ratio

Simulated annealing algorithm is used to identify the velocity structures in this study. Compared with other search schemes, such as genetic algorithm, simulated annealing algorithm is good at searching the global minimum among many local minima for the objective function. The simulated annealing algorithm used in this study refer to the one developed by Ingber (1989), Saguchi et al. (2009), Satoh (2006). The optimal underground velocity structures are determined by minimizing the misfit function which is expressed in Eq. (3.6). Additionally, it is necessary to specify the temperature reduction function expressed as Eq. (3.7).

$$E_m = \frac{\sum_{f_{min}}^{f_{max}} \left| \frac{(H/V)^{cal} - (H/V)^{obs}}{f_i} \right|}{\sqrt{\sum_{f_{min}}^{f_{max}} \frac{(H/V)^{cal}}{f_i} \sum_{f_{min}}^{f_{max}} \frac{(H/V)^{obs}}{f_i}}} \tag{3.6}$$

where

f_i denotes frequency;

f_{min} and f_{max} are set to be 0.33 Hz and 20.0 Hz respectively;

$(H/V)^{cal}$ and $(H/V)^{obs}$ denote the theoretical and observed H/V spectral ratios respectively.

$$T_k = T_0 \cdot exp(-ck^{\alpha}) \tag{3.7}$$

where

T_k is the temperature for the k_{th} time;

T_0, c and α are the constant which are set to be 1.0, 0.6 and 1.0, respectively.

In order to trigger the identification procedure, initial velocity structure model is needed. In Japan, these data can be obtained for the strong-motion stations (i.e., K-NET and KiK-net) operated by NIED in the shallow layers, while the initial velocity structure model in the deep layers can refer to the J-SHIS website. The optimal velocity structures model is obtained by a search range centered the initial model with simulated annealing algorithm. As a case study, we implement the identification at one strong-motion station, MYG006.

Table 3.2 shows the initial velocity structure model generated by use of PS-logging data from NIED and those published by J-SHIS. As the identified velocity structures may be different from the identification schemes, three kinds of schemes are applied to obtain the optimal one. (a) Only identifying the parameters about S-wave, such as S-wave velocity (V_S), Q_{S0} and n (Q_S is assumed to be $Q_S = Q_{S0} \times f^n$) in each layer from surface to bedrock (V_S=3.1 km/s); (b) identifying the parameters about S-wave in shallow layers (about -100 m in the depth, depending on the soil condition), and identifying the thicknesses of deep layers; (c) identifying the parameters about S-wave and thickness in each layer from surface to bedrock. The optimal velocity structures are selected from these three schemes. The search range with respect to the initial model should be as large as possible, it is set to be 80% for each parameter in this study. In addition, in order to improve the efficiency of identification, the parameters about P-wave, such as P-wave velocity (V_P) and Q_P are determined from empirical relationships with S-wave, according to Eq. (3.8) by Kitsunezaki et al. (1990) and Eq. (3.9) by Yoshida and Kobayashi (2002), as well as the fixed thickness and density in each layer. It may not have a significant effect on the final results, as the objective function, i.e., H/V is insensitive to these parameters just as the suggestions from Arai and Tokimatsu (2004), Satoh (2006).

$$V_p = 1.11 \times V_s + 1290.0 \qquad (unit : m/s) \tag{3.8}$$

$$Q_P = Q_S/2.0 \tag{3.9}$$

Fig. 3.6 and Table 3.3 shows the identified velocity structures at MYG006. The H/V spectral ratios calculated with the identified model are in a good agreement with the observed one in a period range less than 0.3 s as shown in left upper panel of

Table 3.2 Initial underground velocity structures at MYG006

$\rho(ton/m^3)$	Vs(m/s)	Vp(m/s)	Qs	n	H(m)	Depth(m)
1.42	70	350	10	0.5	1.0	2.0
1.75	130	1420	10	0.5	2.5	17.0
1.75	130	1420	10	0.5	2.5	17.0
1.75	130	1420	10	0.5	10.0	17.0
1.85	400	1880	20	0.5	3.0	20.0
1.90	600	2000	100	0.5	12.0	68.0
2.00	700	2100	100	0.5	12.0	68.0
2.00	800	2200	100	0.5	12.0	68.0
2.10	950	2400	100	0.5	12.0	68.0
2.15	1200	2600	100	0.5	200.0	300.0
2.25	1400	3000	100	0.5	200.0	500.0
2.30	1600	3400	100	0.5	236.0	704.0
2.35	1900	3750	150	0.5	649.0	1353.0
2.40	2100	4000	150	0.5	520.0	1873.0
2.50	2700	4600	150	0.5	1170.0	3043.0
2.50	3100	5500	200	0.5	0.0	0.0

Fig. 3.6. Concerning the period range less than 0.3 s, even peak periods of the H/V spectral ratios with the initial model is almost consistent with those of the observed one, although amplitudes are different from each other. It comes from the similarity of Vs structures less than 100 m between the initial model and the identified model as shown in right lower panel of Fig. 3.6. Meanwhile, the amplitudes of the H/V spectral ratios with the initial model are larger than those of observed ones, which come from the Q_S values in the identified model smaller than those in the initial model shown in Table 3.3. The period range in this analysis is limited to less than 3.0 s, therefore the Vs structures in deep layers related to longer period than 3.0 s are not reliable. The transfer functions for S- and P-wave velocity structures are also shown in the right upper panel of Fig. 3.6. It can be seen that the S-wave transfer function is larger than 4.0 from 0.15 s to 2.0 s, while the P-wave transfer function is rather small.

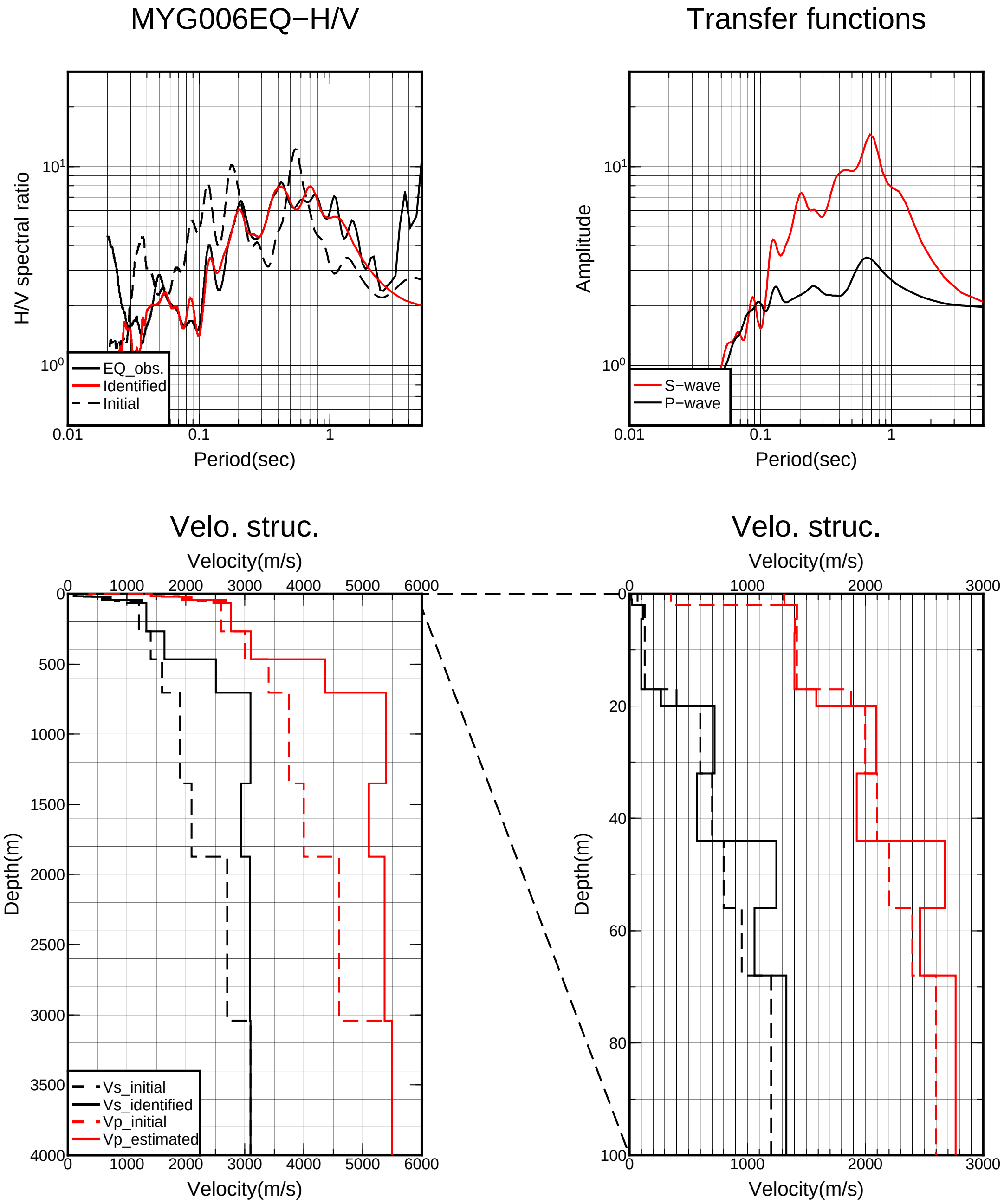

Fig. 3.6 Identification of underground velocity structures at MYG006 from earthquake H/V spectral ratio (target period range is 0.05 s ∼ 3.0 s)

Table 3.3 Identified underground velocity structures from earthquake H/V spectral ratio at MYG006

$\rho(ton/m^3)$	Vs(m/s)	Vp(m/s)	Qs	n	H(m)	Depth(m)
1.42	20.2	1312.4	1.4	0.68	1.0	2.0
1.75	115.0	1417.7	11.7	0.99	2.5	4.5
1.75	102.0	1403.2	11.7	1.00	2.5	7.0
1.75	100.0	1401.0	3.1	1.00	10.0	17.0
1.85	265.7	1584.9	10.9	1.00	3.0	20.0
1.90	723.6	2093.2	26.8	1.00	12.0	32.0
2.00	572.8	1925.8	20.0	1.00	12.0	44.0
2.00	1246.7	2673.8	8.0	0.76	12.0	56.0
2.10	1058.5	2465.0	9.5	0.00	12.0	68.0
2.15	1330.6	2767.0	75.7	0.00	200.0	268.0
2.25	1635.8	3105.7	126.0	0.00	200.0	468.0
2.30	2509.1	4365.9	143.9	1.00	236.0	704.0
2.35	3100.0	5394.0	19.0	0.00	649.0	1353.0
2.40	2931.5	5100.7	21.0	0.00	520.0	1873.0
2.50	3087.3	5372.0	27.0	1.00	1170.0	3043.0
2.50	3100.0	5500.0	31.1	0.00	0.0	0.0

3.2.2 Identification of underground velocity structures from microtremor H/V spectral ratio

3.2.2.1 Theoretical calculation of microtremor H/V spectral ratio

Compared with earthquake H/V spectral ratio, microtremor H/V spectral ratio is widely applied to identify the underground velocity structures as the microtremors generated by human activies or even natural phenomena (such as sea, wind) can be observed conveniently. Nakamura (1989, 2000) asserted that microtremor H/V spectral ratio can be explained by vertical incident SH waves. That is, the predominant period was consistent with that of SH waves, and the amplitude was almost the same as the amplification factor due to multiple reflected SH waves. On the other hand, Tokimatsu and Miyadera (1992), Lachet and Bard (1994), Konno and Ohmachi (1998), Fäh et al. (2001) suggested that the predominant period of microtremor H/V spectral ratio can be explained by that of fundamental mode of Rayleigh wave, i.e., ellipticity, and implied that the amplitude of microtremor H/V spectral ratio was affected by higher modes of Rayleigh waves. Arai and Tokimatsu (2000, 2004) pointed out that the predominant period of microtremor H/V spectral ratio was mainly controlled by higher modes of Rayleigh waves, and the amplitude of H/V spectral ratio was controlled by Love waves. They expressed the microtremor H/V spectral ratio shown in Eq. (3.10) as the square root of the summation of power spectra for Rayleigh and Love waves in the horizontal component to the power spectrum of Rayleigh waves in the vertical component. They further proved that the observed microtremor H/V spectral ratio can be used to identify underground velocity structures in the shallow layers by fitting the theoretical one incorporating higher modes of both Rayleigh and Love waves. Recently, Sánchez-Sesma et al. (2011) succeeded in explaining the microtremor H/V spectral ratio by use of diffuse filed theory which included all the contributions of Rayleigh, Love and body waves. They expressed the microtremor H/V spectral ratio shown in Eq. (3.11) as the square root of the ratio of the corresponding imaginary parts of Green's tensor components. Tobita et al. (2012) applied their theoretical H/V spectral ratio to identify the underground velocity structures in the Osaka basin of Japan.

$$\frac{H}{V}(\omega) = \sqrt{\frac{P_{HR}(\omega) + P_{HL}(\omega)}{P_{VR}(\omega)}} \tag{3.10}$$

where

$P_{HR}(\omega)$ and $P_{HL}(\omega)$ are the power spectra in the horizontal component for Rayleigh waves and Love waves respectively;

$P_{VR}(\omega)$ is the power spectrum in the vertical component for Rayleigh waves.

$$(\frac{H}{V})(\omega) = \sqrt{\frac{ImG_{11}(\omega) + ImG_{22}(\omega)}{ImG_{33}(\omega)}} \tag{3.11}$$

where ImG_{ii} is the imaginary part of Green function when source and receiver are the same.

In this study, we decide to identify the underground velocity structures using the theoretical microtremor H/V spectral ratio proposed by Arai and Tokimatsu (2004), because the calculation of theoretical microtremor H/V spectral ratio proposed by Sánchez-Sesma et al. (2011) needs the analytic Green function which is a time consuming process, it is not suitable for identifying velocity structures with simulated annealing algorithm, although it may be possible for genetic algorithm or grid search (Tobita et al., 2012). Then, we will explain the variables of Eq. (3.10) in detail. Considering higher modes of Rayleigh and Love waves, $P_{HR}(\omega)$ and $P_{HL}(\omega)$ can be expressed as follows:

$$P_{HR}(\omega) = \kappa L_V^2 \sum_{m=0}^{M} \left(\frac{A_{Rm}}{k_{Rm}}\right)^2 \left(\frac{u}{w}\right)_m^2 \left[1 + \left(\frac{\alpha^2}{2}\right)\left(\frac{u}{w}\right)_m^2\right] \tag{3.12}$$

$$P_{HL}(\omega) = \kappa L_V^2 \sum_{m=0}^{M} \left(\frac{\alpha^2}{2}\right)\left(\frac{A_{Lm}}{k_{Lm}}\right)^2 \tag{3.13}$$

$$P_{VR}(\omega) = \kappa L_V^2 \sum_{m=0}^{M} \left(\frac{A_{Rm}}{k_{Rm}}\right)^2 \left[1 + \left(\frac{\alpha^2}{2}\right)\left(\frac{u}{w}\right)_m^2\right] \tag{3.14}$$

where

κ is a function with respect to attenuation coefficient, it will be cancelled as it comes out both in numerator and denominator;

L_V is the point force randomly distributed on the free surface;

M is the maximum number of higher modes considered;

A is the medium response;

k is the wavenumber;

α is the H/V ratio of the microtremor loading sources, L_H/L_V, which is assumed to be constant in the area considered;

u/w is the ellipticity or the H/V ratio of Rayleigh waves on the free surface.

From the above equations, we can see the coefficient κL^2 can be cancelled out for Eq. (3.10), which means that the scattering damping ratio has no effects on the H/V spectral ratio and therefore can not be identified by fitting the observed H/V spectral ratio. What's more, α is the only unknown in order to evaluate the H/V spectral ratio, provided the velocity structures are given. Arai and Tokimatsu (2000) suggested to determine this parameter by assuming $(R/L)(\omega)$ to be 0.7. $(R/L)(\omega)$ is defined as the Rayleigh-to-Love-wave amplitude ratio for horizontal motions at a certain frequency ω.

$$\left(\frac{R}{L}\right)(\omega) = \sqrt{\frac{P_{HR}(\omega)}{P_{HL}(\omega)}} \tag{3.15}$$

By substituting the expressions in Eq. 3.12 into Eq. 3.15, we can express the α as follows:

$$\alpha = \sqrt{\frac{2 \cdot \sum_{m=0}^{M} (A_{Rm}/k_{Rm})^2 (u/w)_m^2}{[R(\omega)/L(\omega)]^2 \sum_{m=0}^{M} (A_{Lm}/k_{Lm})^2 - \sum_{m=0}^{M} (A_{Rm}/k_{Rm})^2 (u/w)_m^4}} \tag{3.16}$$

It should be noticed that the denominator may become negative at some frequencies because of a constant (R/L), although α should be a real. In that case, the values of H/V are set to be zero, as there is no physical meaning at those frequencies.

3.2.2.2 Data processing of observed microtremor H/V spectral ratio

Except the information about the soil condition, microtremors include many noises caused by human activies, climate condition and so on. Averaging is considered to be one of the most effective methods to reduce these noises, as microtremor can be regarded as a stochastic process. However, for microtremor H/V spectral ratio, there are three kinds of averaging schemes which result in different H/V spectral ratio. We call them conventional H/V (calculating the H/V spectral ratio in each window, then averaging them over the total number of time windows), Arai's H/V (averaging the horizontal spectra and vertical spectra over the total number of time windows, then calculating the H/V spectral ratio, just as Eq. (3.17)) and Sánchez's H/V (averaging the normalized horizontal and vertical spectra with respect to spectral summation for three components over the total number of time window, then calculating the H/V spectral ratio as suggested by Sánchez-Sesma et al. (2011)). Before comparing their difference, the initial processing about microtremor data should be presented.

$$\frac{H}{V}(\omega) = \sqrt{\frac{P_{NS}(\omega) + P_{EW}(\omega)}{P_{UD}(\omega)}} \tag{3.17}$$

where $P(\omega)$ denotes the power spectrum in one of the three components, i.e., NS, EW and UD.

Fig. 3.7 shows a microtremor observation in time domain with a duration of one hour. As usual, noises with extraordinary large amplitude, e.g., the wave portion around 2800 s in Fig. 3.7, will be excluded from the original microtremor records in three components firstly, e.g. north-to-south (NS), east-to-west (EW), up-to-down (UD). Next the observed data in three components are continuously divided into many segments with the same length of duration (time window), e.g., 40.96 s in this study. Power (or Fourier) spectra in three components are then obtained after offsetting and tapering. The horizontal spectrum is the square root of the summation of power spectra (or squares of Fourier spectra) in the NS and EW components. Finally, smoothing is implemented in the logarithmic scale just as that for the earthquake H/V spectral ratio. Then, we will discuss the differences of microtremor H/V spectral ratios dependent on the three different average schemes.

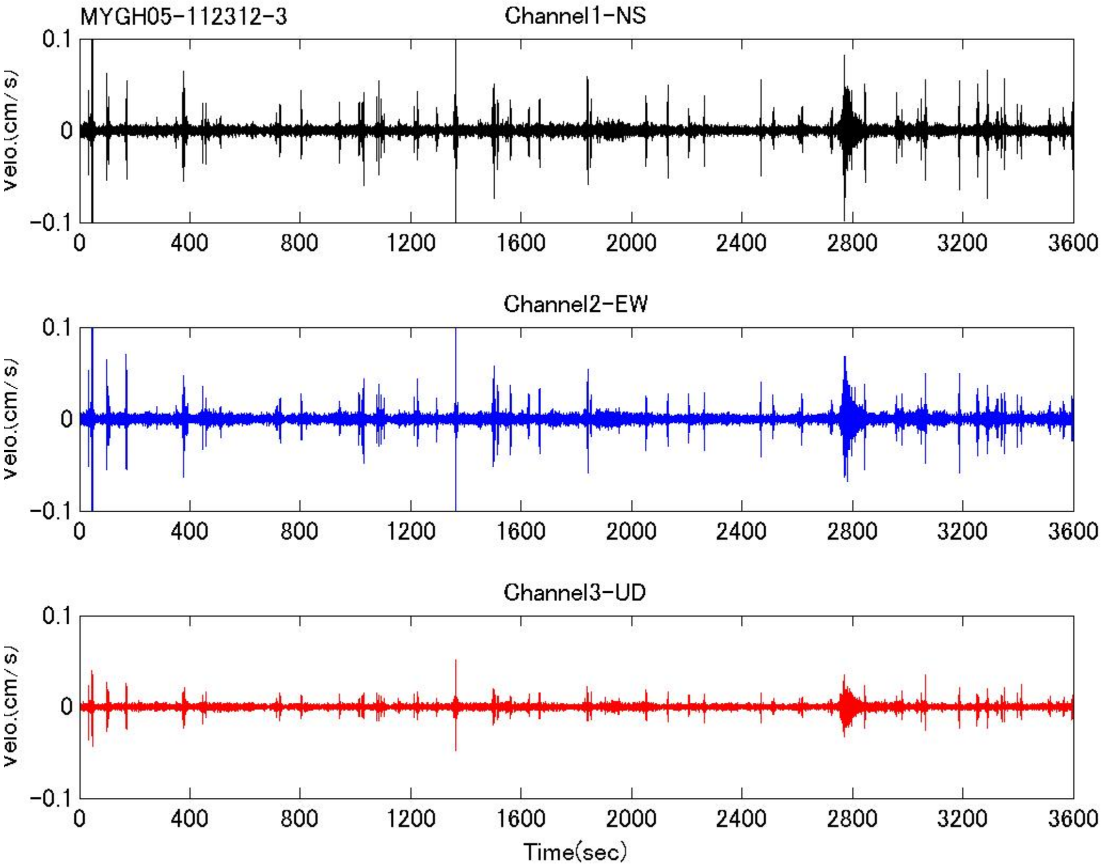

Fig. 3.7 An example waveform of microtremor observed near the MYGH05 strong-motion station from 12:00 to 13:00 on Nov. 23, 2012

Without loss of generality, we compare these three different H/V spectral ratios at four sites near the strong-motion stations (AICH04, GIFH09, MYGH05 and MYGH06) as shown in Fig. 3.8. We can find that the conventional calculation method for H/V spectral ratio is generally larger than the other two H/V spectral ratios, while the Arai's H/V is similar to Sánchez's H/V. It can be explained that the amplitude of signal involved in microtremor for the vertical component is too weak, which leads to the larger amplitude of microtremor H/V spectral ratio. We can also obtain the similar conclusion for earthquake H/V spectral ratios. It seems that the Sánchez's H/V is most reliable because it suggests that the resulting illumination is totally or partially equipartitioned. But because the difference between Arai's H/V and Sánchez's H/V is trivial, and Arai's assumption about R/L is based on his H/V calculation method, we finally adopt the Arai's H/V method to obtain the microtremor H/V spectral ratio.

Another important thing about microtremor is the stability or temporal variabilities. As microtremors are affected by many factors, they exhibit difference depending on the strength of the surrounding human activity, temperature, atmosphere etc. Although

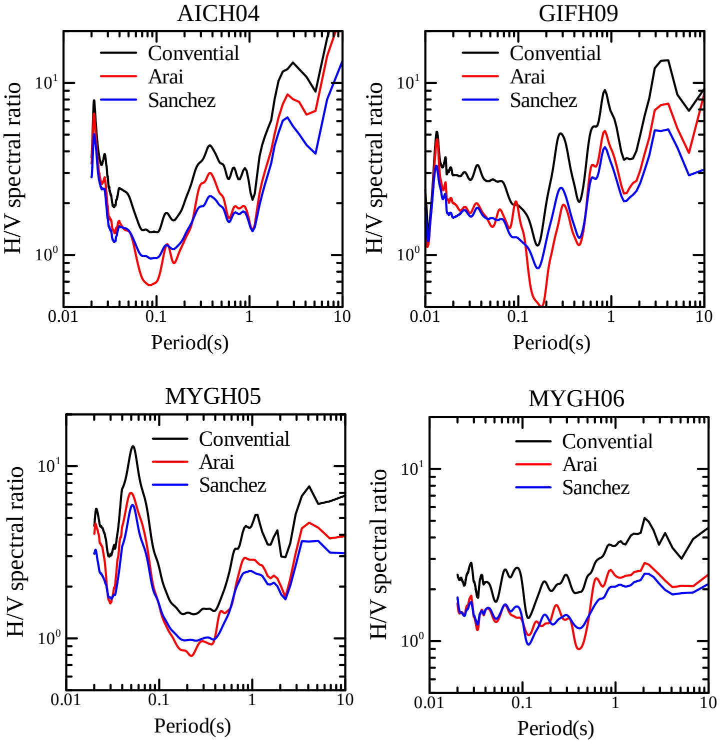

Fig. 3.8 Difference of microtremor H/V spectral ratio due to different calculation method

the temporal variation has been studied by several researchers, Nakamura (1989) and Okada and Suto (2003), we still think it is necessary to examine the characteristics of microtremor for temporal variability. Fig. 3.9 ∼ Fig. 3.12 show the temporal variation of microtremor H/V spectral ratios in the vicinity of four strong-motion stations (GIGH09, AICH04, MYGH05 and MYG009). The total observation duration is one week at GIFH09, three days at AICH04, one day (24 hrs) at MYGH05 and 3 hrs at MYG009. It can be seen that the power spectrum of each component significantly varies with the time, but the H/V spectral ratios are relatively stable. It seems that the variations of H/V spectral ratios are not obvious for short observation duration, e.g. 3 hours near MYG009 station. Also this variation do not necessarily increase with the time but depend on the noises in the neighbourhood of observation site instead. For instance, the variation of the H/V spectral ratios for 72 hrs near AICH04 station which locates at a relatively silent rice paddy is smaller than that for 24 hrs near MGYH05 station which locates at the intersection of roads. Therefore, it is difficult to determine the observation duration during which the microtremor H/V spectral ratios are stable. It should depend on the noise environment around the observation sites, but it is true that the longer the better.

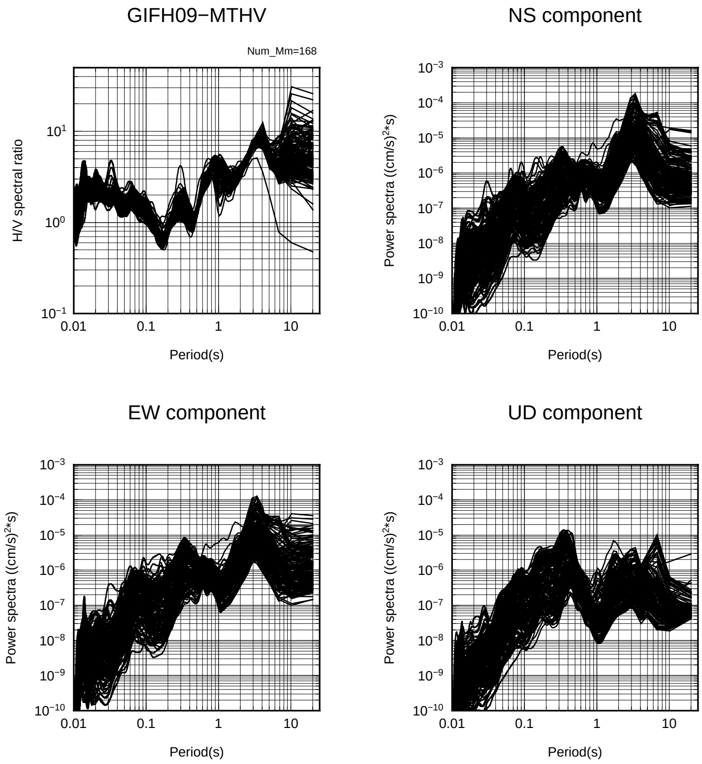

Fig. 3.9 Temporal variation of microtremor H/V spectral ratio for each hour at GIFH09 from 11:00 on Oct. 16 to 11:00 on Oct. 23, 2012

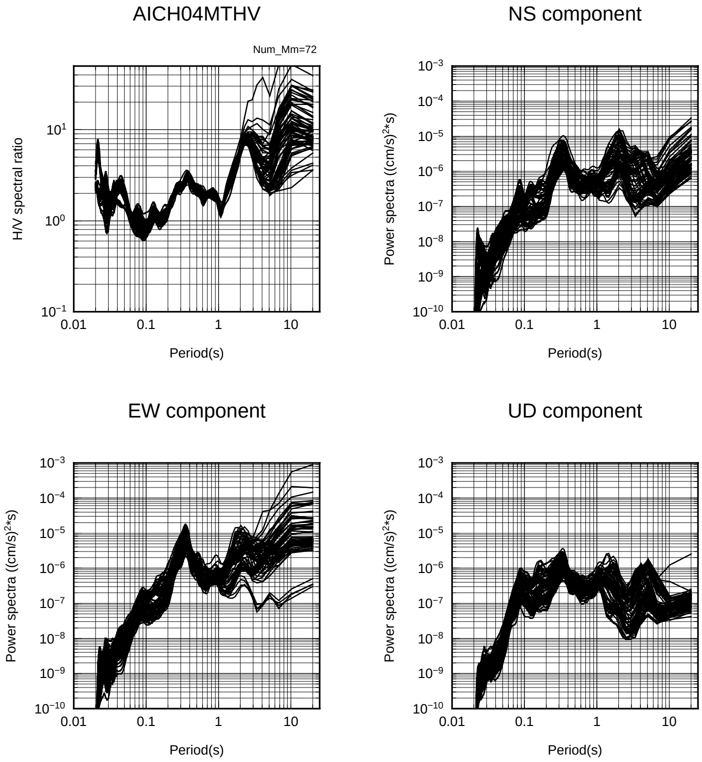

Fig. 3.10 Temporal variation of microtremor H/V spectral ratio for each hour at AICH04 from 19:00 on Oct. 22 to 19:00 on Oct. 25, 2012

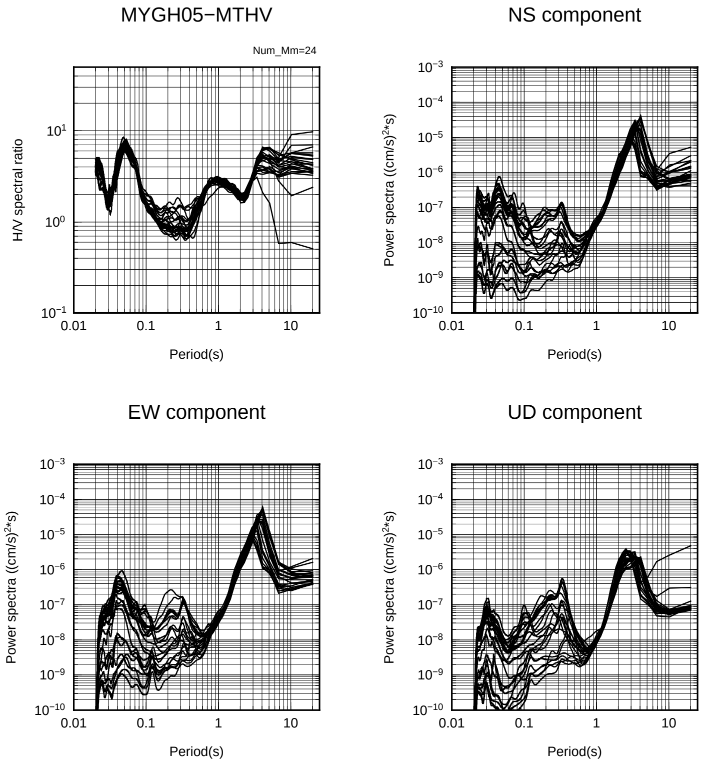

Fig. 3.11 Temporal variation of microtremor H/V spectral ratio for each hour at MYGH05 from 10:00 on Nov. 23 to 10:00 on Nov. 24, 2012

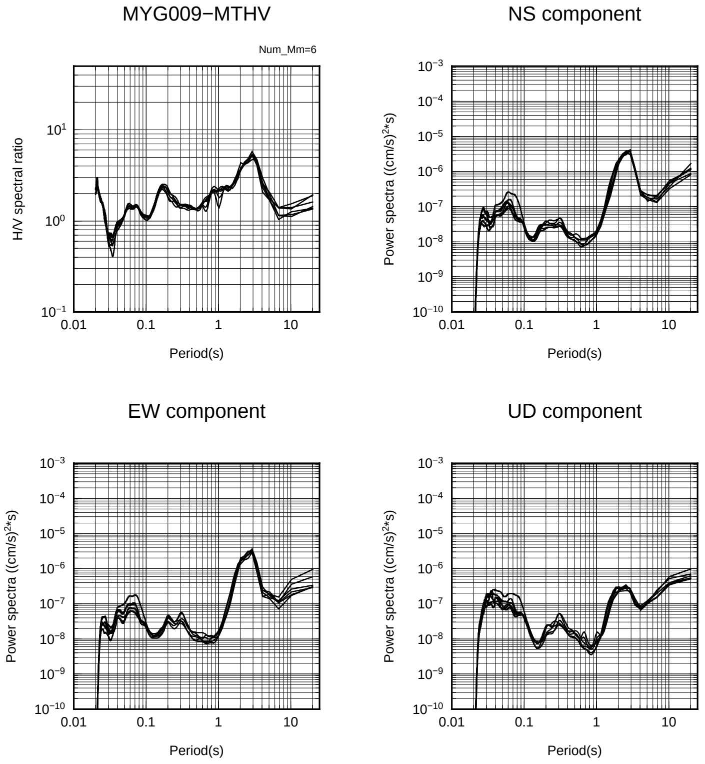

Fig. 3.12 Temporal variation of microtremor H/V spectral ratio for half an hour at MYG009 from 11:15 on Nov. 23 to 14:15 on Nov. 23, 2012

3.2.2.3 Identification of velocity structures from microtremor H/V spectral ratio

Simulated annealing algorithm is also applied to identify underground velocity structures from microtremor H/V spectral ratio. The misfit function and reduce temperature function are the same as those introduced in the subsection 3.2.1.3, except that the theoretical microtremor H/V spectral ratio is calculated through Eq. (3.10), Eq. (3.12) $\sim$ Eq. (3.16). In order to incorporate the effect of the higher modes of surface waves (Rayleigh waves and Love waves), the number of modes should be as large as possible, but the amplitudes are actually determined by the first few modes. Arai and Tokimatsu (2000) suggested that fourth mode at least should be calculated. We adopt to calculate third mode because the lower amplitudes of higher modes over 3 may have a very limited effect on the short period range, e.g., shorter than 0.2 s. As the Q value related to the attenuation can not be identified from the microtremor H/V spectral ratio, the following three identification schemes are conducted to determine the optimal velocity structures. That is (a) only identifying the Vs from surface to bedrock, (b) identifying the Vs in the shallow layers and thicknesses in the deep layers, (c) identifying the Vs and thickness of each layer from surface to bedrock. The other parameters are fixed to be the same as the initial values.

We again identify the velocity structures at MYG006, not from earthquake H/V spectral ratio but from microtremor H/V spectral. The target period range is still set to be from 0.05 s to 2.0 s. Fig. 3.13 shows the fitting between theoretical and observed H/V spectral ratios, and the dispersive curves and response functions for each mode of surface waves. It can be seen that the theoretical H/V spectral ratio match well with the observed one, which suggests that the identified velocity structures are reasonable. Besides, the amplitude of theoretical H/V spectral ratio incorporating higher modes of surface waves obviously decrease compared with that of fundamental mode. Also the response functions for higher modes over 2 are quite smaller than that of fundamental and first mode, which suggests that it is reasonable to only incorporate the first 3 modes. Fig. 3.14 shows the identified underground velocity structures. It can be seen that the predominant period of the theoretical H/V spectral ratio for initial model is shorter than the observed one. Therefore, smaller velocity in the shallow layers of the identified velocity structures leads to the right shift of predominant period of H/V spectral ratio, which again suggests the identified velocity structures are reasonable. In addition, the transfer functions for S- and P-wave are also calculated with the identified velocity structures listed in Table 3.4 and the assumed Q value ($Q_S = V_S/20$ and $Q_P = Q_S/2$).

It can be found that the transfer function for S-wave is quite large from about 0.2 s to 2.0 s.

Table 3.4 Identified underground velocity structures from microtremor H/V spectral ratio at MYG006

$\rho(ton/m^3)$	$V_S(m/s)$	$V_P(m/s)$	H(m)	Depth(m)
1.42	126.0	1429.8	0.8	0.8
1.42	84.8	1384.1	1.6	2.4
1.75	110.1	1412.2	3.7	6.1
1.75	136.0	1441.0	4.1	10.1
1.75	169.8	1478.5	7.2	17.3
1.85	226.1	1541.0	3.9	21.2
1.90	261.8	1580.6	14.2	35.4
2.00	363.9	1693.9	14.2	49.6
2.00	466.6	1807.9	9.0	58.6
2.10	422.1	1758.5	17.4	76.0
2.15	1243.7	2670.5	151.3	227.4
2.25	1084.8	2494.1	156.9	384.3
2.30	1104.4	2515.9	237.3	621.6
2.35	1423.7	2870.3	734.2	1355.8
2.40	2557.0	4449.2	735.9	2091.7
2.50	2828.2	4921.1	1822.8	3914.5
2.50	3100.0	5500.0	0.0	3914.5

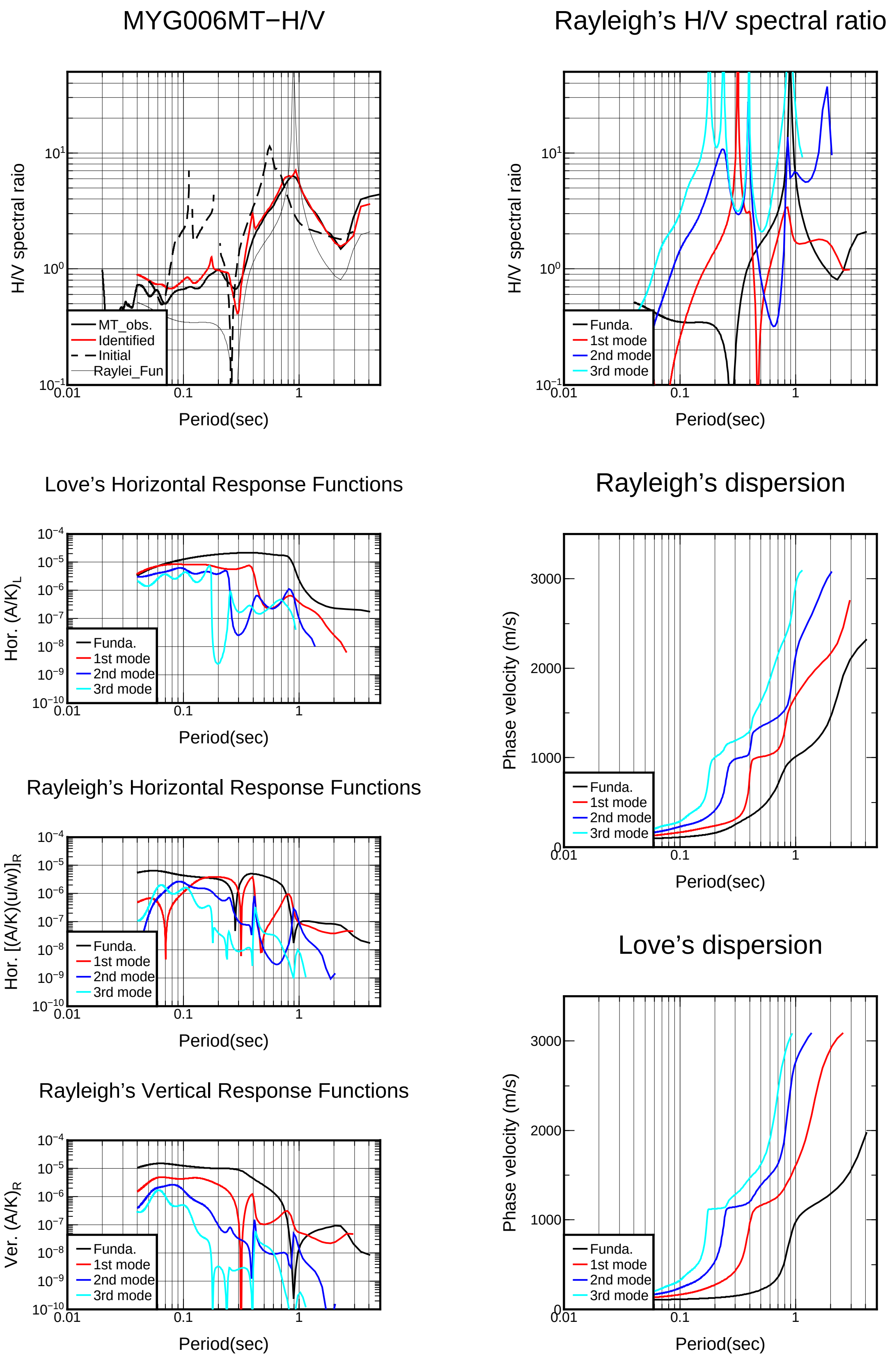

Fig. 3.13 The dispersive curves and response functions of surface waves calculated with the identified underground velocity structures at MYG006

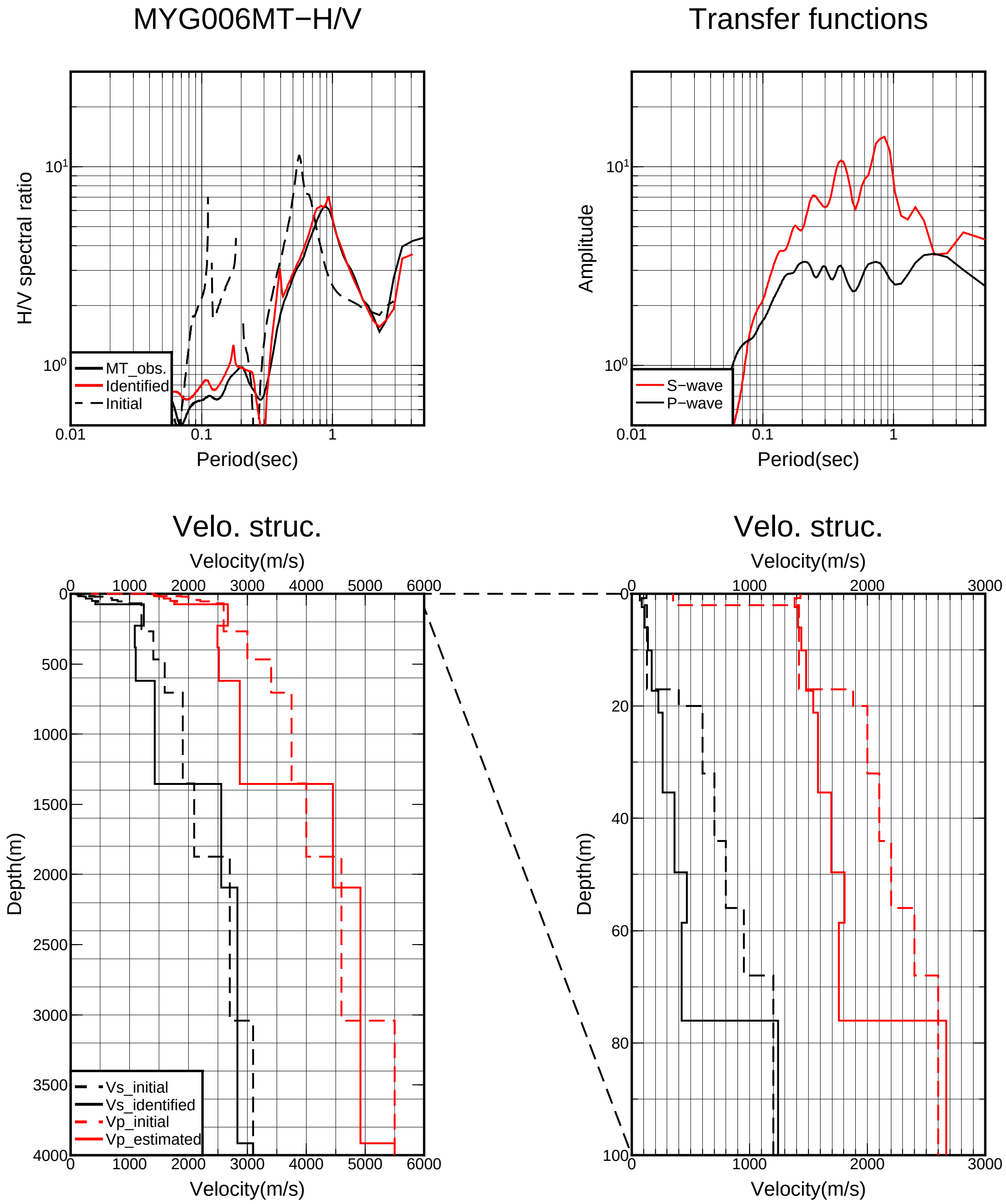

Fig. 3.14 Identification of underground velocity structures at MYG006 from microtremor H/V spectral ratio

3.2.3 Comparison of underground velocity structures identified from H/V spectral ratios of earthquake motions and microtremors

We have obtained two sets of the velocity structures identified from two kinds of H/V spectral ratio at the same site, MYG006, so we compare them in Fig. 3.15. It can be seen that these two sets of identified underground velocity structures are almost the same in shallow layers (about 20 m in the depth), although the velocity structures in deep layers are quite different. Moreover, the transfer functions for S-wave calculated with the identified underground velocity structures are almost the same as each other in the target period range (0.05 s∼3.0 s). It can be explained that the transfer functions in the target period range are mainly determined by the underground velocity structures in the shallow layers. In addition, the bedrock motions estimated with these two underground velocity structures from the same observed surface motions by Eq. (3.2) are also compared, as shown in Fig. 3.16. The consistency for the waveforms and Fourier spectra indicates that the underground velocity structures can be identified from any one of the H/V spectral ratios, either earthquake or microtremor. It also implies that the ground motions may be estimated with the underground velocity structures identified from microtremor H/V spectral ratios at those sites where strong-motion stations were not installed.

Without the loss of generality, the underground velocity structures identified from both earthquake and microtremor H/V spectral ratios are compared at other four sites, as well as the transfer functions. We can conclude from the results that the transfer functions calculated with identified velocity structures from microtremor H/V spectral ratios are in agreement with those calculated with identified velocity structures from earthquake H/V spectral ratios, although the identified velocity structures are different in deep layers.

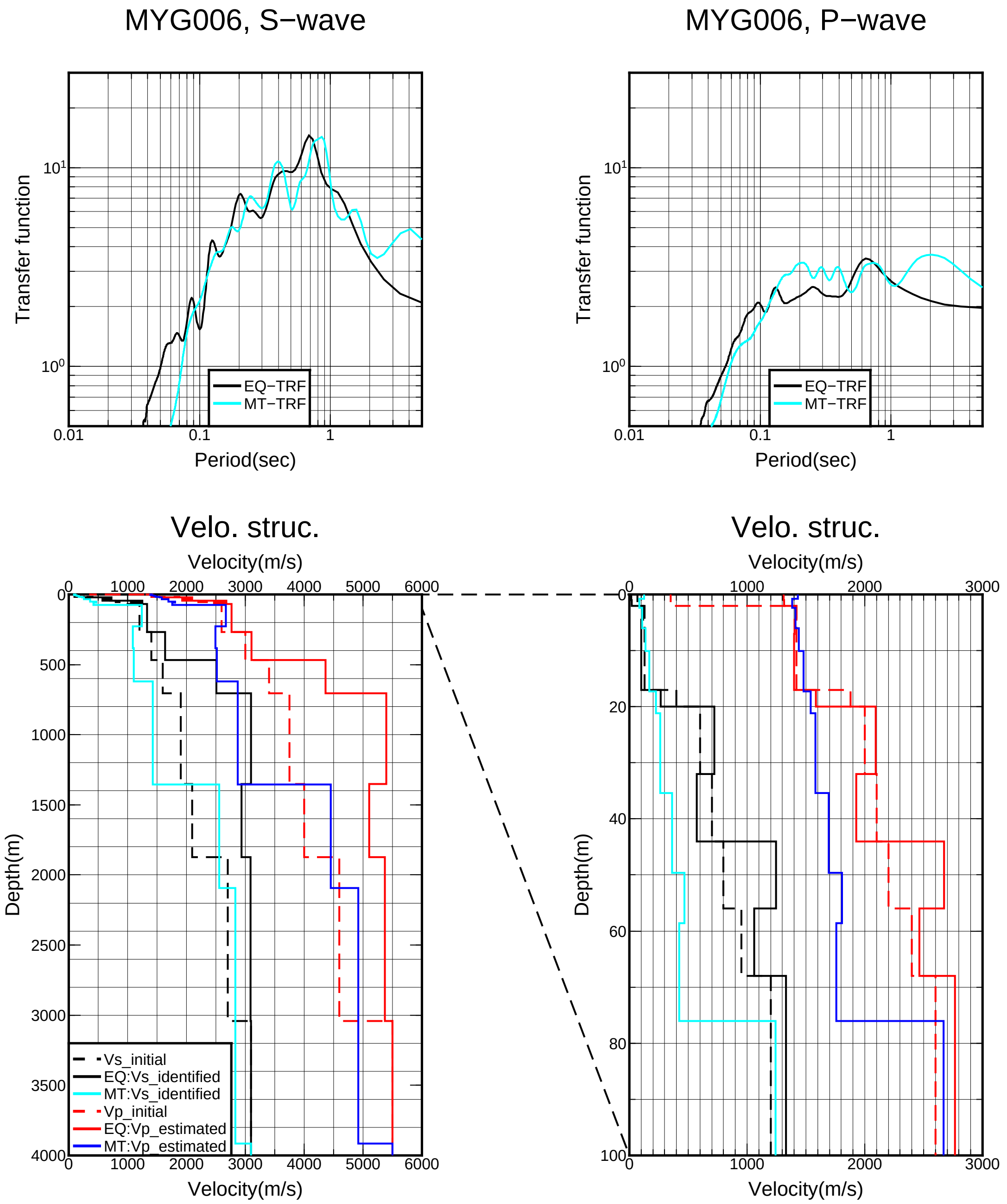

Fig. 3.15 Comparison of underground velocity structures and transfer functions at MYG006

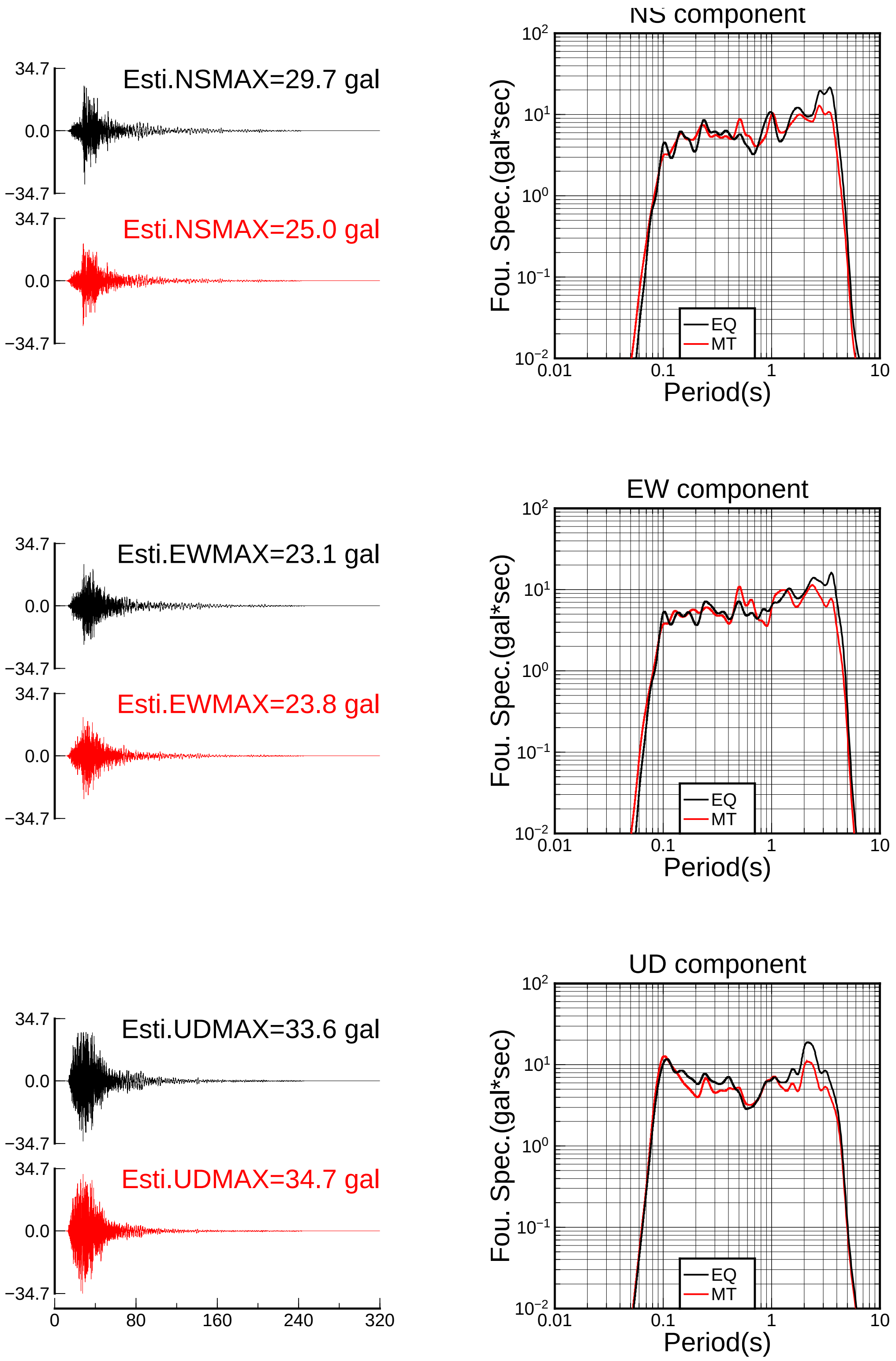

Fig. 3.16 Comparison of the acceleration waveforms and Fourier spectra on the bedrock of MYG006. Black and red ones correspond to the estimated motions by use of identified velocity structures from H/V spectral ratio of earthquake motions and microtremor respectively. The surface motions are observed during the 2005 Miyaki-Oki earthquake

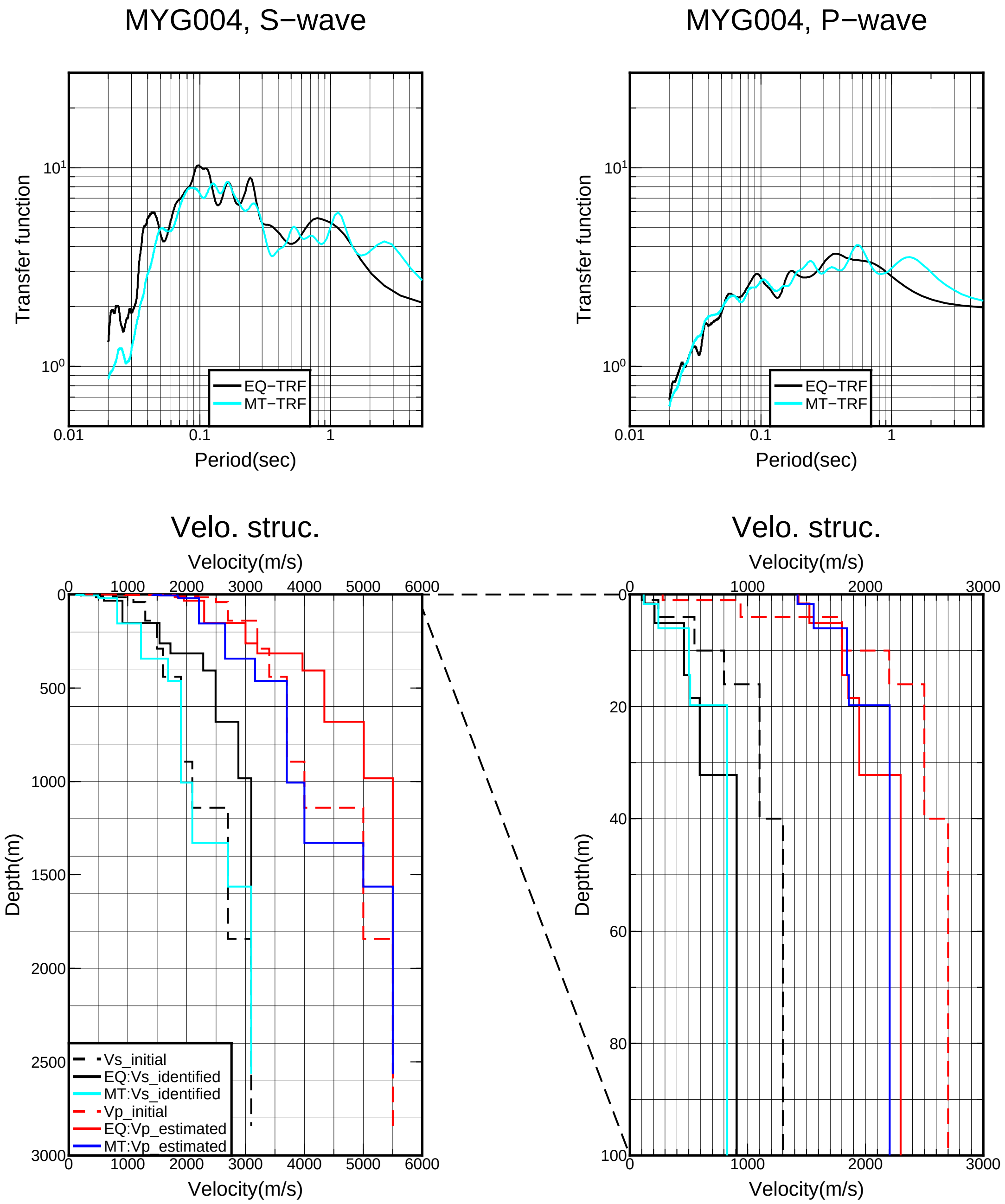

Fig. 3.17 Comparison of underground velocity structures and transfer functions at MYG004

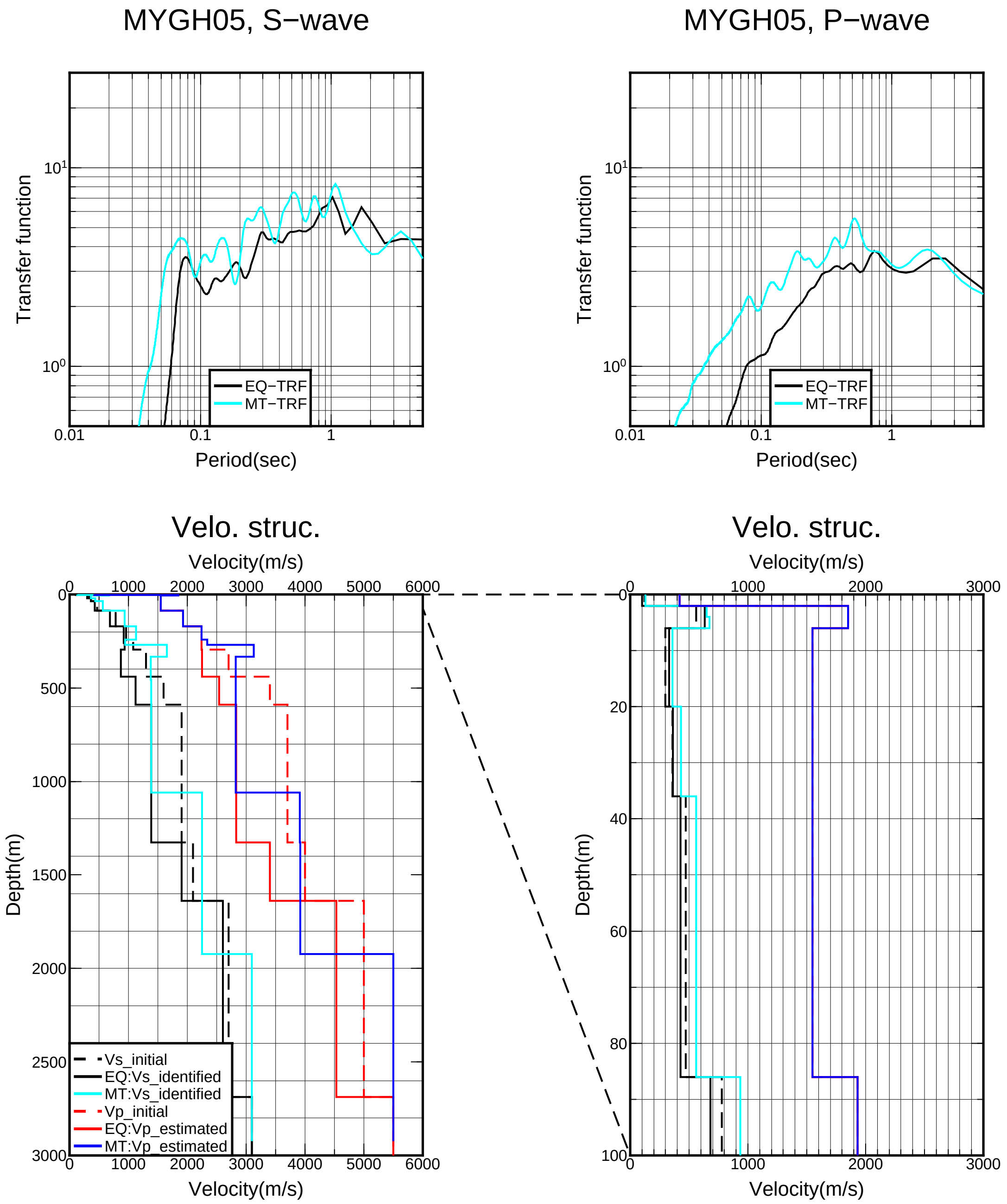

Fig. 3.18 Comparison of underground velocity structures and transfer functions at MYGH05

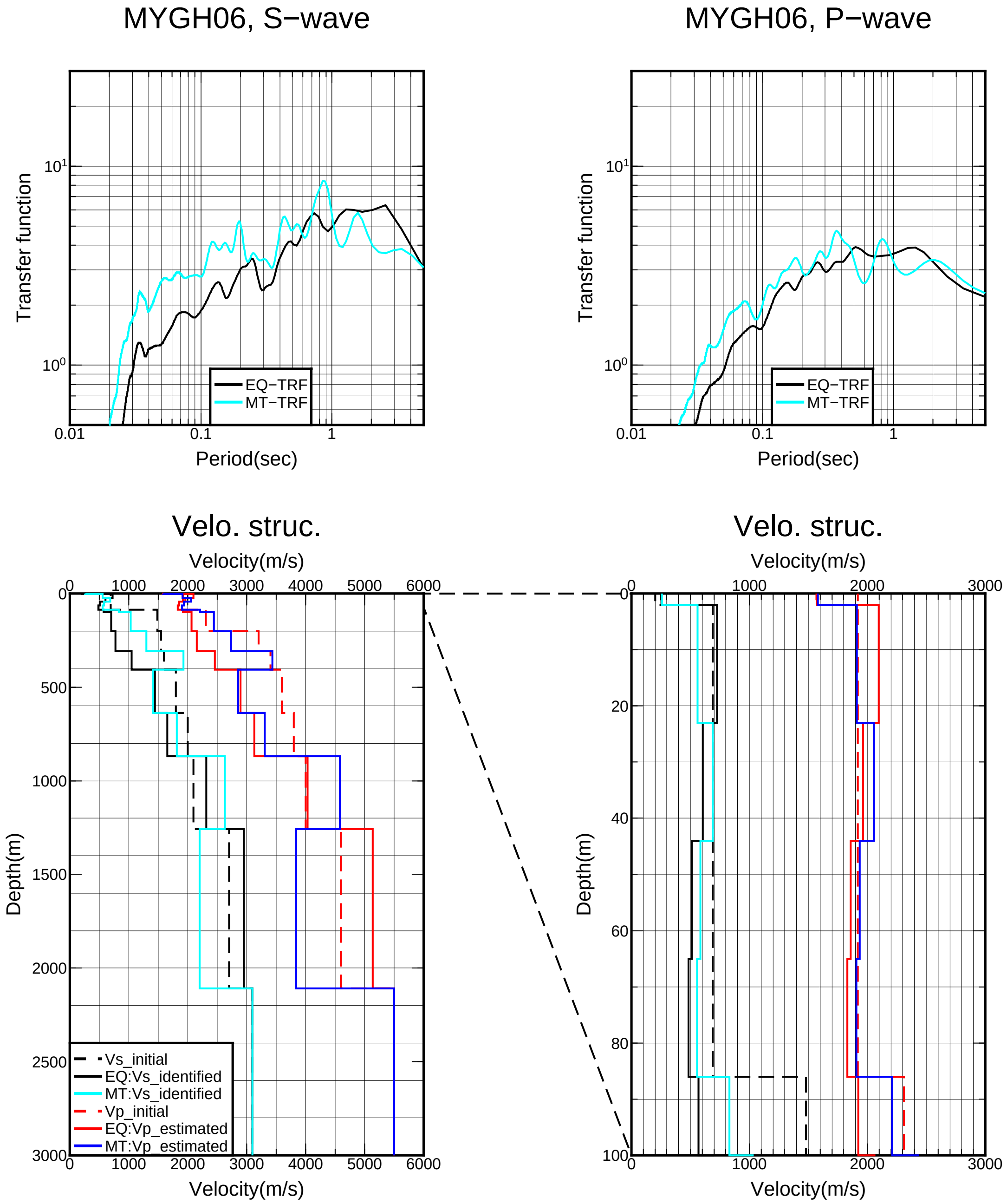

Fig. 3.19 Comparison of underground velocity structures and transfer functions at MYGH06

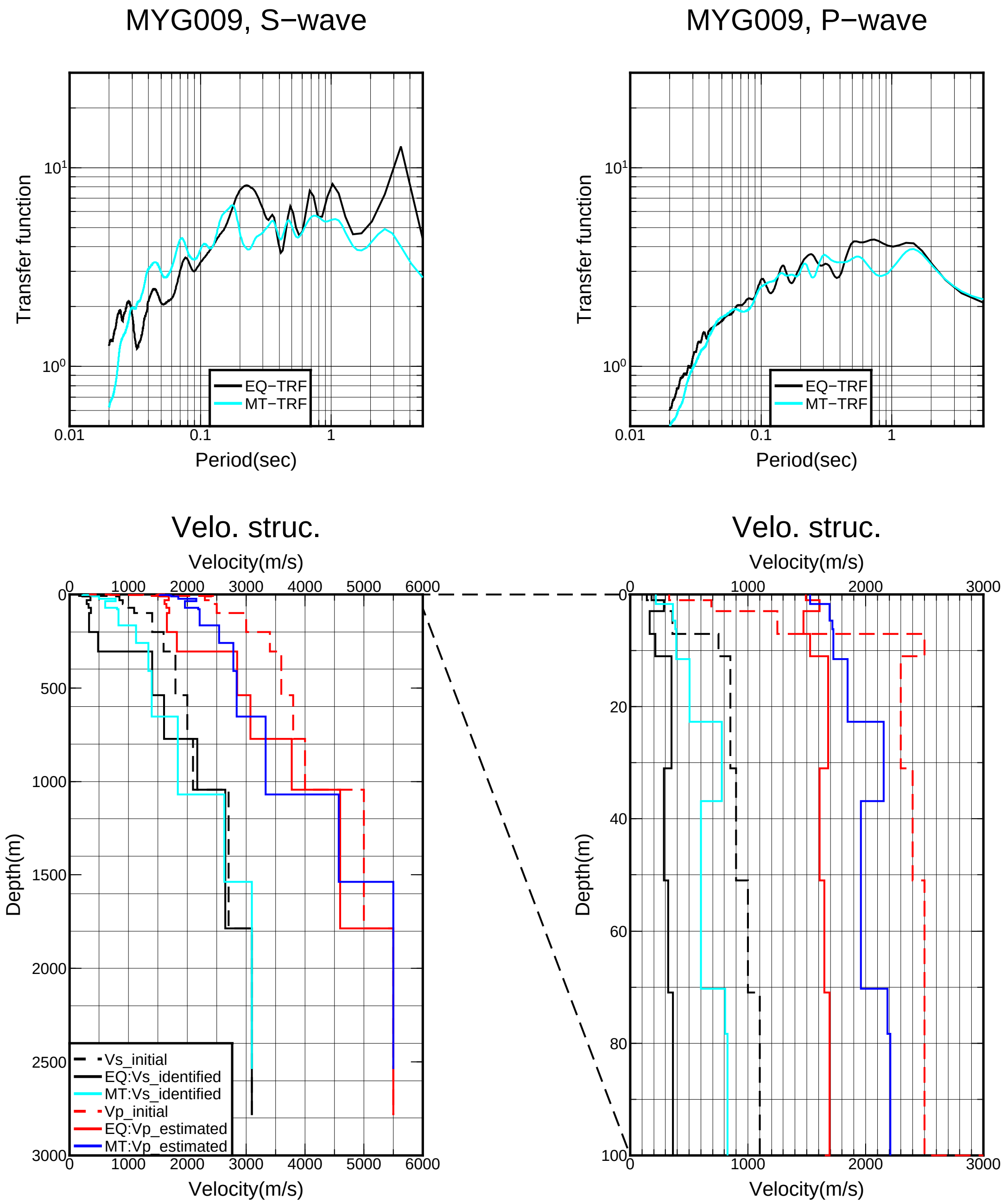

Fig. 3.20 Comparison of underground velocity structures and transfer functions at MYG009

3.3 Verification of estimating ground motions at strong-motion stations

We have verified that the underground velocity structures identified from microtremor H/V spectral ratio are reliable, but it is necessary to verify whether the underground velocity structures at two adjacent sites can be used to estimate the ground motions. Just as shown in Fig. 3.1, we can estimate the bedrock motions at one strong-motion station and then estimate the surface motions at the other strong-motion station with the estimated bedrock motions. The transfer functions at these two strong-motion stations will be evaluated with the underground velocity structures both identified from microtremor H/V spectral ratio. Then we can confirm whether the identified underground velocity structures is suitable for estimating ground motions through comparing the estimated ground motions with the observed ones on the surface of the strong-motion station. On the other hand, for the mainshock, we need to verify whether both the underground velocity structures and source model is applicable for estimating ground motions.

3.3.1 Verification of estimating ground motions for small earthquakes

We will verify the estimation method with the underground velocity structures identified from microtremor H/V spectral ratios at several strong-motion stations shown in Fig. 3.21 during small earthquakes in this subsection. First, we estimate the bedrock motions at MYG006 shown in Fig. 3.22 with the identified underground velocity structures from the surface motions during a small earthquake which was an $M_{JMA}6.3$ event occurred in the depth of 46 km at 3:51 on July 25, 2011. We use this kind of small earthquake because the epicenter is far away any of the strong-motion stations to satisfy the common bedrock assumption. Then we estimate the surface motions at the surrounding strong-motion stations, e.g., MYGH05 shown in Fig. 3.23 and MYG004 shown in Fig. 3.24. It can be seen that not only the acceleration waveforms but also the Fourier spectra in three components of the estimated ground motions are consistent with those of the observed ones, which indicates that the underground velocity structures identified from microtremor H/V spectral ratios are reliable and also the proposed estimation method is effective for small earthquakes.

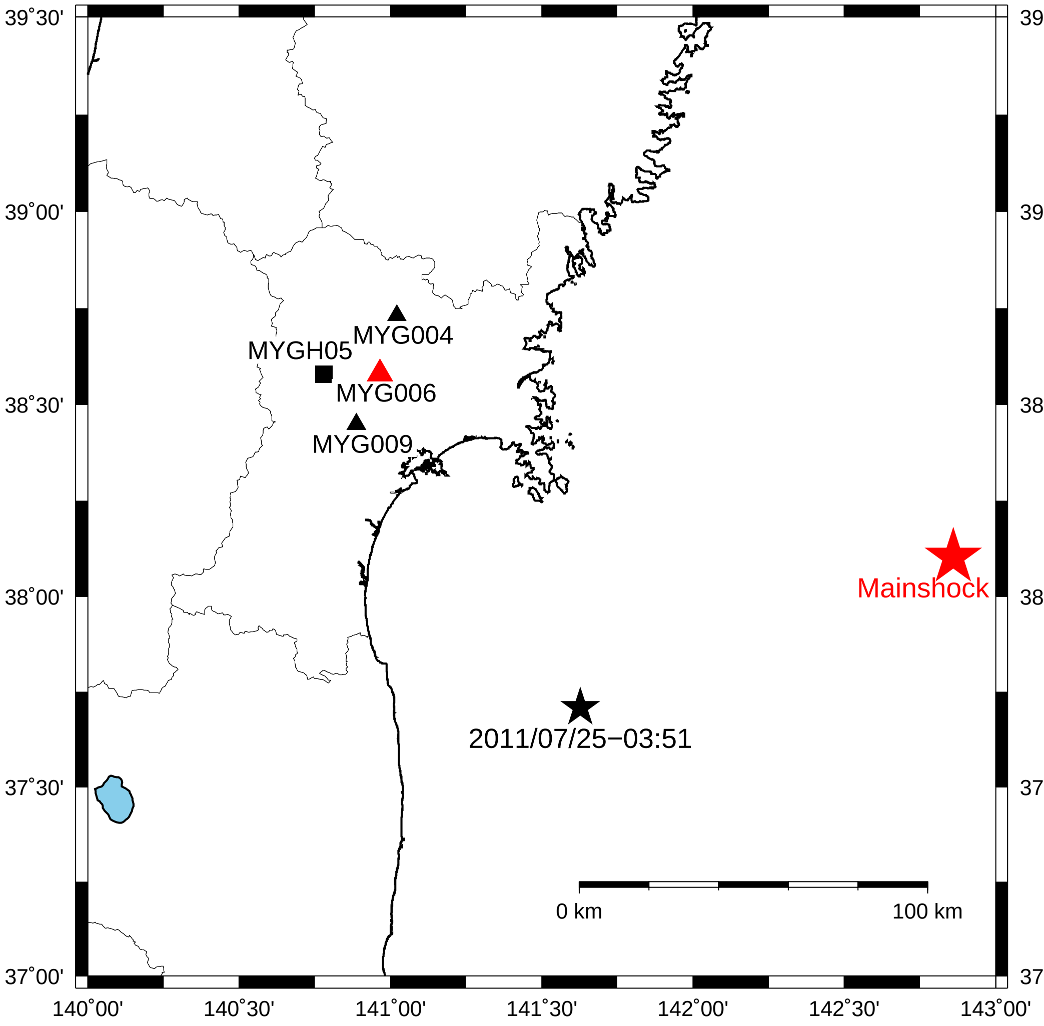

Fig. 3.21 Location of epicenters for a small earthquake and mainshock

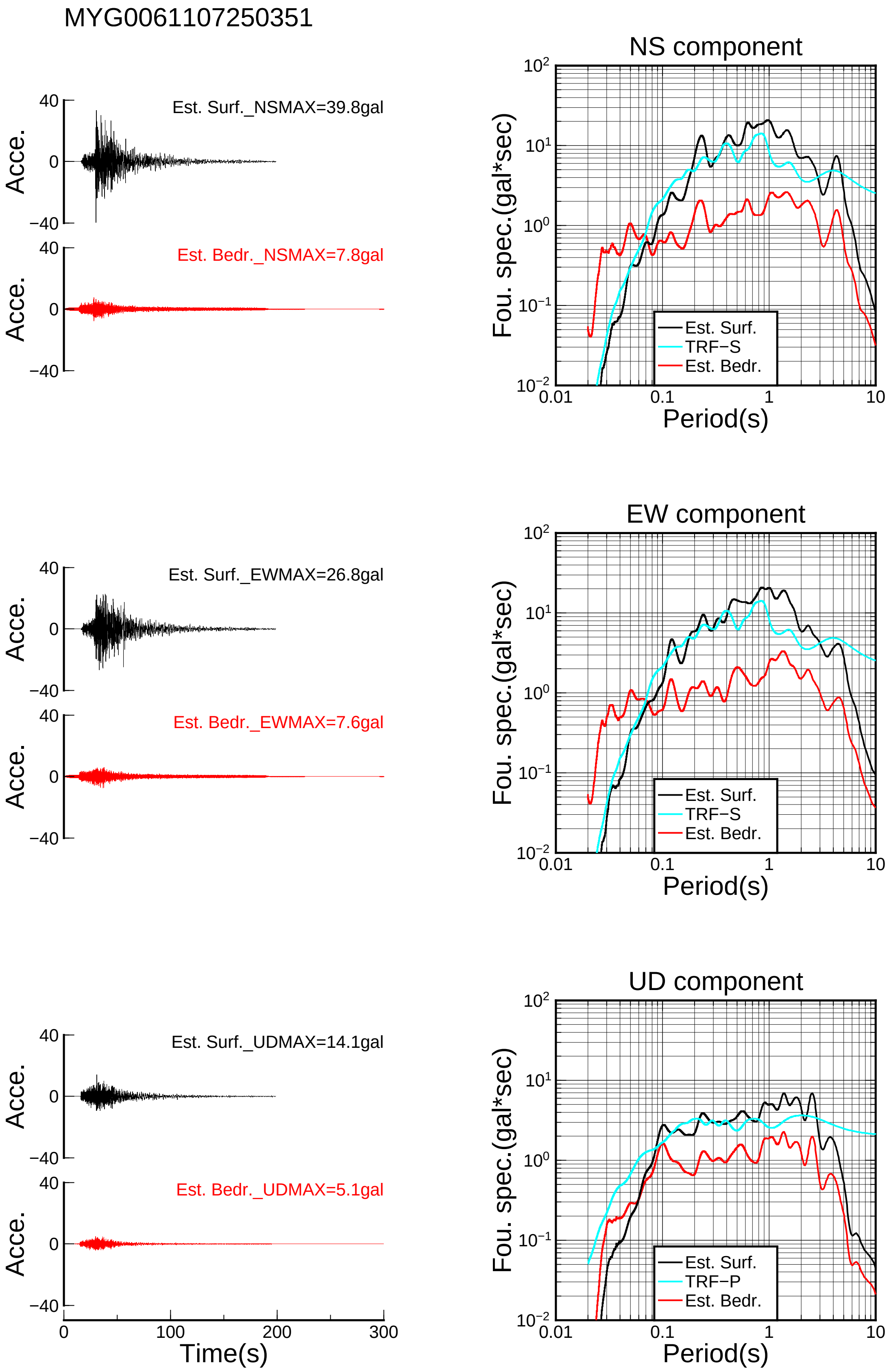

Fig. 3.22 Bedrock motions at MYG006 during a small earthquake occurring at 3:51 on July 25, 2013

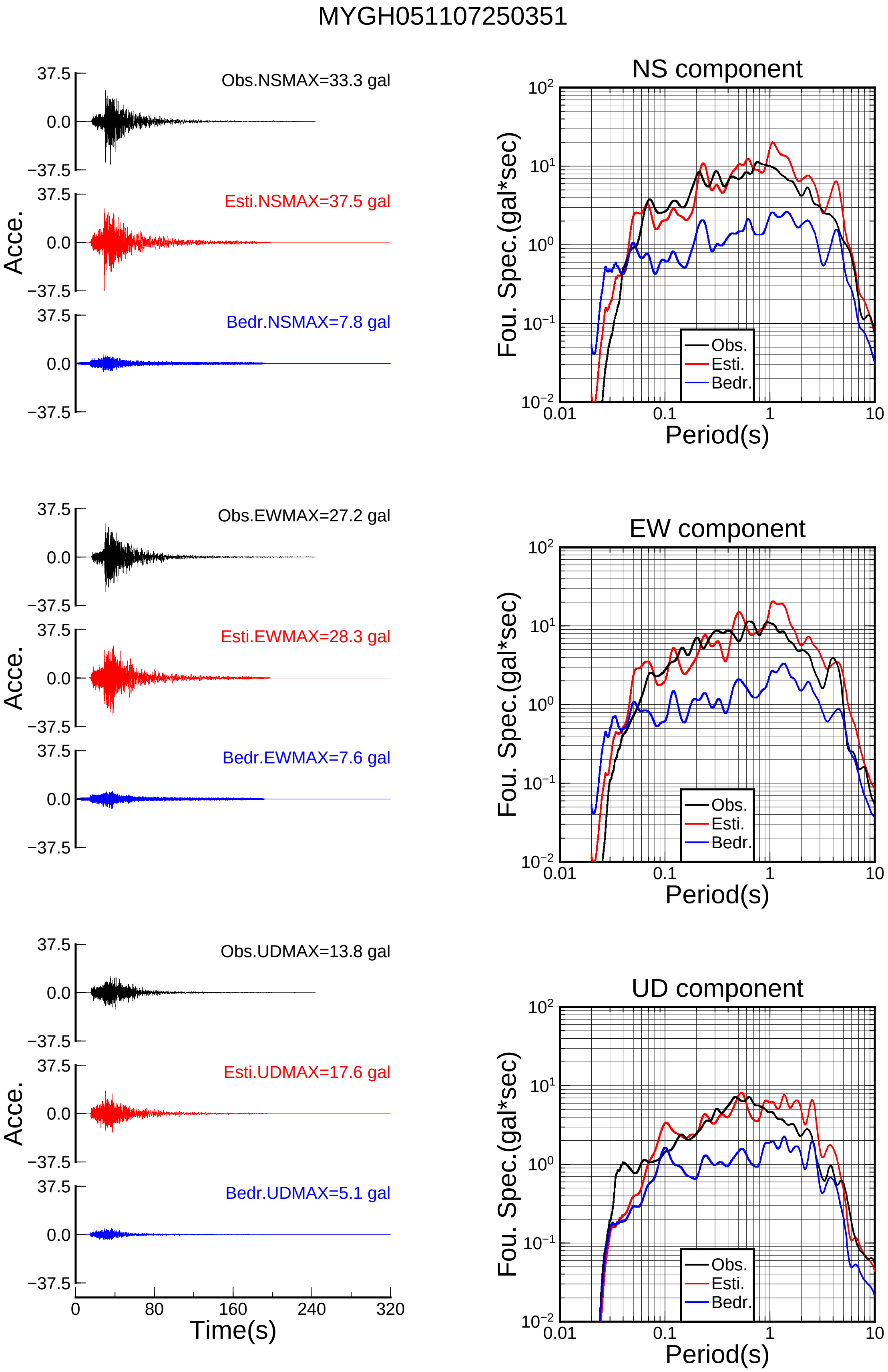

Fig. 3.23 Surface motions estimated at MYGH05 during a small earthquake occurring at 3:51 on July 25, 2013

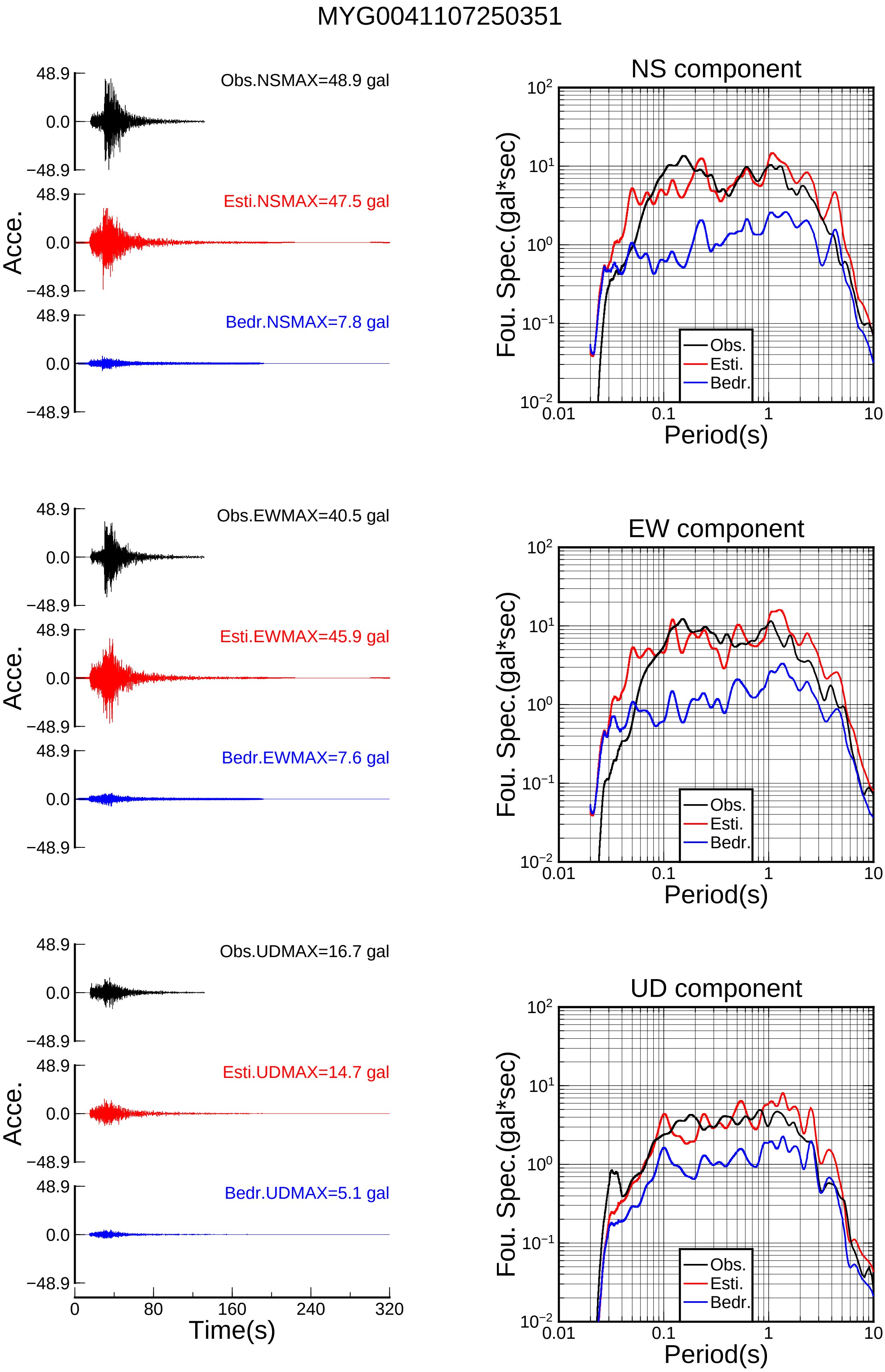

Fig. 3.24 Surface motions estimated at MYG004 during a small earthquake occurring at 3:51 on July 25, 2013

3.3.2 Verification of estimating ground motions during the mainshock

During the mainshock, the soft soil near the surface at some sites may behave nonlinear, so it is not advisable to directly estimate the bedrock motions from the surface motions of mainshock. We propose that the bedrock motions are estimated from the surface motions during the specified small earthquake, then they are synthesized into the bedrock motions for the mainshock with the underground velocity structures and source model. The ground motions during the mainshock can be estimated from the synthesized bedrock motions at those sites under the common basement assumption. In order to demonstrate the effectiveness of the proposed method, we apply this method among several strong-motion stations as shown in Fig. 3.21. As for the source model, we adopt the short-period (0.1 s $\sim$ 10.0 s) one developed by Kurahashi and Ikikura (2013) which is regarded as one of the most suitable models for the mainshock. From the Fig. 3.25, we can see the source model is composed of five strong motion generation areas (SMGAs) during the mainshock.

As the MYG006 strong-motion station where the bedrock motions will be synthesized is close to the SMGA1 $\sim$ SMGA3, the other two SMGAs may have little effect on the final result, we finally decide to synthesize the bedrock motions for the mainshock only using SMGA1, SMGA2 and SMGA3. The bedrock motions during the small earthquake, i.e., the 2005 Miyagi-Oki earthquake occurring at 11:46 on August 16, have been estimated as shown in Fig. 3.16. Then they are used to synthesize the bedrock motions for the mainshock. The left panels in Fig. 3.25 show the synthesized waveforms corresponding to the three SMGAs, we can see the onset time of the first wave packet comes first from the SMGA1 which is closest to MYG006, the onset time for the other two wave packets are almost the same as the distance between SMGA2 and MYG006 is almost the same as that between SMGA3 and MYG006. The bedrock motions for the mainshock are the superposition of these three synthesized motions in each component, as shown in Fig. 3.26. It can be seen that the bedrock motions for mainshock are significantly amplified compared with those of small earthquake. Then the synthesized bedrock motions are used to estimate the surface motions of MYGH05 and MYG009 stations shown in Fig. 3.27 and Fig. 3.28. It can be seen that both the acceleration waveforms and Fourier spectra are in good agreement with the observed ones in the NS and EW components, and the accuracy for estimated ground motions in the UD component both at MYGH05 and MYG009 is not so satisfactory. For the small earthquake, the estimated ground motions in the UD component at MYGH05 are almost the same as the observed ones as shown in Fig. 3.23, which indicates that the identified underground velocity structures at MYGH05 are reliable. The reason for the larger estimated ground motions in the UD components during the mainshock may caused by the less accuracy of source model in the UD component.

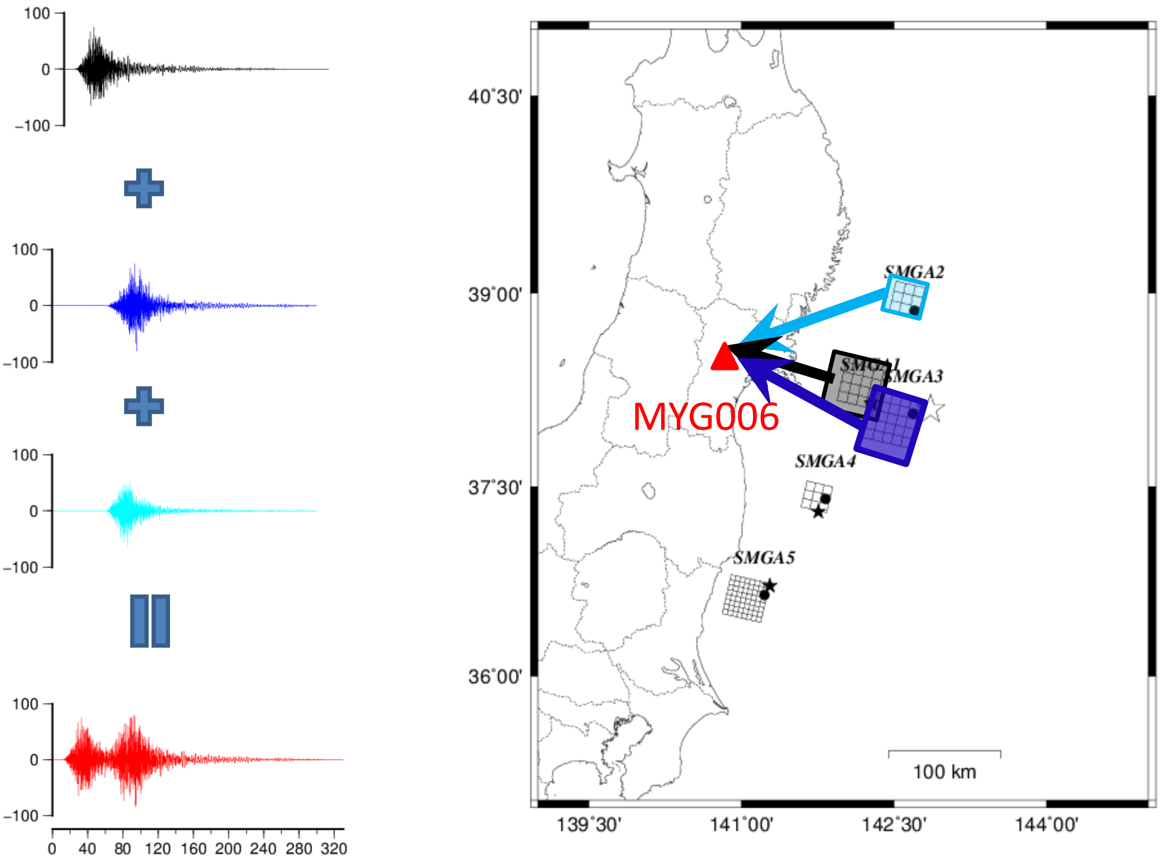

Fig. 3.25 Estimated incident motions in the NS component at the bedrock of MYG006 during the mainshock with the short-period source model (Kurahashi and Ikikura, 2013)

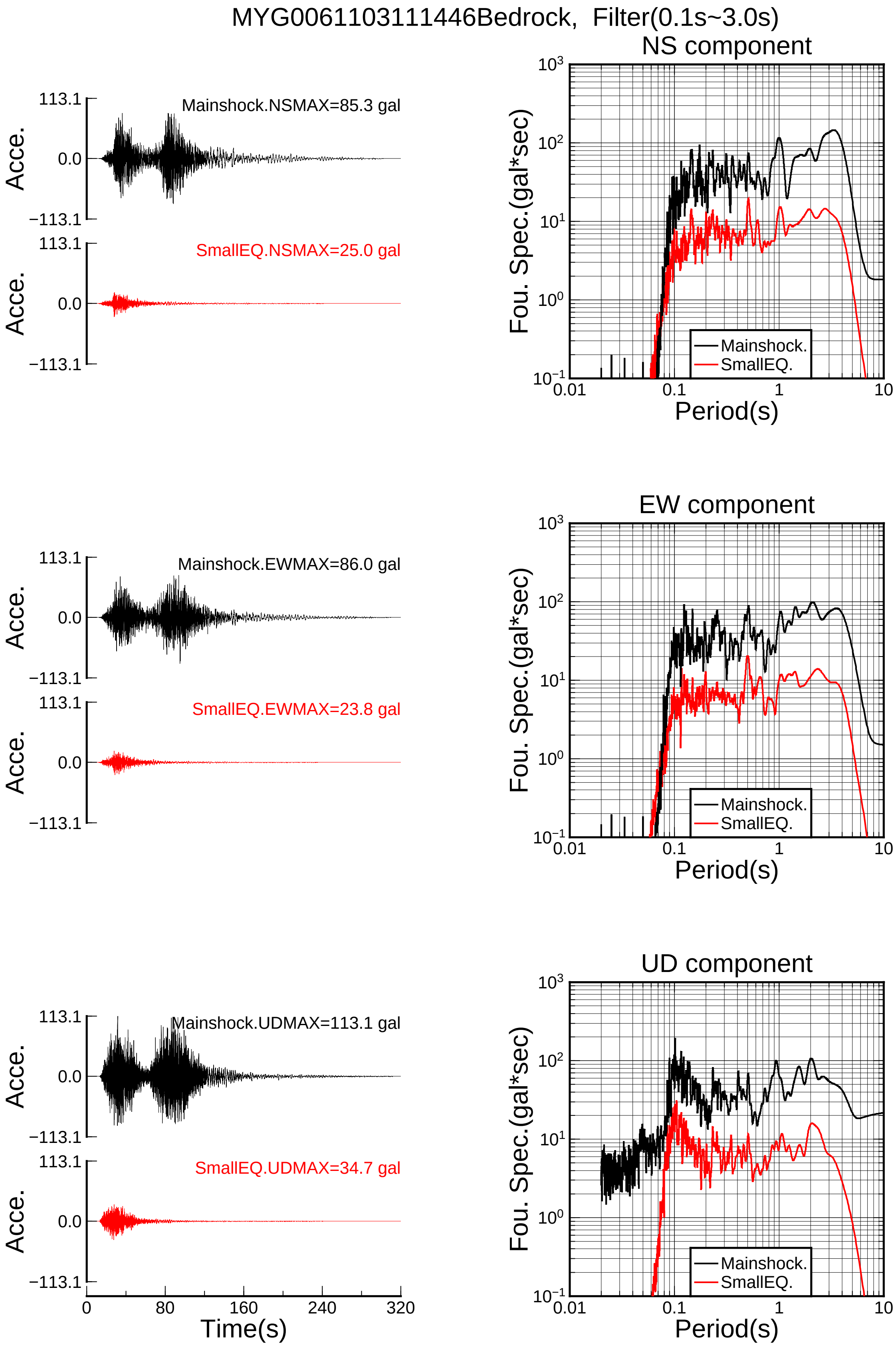

Fig. 3.26 Estimated of bedrock motions in three components at MYG006 during the mainshock. The Fourier spectra are smoothed with the parzen window of 0.1 Hz

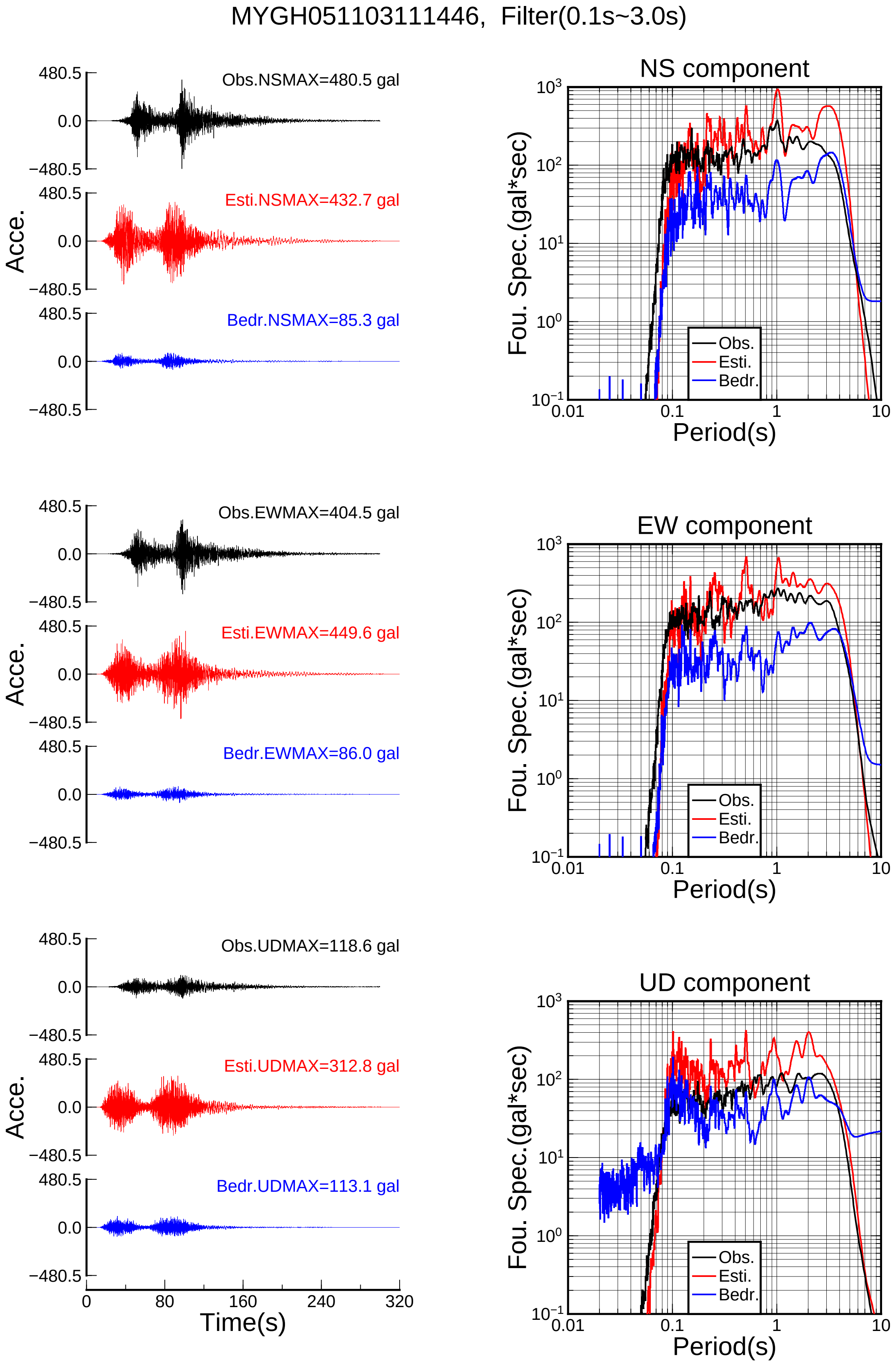

Fig. 3.27 Comparisons of estimated surface motions with observed surface motions at MYGH05 during the mainshock. The Fourier spectra are smoothed with the parzen window of 0.1 Hz

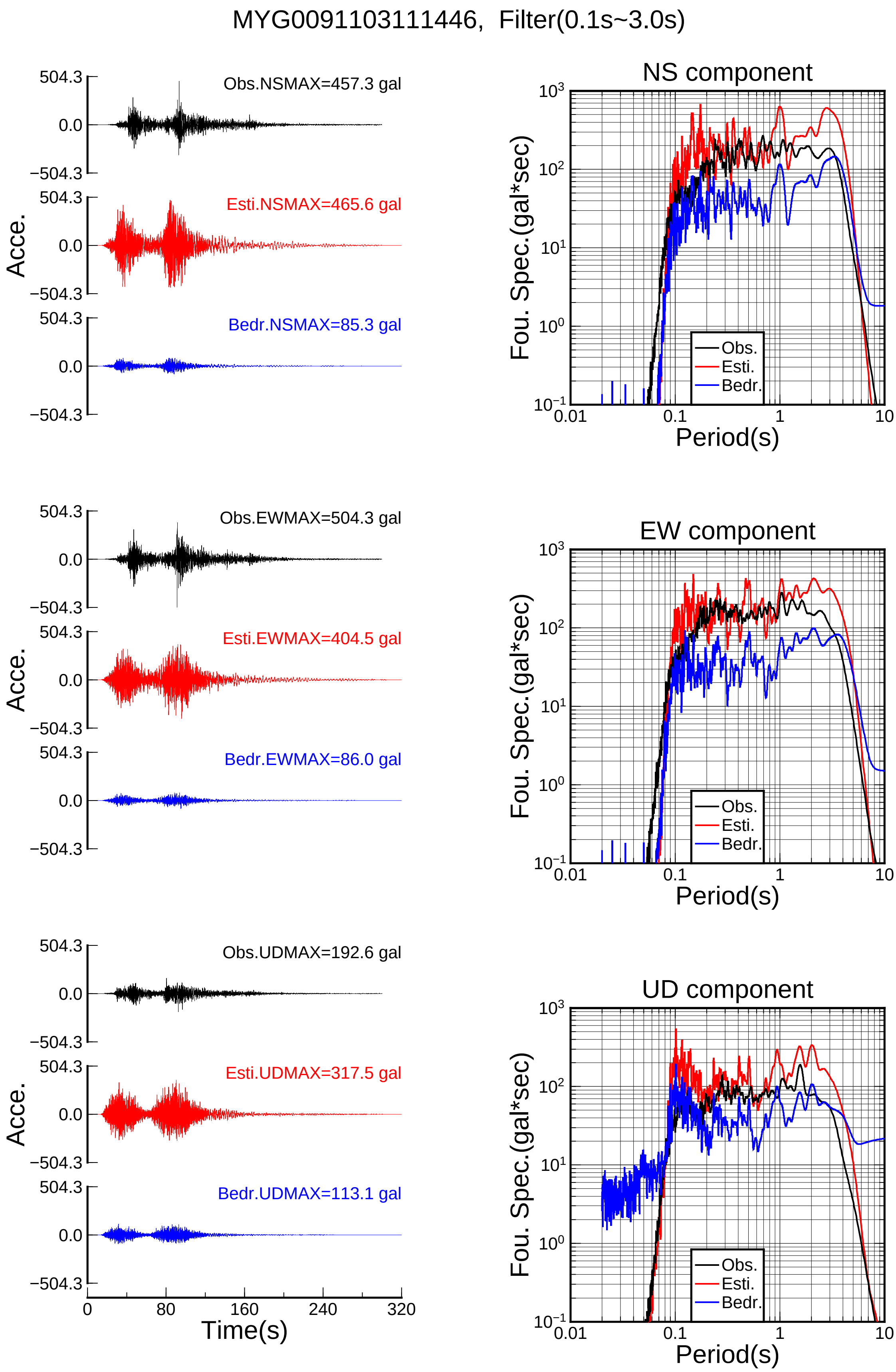

Fig. 3.28 Comparisons of estimated surface motions with observed surface motions on the surface at MYG009 during the mainshock. The Fourier spectra are smoothed with the parzen window of 0.1 Hz

In addition, during the mainshock, nonlinear behaviour inevitably occurs at those sites with soft layers near the surface. Fig. 3.29 shows a comparison of earthquake H/V spectral ratios between the small earthquakes and mainshock. It can be seen that the right shift of the predominant period in the short period range for the earthquake H/V spectral ratio during the mainshock occurs compared with that for average small earthquakes H/V spectral ratio, which suggests the soil near the surface behaves nonlinear during the mainshock. On the other hand, the nonlinear behaviour at MYG006 is more obvious than that at MYGH05, which suggests that the estimation method we have verified should not neglect the nonlinear effect at those soft sites like MYG006. Fig. 3.30 shows the estimated surface motions of MYG006 during the mainshock with the synthesized bedrock motions at MYG006. We can find that the Fourier spectra between 0.1 s and 0.5 s is overestimated under the linear assumption compared with those of observed ones. However, the estimated ground motions at other sites, such as MYG009 and MYGH05, do not show obvious difference with the observed ones, which suggests that the estimation method is generally applicable for mainshock. The nonlinear effect which should not be neglected at soft sites is expected to be solved afterwards.

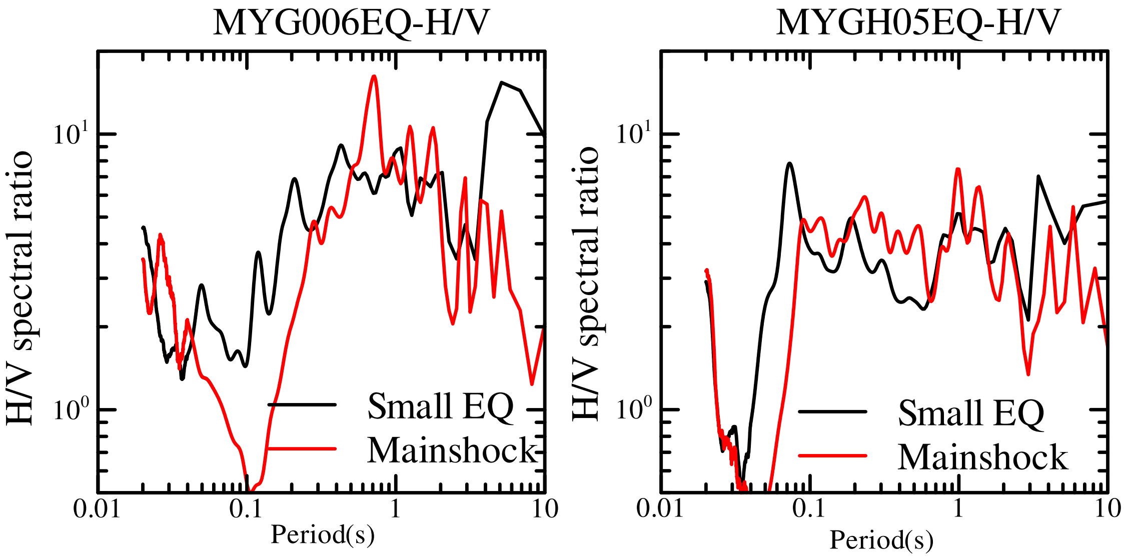

Fig. 3.29 Comparison of earthquake H/V spectral ratios between small earthquakes and mainshock

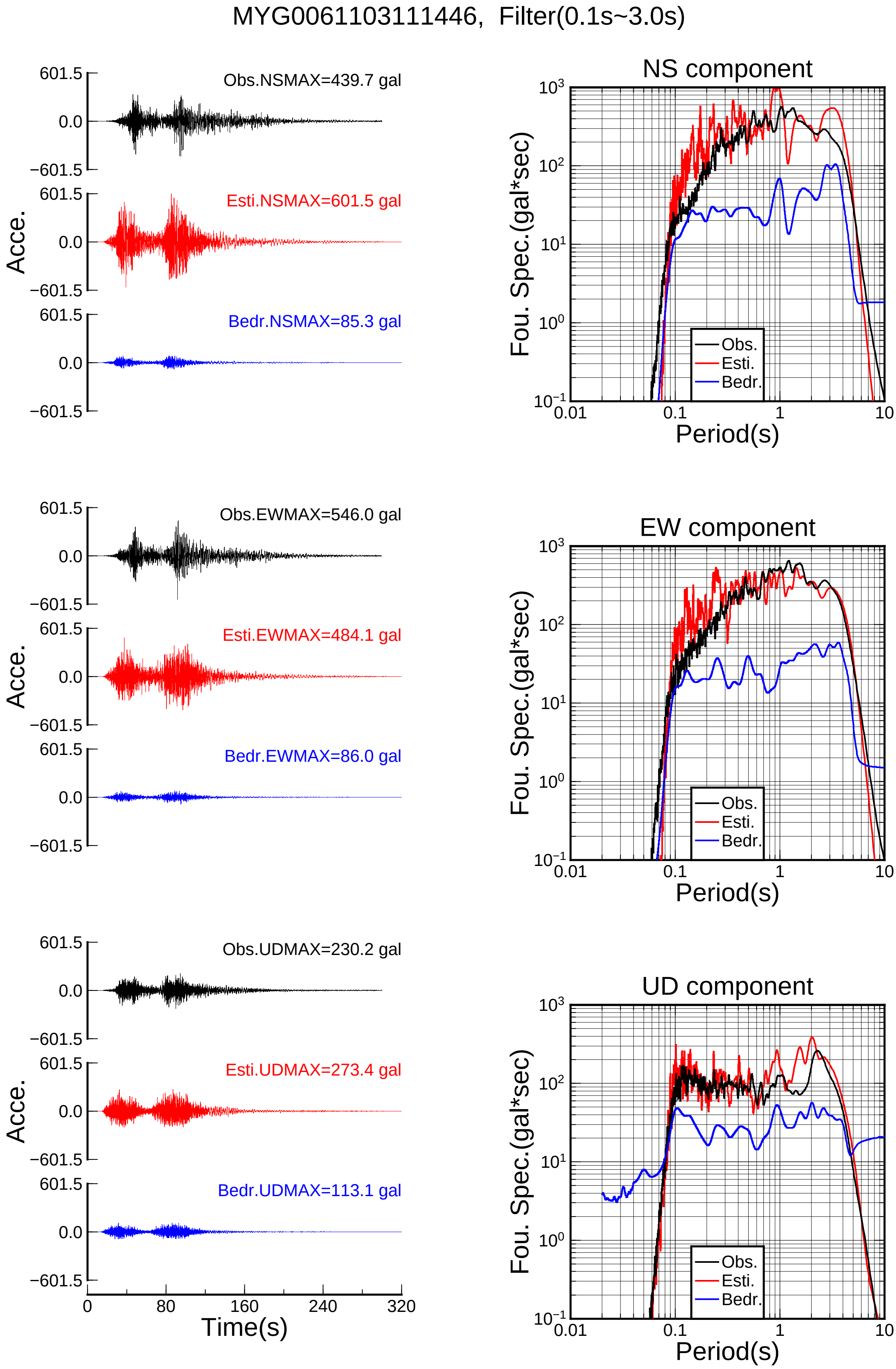

Fig. 3.30 Comparison of estimated surface motions with observed surface motions at MYG006 during the mainshock. The Fourier spectra are smoothed with the parzen window of 0.1 Hz

3.4 Summary

In this chapter, we first presented a method to estimate ground motions at the sites where the microtremors were observed. Next we applied the method to estimate ground motions for small earthquakes with the underground velocity structures identified from the microtremor H/V spectral ratios. Then we applied the method to estimate the ground motions during the mainshock with the identified underground velocity structures and short-period source model. As a result, the following conclusions can be obtained.

The transfer function calculated with underground velocity structures identified from microtremor H/V spectral ratio is almost the same as that calculated with underground velocity structures identified from earthquake H/V spectral ratio, although the identified velocity structures are not always consistent with each other. It suggests that the underground velocity structures can be identified directly from microtremor H/V spectral ratios at any sites, as long as the microtremors are observed.

The underground velocity structures identified from microtremor H/V spectral ratio can be used to estimate ground motions during small earthquakes by confirming the consistency between estimated and observed surface motions.

By use of the short-period source model and the identified underground velocity structures, the bedrock motions estimated from surface ground motions during a specified small earthquake are synthesized to the bedrock motions during the mainshock by the modified empirical Green's function method. The consistency between estimated and observed motions suggests that the method is applicable for the mainshock.

The method of estimating ground motions during the mainshock generally work well at those hard sites. For some sites with soft layers near the surface, the ground motions may be overestimated without concerning the nonlinear effect for the mainshock. The nonlinear calculation is expected to be involved afterwards.

Chapter 4

Fragility curves of buildings based on damage ratios and estimated ground motions in subdistricts of Osaki, Kurihara and surrounding cities near the source fault area during the mainshock

As has been pointed in the chapter 2, the ground motions at the strong-motion stations are not representative at some administrative districts, such as Yabuki town and Osaki city, which affected the accuracy of fragility curves. It is advisable to construct the fragility curves based on the damage ratios and ground motion characteristics in a smaller administrative unit, e.g., subdistricts shown in Fig. 2.11. In this chapter, we aims at obtaining the fragility curves in the stricken subdistricts near the source fault area of mainshock. As there are only a couple of strong-motion stations in the studied area, the ground motions in each subdistrict where strong-motion stations were not installed will be estimated with the proposed method in chapter 3. We anticipate the accuracy of the constructed fragility curves is better than those in chapter 2.

4.1 Microtremor measurement

In order to estimate the ground motions in the subdistricts, we need to know the underground velocity structures at each site. As has been verified in chapter 3, it can be

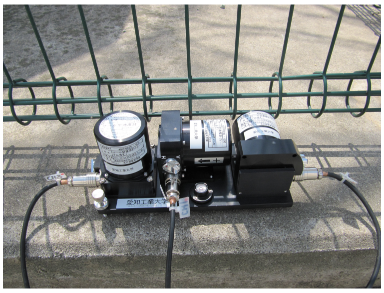

(a) Sentor: VSE-15D-6

(b) Data logger A: SAMTAC-802H

(c) Data logger B: HKS-9550

Fig. 4.1 Photos about measurement instruments including one sensor and two kinds of data loggers

identified from microtremor H/V spectral ratios, so we conducted the microtremor measurement at one site in each subdistrict. Totally, we have conducted the microtremor measurement at 17 sites, including 9 subdistricts in Kurihara city and 6 subdistricts in Osaki city, as well as one site in Wakuya town whose area is approximately equivalent to any of the above subdistricts. The instruments for microtremor measurement are composed of two device, i.e., sensor and data logger. The sensor shown in Fig. 4.1(a) are VSE-15D-6 produced by Tokyo Sokushin CO. LTD. in Japan. It has a high resolution of approximately $2 \times 10^{-8} m/s^2$. The frequency range is from 0.1 Hz to 70 Hz and the maximum measuring range is ± 0.1 m/s. The data logger we used have two types, one is SAMTAC-802H with 6 channels produced by Tokyo Sokushin CO., LTD. in Japan as shown in Fig. 4.1(b), the other is HKS-9550 with 3 channels produced by Keisokugiken Corporation in Japan as shown in Fig. 4.1(c). Both of them have a high resolution of 24bit. Fig. 4.2 is the photos during the measurement at target sites. The duration of each measurement is 30 mins.

(a) Measurement with the sensors in three components and data logger A

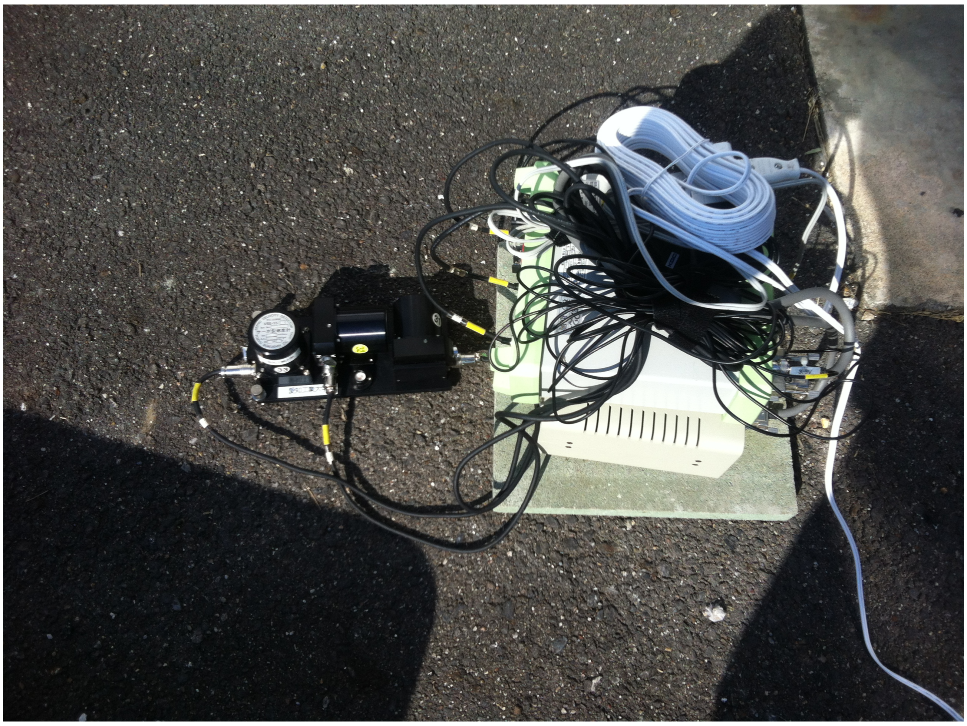

(b) Measurement with the sensors in three components and data logger B

Fig. 4.2 Photos of the microtremor measurement at the target site

In general, we select the streets around which the buildings are concentrated and subjected to damage to some extent due to ground shaking as the target sites. The locations of all the sites are shown in Fig. 4.3 with solid circles and the corresponding geographical information are listed in Table 4.1. It can be seen that the sites where the microtremor measurement was conducted is situated not only at the warm-color area with high amplification factors but also at the cold-color area with relatively low amplification factors. It implies that the ground motions at the sites of warm-color area may different from those at the sites of cold-color area, while the ground motions at the adjacent sites of either warm-color or cold-color areas may be similar to one another. Fig. 4.4 shows the distribution of predominant period from microtremor H/V spectral ratios at damaged sites. It can be seen that the locations of the sites with a predominant period of about 1.0 s are almost consistent with the locations of warm-color areas, such as the sites in the Wakuya town, Kashimadai, Furukawa and Tajiri. It again implies that the ground motions at the sites may be larger than those at other sites.

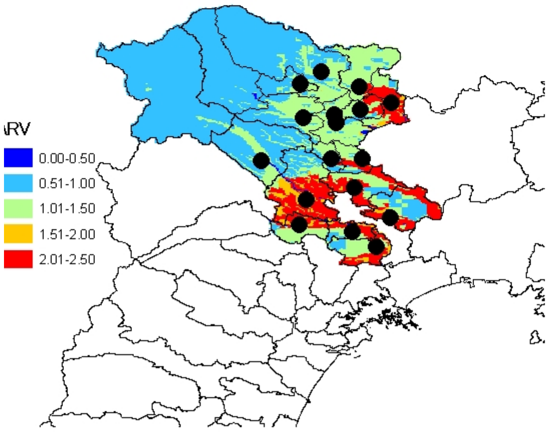

Fig. 4.3 Distribution of amplification factors in the subdistricts of Osaki city, Kurihara city and in the Wakuya town

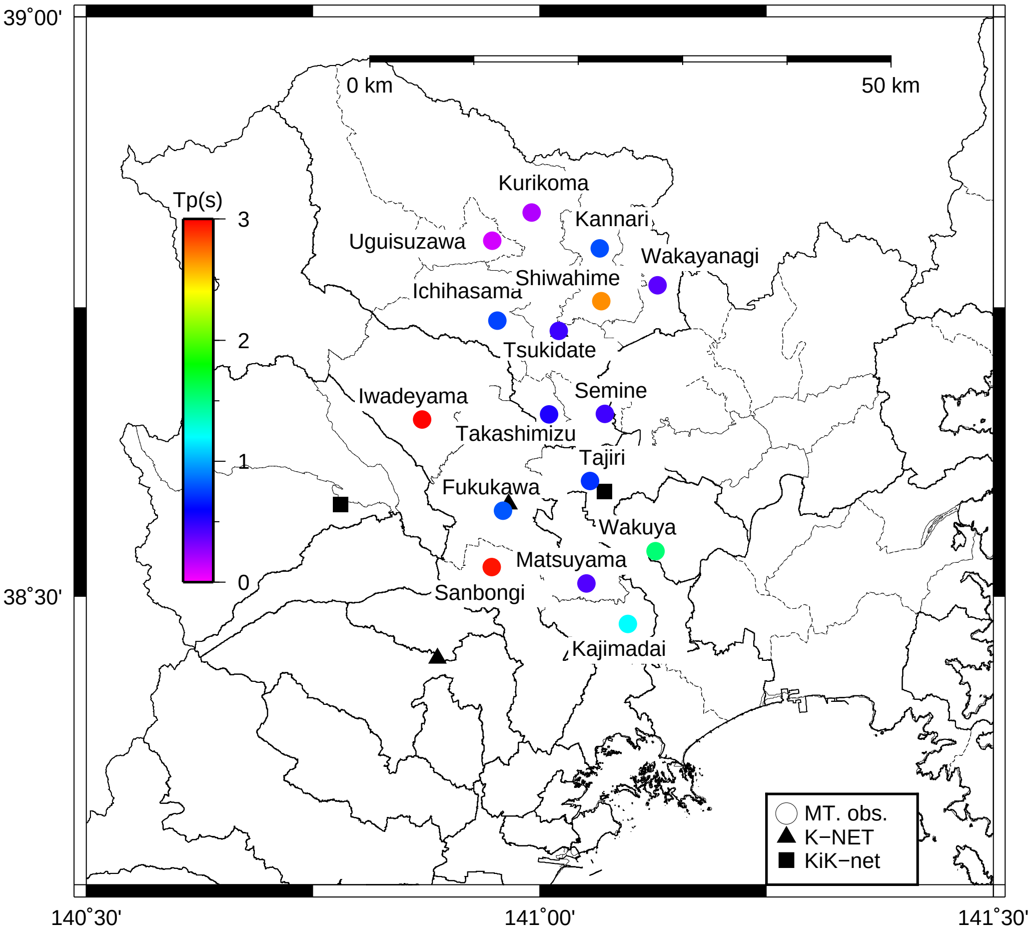

Fig. 4.4 Distribution of predominant period for the observed microtremor H/V spectral ratios in the subdistricts. Triangles and squares denote the strong-motion stations; solid circles denote the sites at which microtremor measurements were conducted; predominant period is obtained through the microtremor H/V spectral ratios from 0.05 s to 3.0 s

Table 4.1 Geographical information and the measurement duration of the damaged sites

Districts	No.	Subdistricts	Latitude(°N)	Longitude(°E)	Duration (min)
Kurihara city	01	Kannari	38.8008	141.0661	30
	02	Korikura	38.8317	140.9908	30
	03	Uguisuzawa	38.8074	140.9476	30
	04	Ichihasama	38.7385	140.9534	30
	05	Tsukidate	38.7294	141.0208	30
	06	Shiwahime	38.7550	141.0676	30
	07	Wakayanagi	38.7688	141.1300	30
	08	Semine	38.6580	141.0719	30
	09	Takashimizu	38.6574	141.0103	30
Osaki city	10	Furukawa	38.5743	140.9597	30
	11	Tajiri	38.6000	141.0556	30
	12	Iwadeyama	38.6531	140.8702	30
	13	Matsuyama	38.5114	141.0515	30
	14	Sanbongi	38.5253	140.9468	30
	15	Kashimadai	38.4818	141.1007	90
Wakuya	16	Wakuya	38.5394	141.1274	150

4.2 Estimation of ground motions at damaged sites during the mainshock

We will apply the estimation method proposed in chapter 3 at the damaged sites where we have conducted the microtremor measurement. We still take the synthesized bedrock motions at MYG006 as the incident motions on the bedrock of all the damaged sites under the common basement assumption which might be suitable if the distance between strong-motion station and any of the damaged sites is sufficiently short compared with that between strong-motion station and the epicenter just as shown in Fig. 4.5. Therefore, the transfer functions at damaged sites are the only unknowns at present, yet they can be obtained from the velocity structures identified from the microtremor H/V spectral ratios.

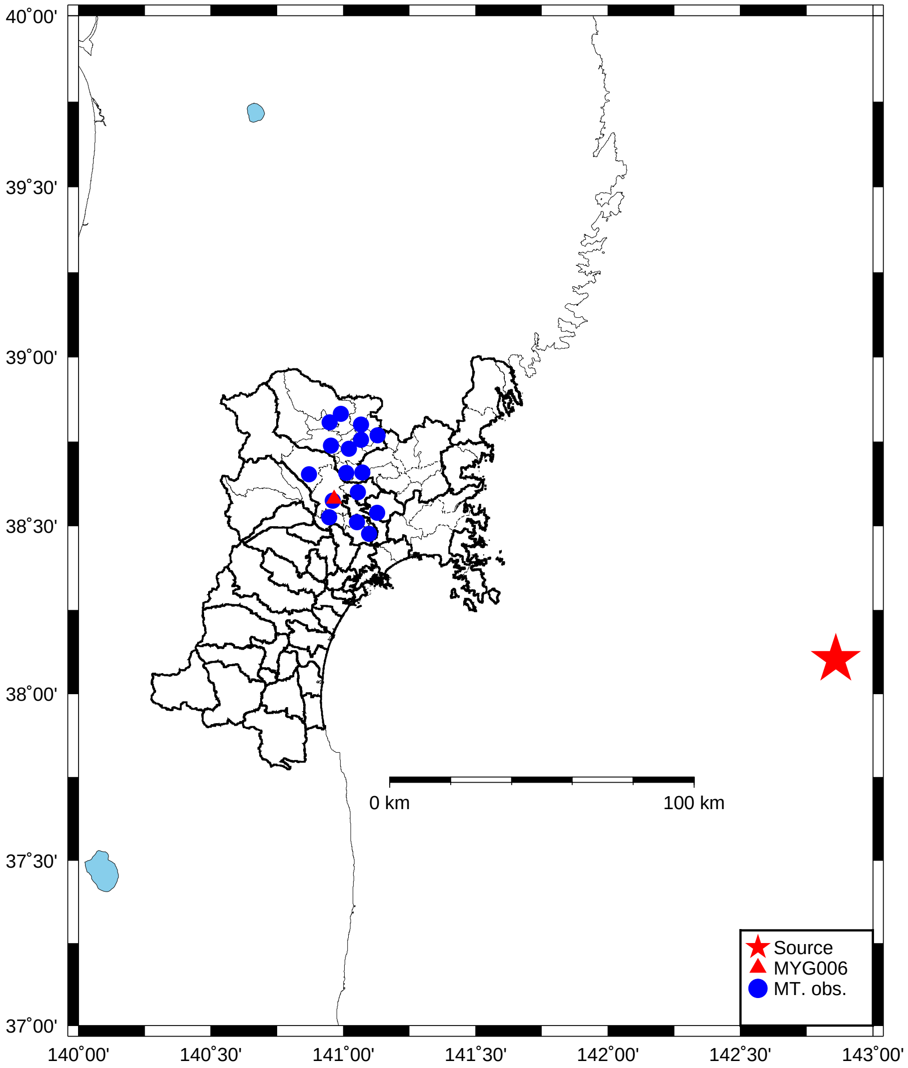

Fig. 4.5 Locations between microtremor observation station and epicenter of mainshock

The identification process is almost the same as that introduced in chapter 3, except the generation of initial velocity structure model. As we do not collect any geological information about the damaged sites, the geological data at adjacent strong-motion stations are used as the initial values in the shallow layers, while for deep layers they can be obtained from the website of J-SHIS. The search range with respect to the initial velocity structure model for the simulated annealing algorithm is still set to be ±80%. Fig. 4.6 shows the fitting of the theoretical microtremor H/V spectral ratios calculated with the identified velocity structures at the damaged sites in the subdistricts. The good consistency between theoretical and observed microtremor H/V spectral ratios suggests that the identified velocity structures are reliable. The identified velocity structures are then used to calculate the transfer functions at the damaged sites in the subdistricts as shown in Fig. 4.7. Appendix B.16 shows the dispersive curves and response functions of surface waves (i.e., Raileigh waves and Love waves) calculated with the identified velocity structures. Finally, we estimate the surface motions from the synthesized bedrock motions at MYG06 during the mainshock by use of the transfer functions at the damaged sites in the subdistricts. The estimated ground motion indices are listed in Table 4.2.

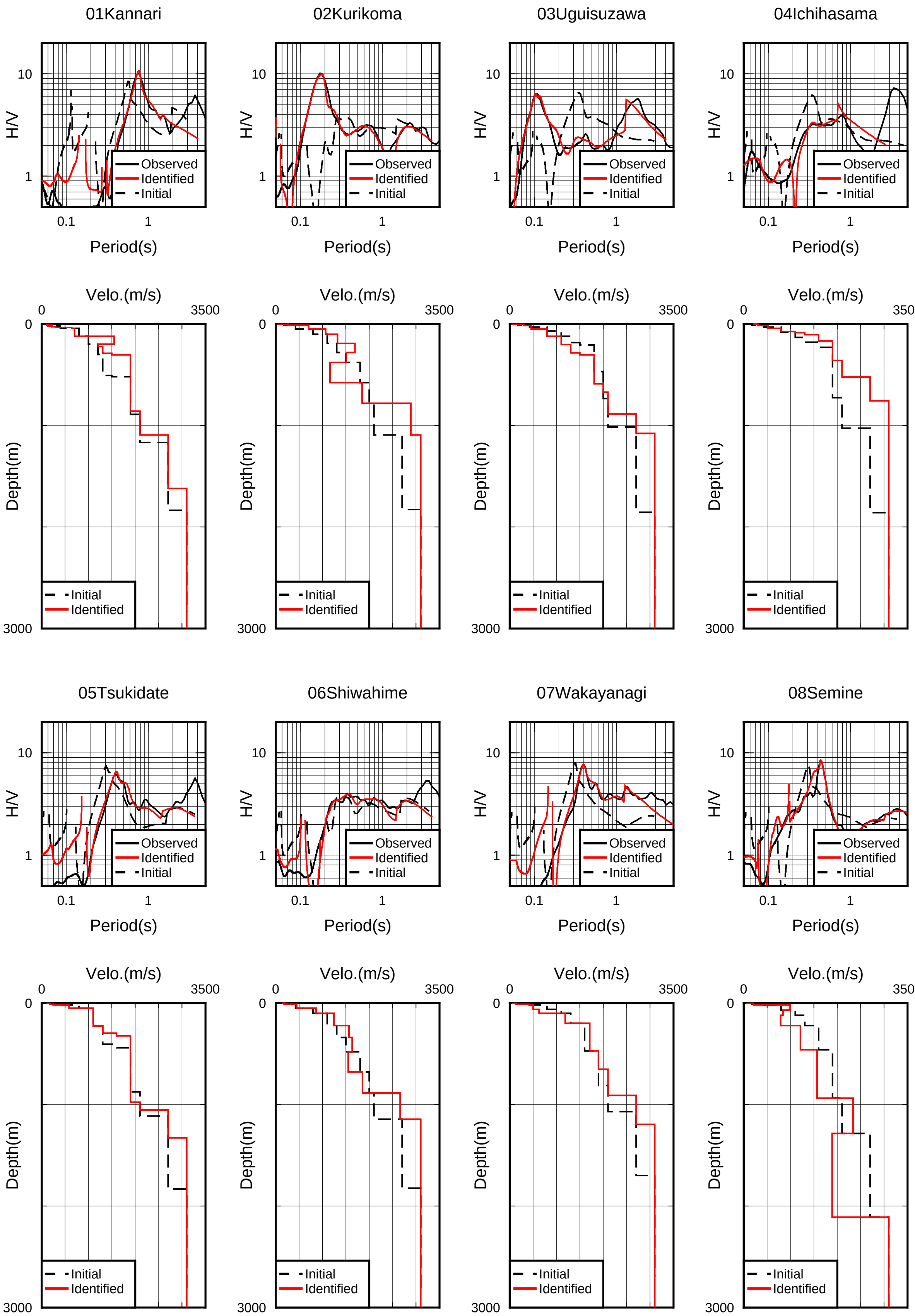
01Kannari
02Kurikoma
03Uguisuzawa
04Ichihasama
05Tsukidate
06Shiwahime
07Wakayanagi
08Semine
H/V
10
1
0.1
1
Period(s)
Observed
Identified
Initial
Velo.(m/s)
0
3500
Depth(m)
0
3000
Initial
Identified

(a)

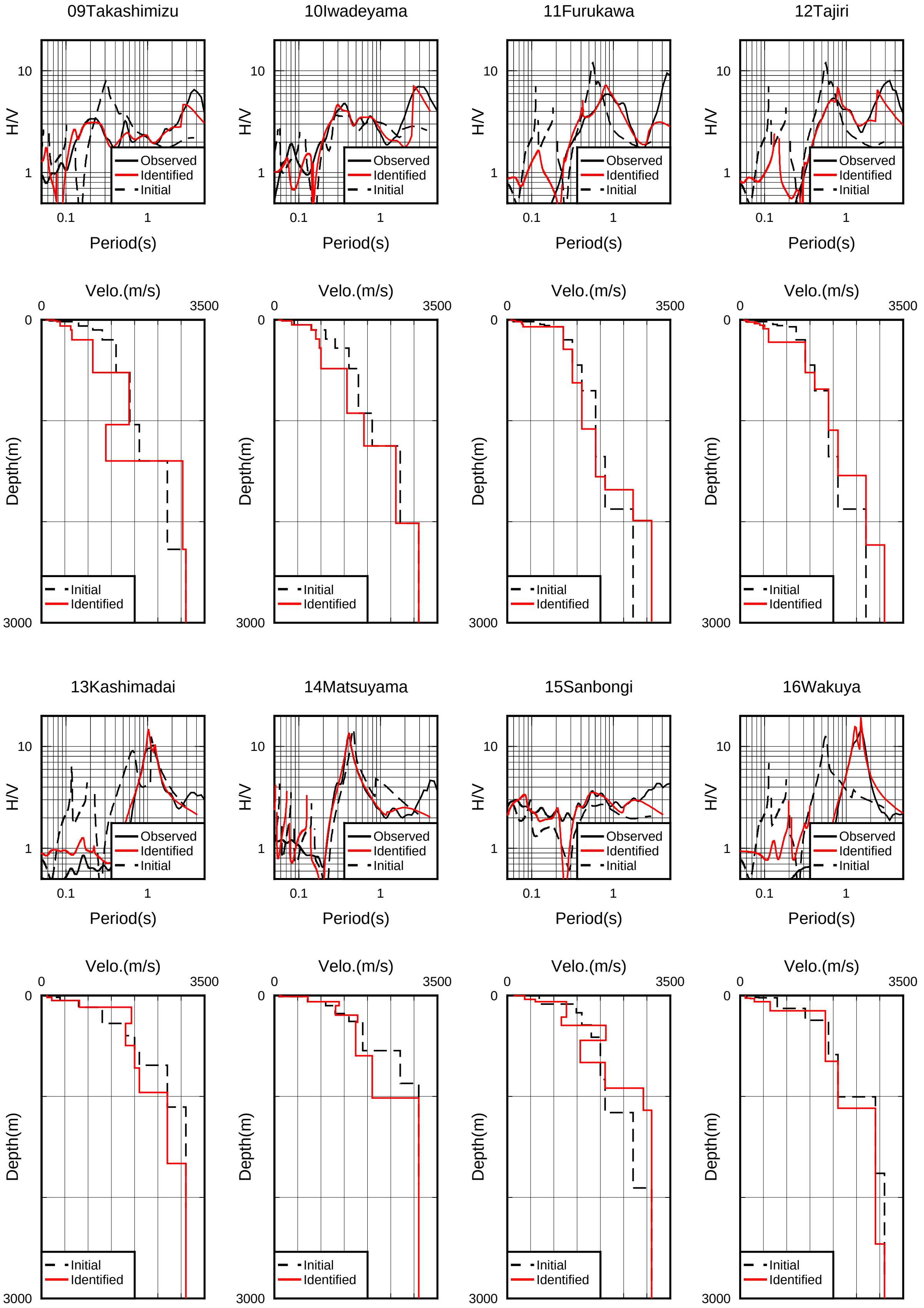

(b)

Fig. 4.6 Fitting of H/V theoretical microtremor spectral ratios and identified velocity structures

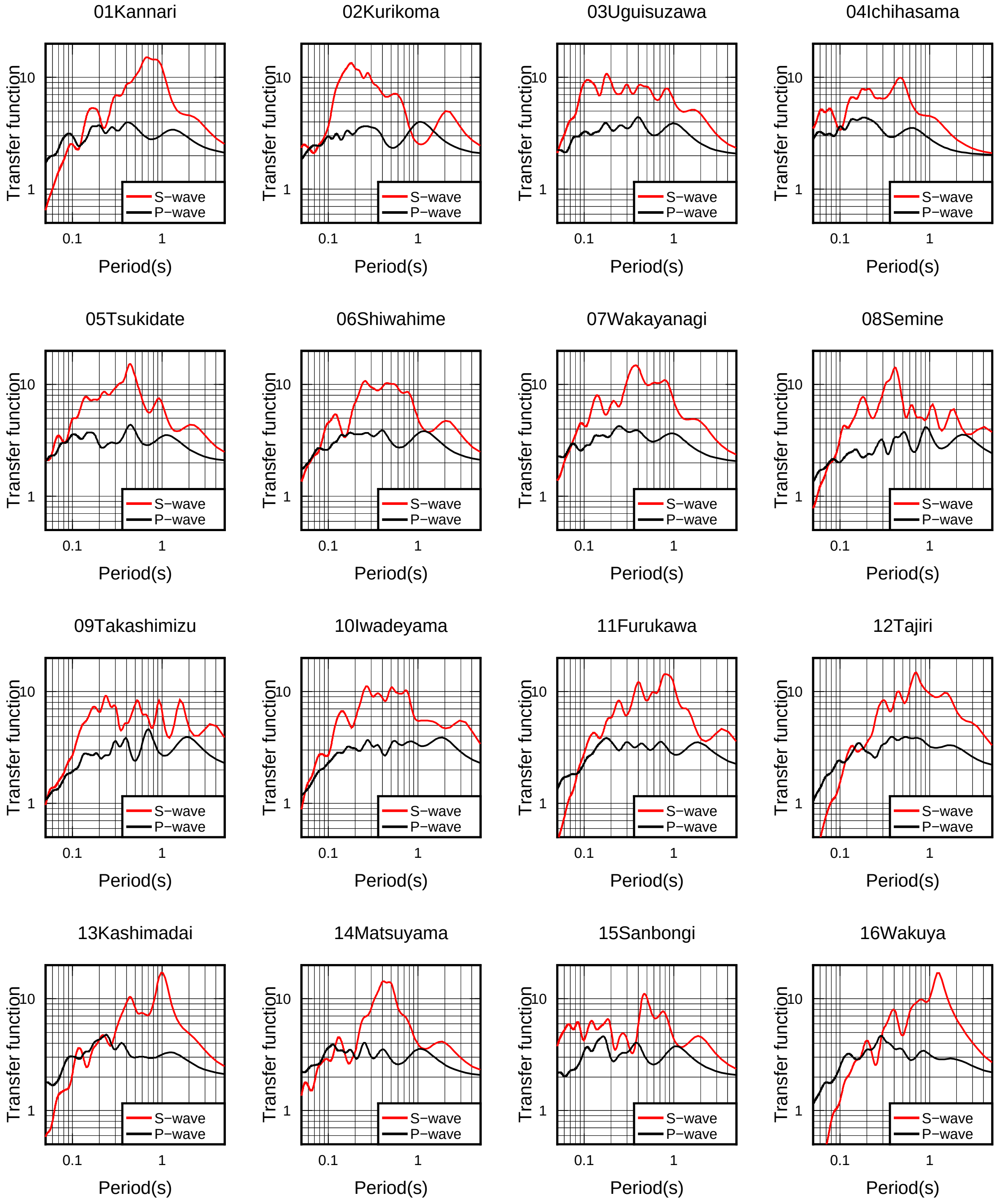

01Kannari

02Kurikoma

03Uguisuzawa

04Ichihasama

05Tsukidate

06Shiwahime

07Wakayanagi

08Semine

09Takashimizu

10Iwadeyama

11Furukawa

12Tajiri

13Kashimadai

14Matsuyama

15Sanbongi

16Wakuya

Fig. 4.7 Transfer functions calculated with the identified velocity structures in the subdistricts ($Q_S = V_S/20$; $Q_P = Q_S/2$)

4.3 Fragility curves based on damage ratios and estimated ground motions in the subdistricts

In order to fragility curves, we not only need the ground motion indices but also the damage data of buildings in each subdistrict which are not published by the FDMA. We obtain these damage data classified into total collapse, partial collapse and partial damage, together with the total number of buildings from the city halls, i.e., Kurihara and Osaki cities, except the Wakuya town in which the total number of buildings are published by STAT. The total number of buildings, in fact, is generally the summation of three kinds of numbers, i.e., the number of exclusive residential buildings, the number of combined residential buildings and the number of farm residential buildings for each subdistrict. The total number of buildings and three damage ratios in each subdistrict as well as the Wakuya town are listed in Table 4.2.

Table 4.2 Estimated ground motion indices and damage ratios in the subdistricts of Osaki and Kurihara cities and Wakuya town

District	Subdistricts	PGA (gal)	PGV (cm/s)	I_{JMA}	SI (cm/s)	TCR (%)	CR (%)	DR (%)	Total[1] number
Kurihara city	Kannari	647.2	80.7	6.2	93.9	0.30	3.23	30.36	2635
	Kurikoma	951.5	53.0	6.0	59.5	0.10	0.86	14.32	3932
	Uguiszawa	771.5	64.0	6.0	67.5	0.00	0.23	8.45	852
	Ichihasama	597.2	47.9	5.8	53.5	0.07	0.38	9.27	2922
	Tsukidate	736.0	68.7	6.0	72.6	0.08	1.17	21.55	3944
	Shiwahime	605.1	61.6	6.0	67.5	0.31	2.09	21.50	2246
	Wakayanagi	705.1	67.3	6.1	77.4	0.60	2.87	22.28	4489
	Semine	671.7	56.8	5.9	69.4	0.15	1.98	24.51	1314
	Takashimizu	709.9	73.2	6.0	84.8	0.50	4.95	58.02	1010
	Naruko[2]	254.3	39.2	5.1	32.6	0.02	0.41	3.84	4377
Osaki city	Iwadeyama	664.8	69.9	6.0	81.3	0.17	1.40	9.74	5923
	Furukawa	644.8	78.0	6.1	95.4	1.14	4.98	21.13	28538
	Tajiri	609.0	93.7	6.2	101.7	1.58	9.70	28.65	5578
	Kashimadai	643.4	92.3	6.2	104.9	1.70	10.28	46.41	4710
	Matsuyama	558.5	57.0	6.0	62.6	1.80	10.09	29.64	2993
	Sanbongi	578.1	57.4	5.9	61.1	1.01	4.91	21.76	2872
Wakuya town		523.1	85.0	6.2	99.6	2.47	15.06	32.73	5830

Based on the ground motion indices and building damage ratios, the fragility curves shown in Fig. 4.8 ∼ Fig. 4.10 in this area are constructed through the geometric mean regression method. Table 4.3 lists all the necessary parameters for plotting fragility curves, together with the determination coefficients. It can be seen that the estimated ground motions are generally related with the damage ratios. The PGAs do not exhibit

---

[1] It means the total number of buildings in each subdistrict

[2] No microtremor measurement was conducted, the ground motion indices are obtained from the record at the strong-motion station (MYG005) in Naruko

much variation in the studied area, while PGVs and SIs obviously vary from site to site. Damage ratios increase quickly as the PGA approaches to 500 gal, PGV 60 cm/s, I_{JMA} 6.0 and SI 60 cm/s. These values can be used as the threshold for damage assessment and aseismic design of buildings.

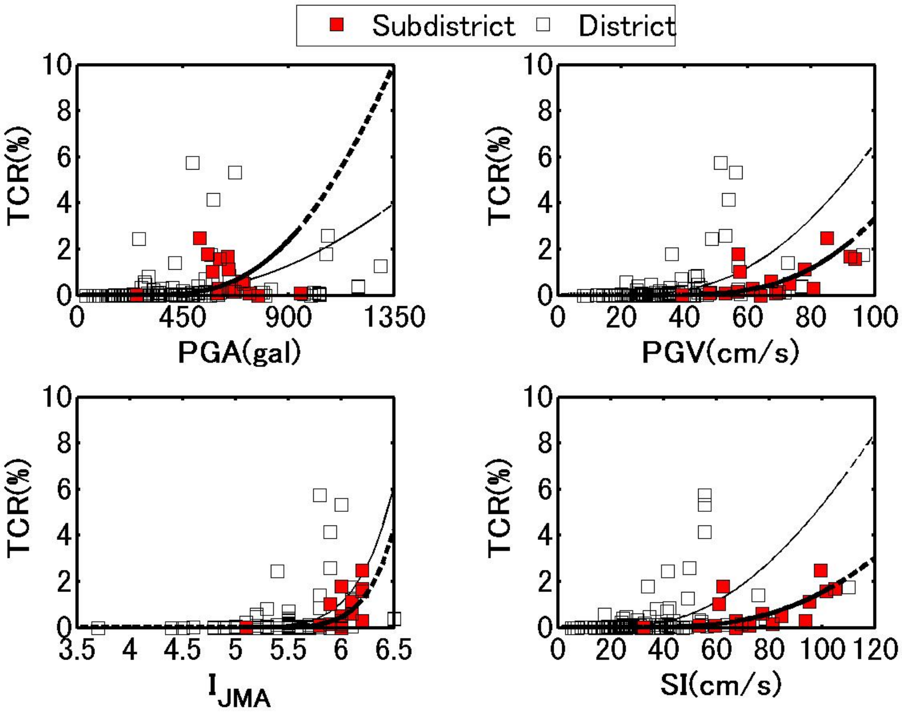

Fig. 4.8 Fragility curves for TCR in the subdistricts (thick curves) of Osaki and Kurihara cities and the Wakuya town, and the stricken districts (thin curves)

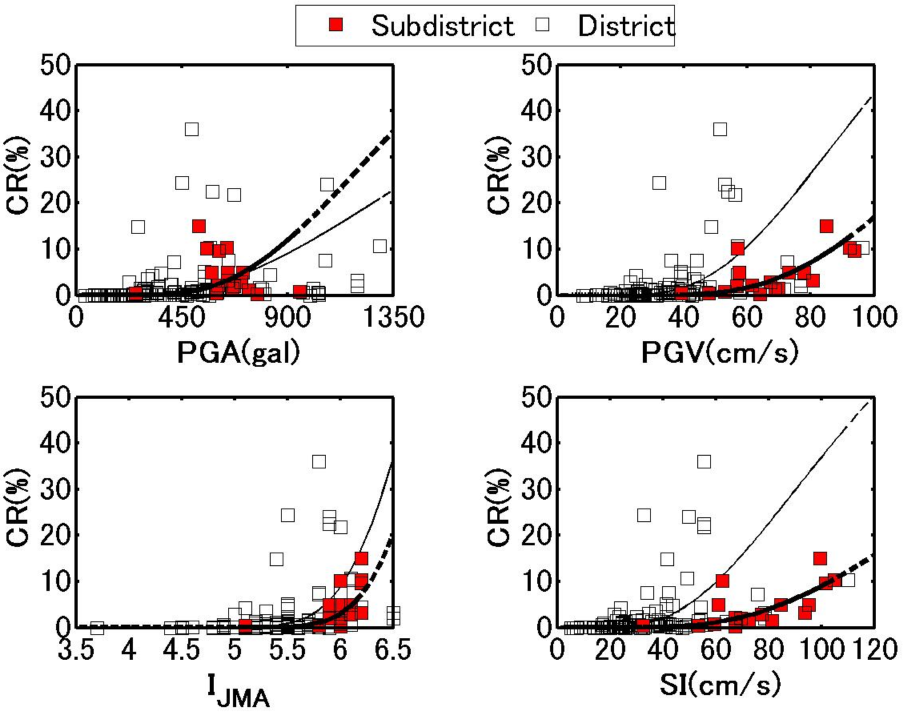

Fig. 4.9 Fragility curves for CR in the subdistricts (thick curves) of Osaki and Kurihara cities and the Wakuya town, and the stricken districts (thin curves)

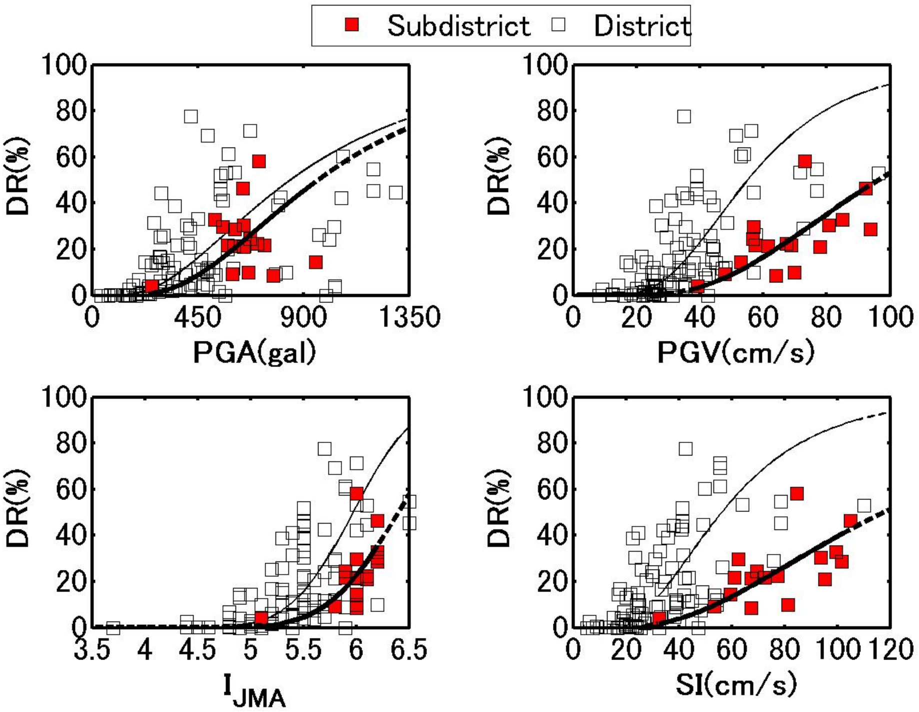

Fig. 4.10 Fragility curves for DR in the subdistricts (thick curves) of Osaki and Kurihara cities and the Wakuya town, and the stricken districts (thin curves)

Table 4.3 Coefficients about fragility curves in subdistricts

	PGA(gal)			PGV(cm/s)			I_{JMA}			SI(cm/s)		
	μ	σ	R^2	μ	σ	R^2	μ	σ	R^2	μ	σ	R^2
TCR	7.947	0.577	0.033	5.548	0.514	0.502	7.469	0.562	0.477	5.993	0.641	0.495
CR	7.393	0.501	0.0001	5.023	0.436	0.462	6.898	0.477	0.332	5.337	0.545	0.446
DR	6.871	0.557	0.116	4.568	0.485	0.469	6.400	0.530	0.428	4.767	0.607	0.509

Compared with the determination of coefficient-R^2 for the fragility curves constructed in districts, chapter 2, the correlation between any of the damage ratios and ground motion indices (PGV, SI and I_{JMA}) gets better, especially the correlation for TCR and ground motion indices is remarkably improved, and the uncertainties for the damage ratios and ground motion indices become smaller. It may be explained by the fact that the number of damage data we used is limited. The other might be that not only the estimated ground motions but also the damage ratios are representative for the studied subdistricts. PGV, SI and I_{JMA} have a better correlation with damage ratios than PGA. Especially, the correlation between PGV and damage ratios is almost identical with that between SI and damage ratios. Again, it is caused by the well consistency between PGV and SI just as shown in Fig. 4.12. The relationship between PGV and SI is also compared with that constructed in chapter 2. We can see SI equals to 1.1282 times PGV, which is closer to 1.18 presented by Tong et al. (1994). The correlation between PGA and damage ratios is not so satisfactory, it can be partly explained from the sensitivity to short period. Just as chapter 2, we again sort the damage data by the predominant period of pseudo-velocity response spectra (pSv) shown in Fig. 4.15. It can be seen that the predominant periods of the pSv in the subdistricts are all longer than 0.5 s. For instance, the PGA in the Kurikoma subdistrict of Kurihara city approaches to 960 gal. But its predominant period of pSv is longer than 5.0 s which almost will not cause damage to buildings. The period characteristics of estimated ground motions is also examined through Fig. 4.13. It can be seen that the equivalent predominant periods of the estimated ground motions are densely distributed from 0.5 s and 1.0 s, and there is no subdistrict with PGV greater than 100 cm/s and PGA greater than 800 gal, which can be used to explain the relatively low damage ratios. In addition, pseudo-velocity response spectra are also investigated as shown in Fig. 4.14. We can see that many of the response spectra have low amplitude smaller than 200 cm/s, some are predominant at a short period, e.g., 0.5 s. The large amplitude around 1.0 s in the Kashimadai, Furukawa, Tajiri, Kannari subdistricts and Wakuya town can account for the large damage ratios well. It also implies that the estimated ground motions are reliable. The pSv in Kashimadai subdistricts has a sharp peak at about 1.0 s, its amplitude is the largest, comparable to that in JR-Takatori

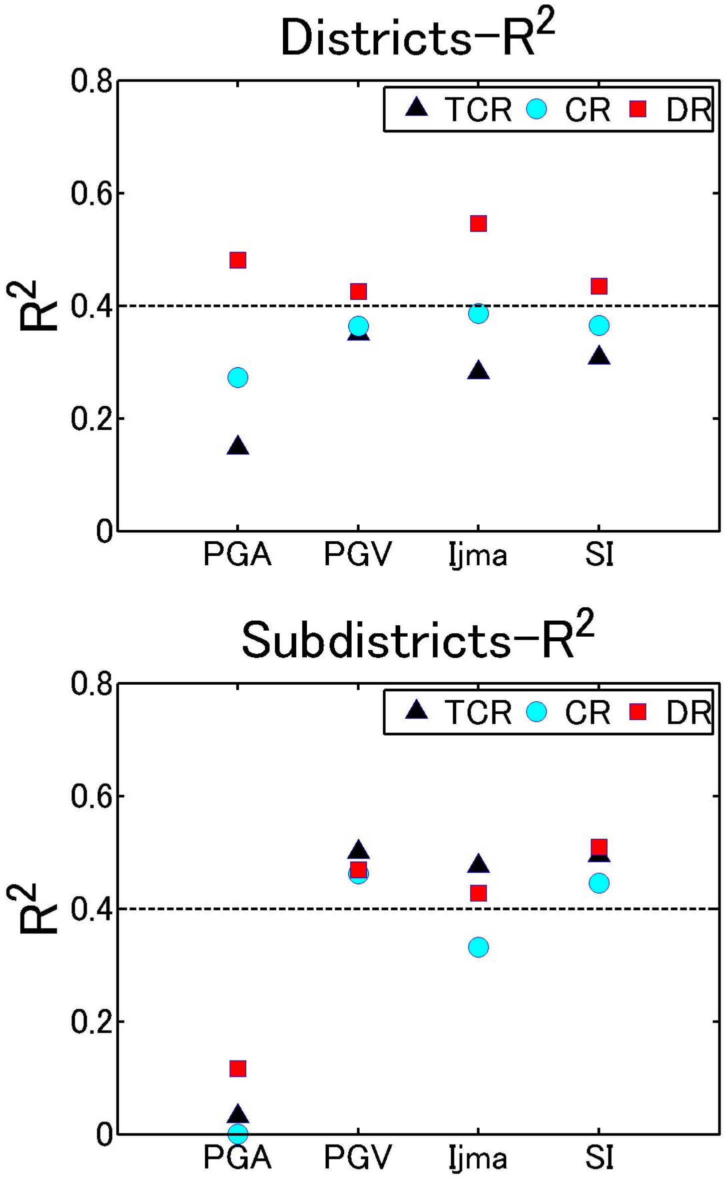

Fig. 4.11 Comparison of R^2 for damage ratios versus ground motion indices in subdistricts with those in districts

during the 1995 Kobe earthquake, but the damage ratio in Kashimadai is not comparable, quite lower than that in JR-Takatori, which suggests that the estimated ground motions may be overestimated due to neglecting the nonlinear effect.

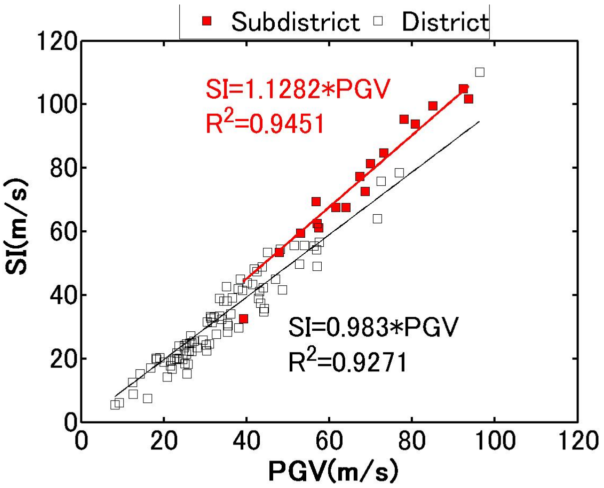

Fig. 4.12 Relationship between SI and PGV based on the estimated ground motions in the subdistricts (red) and districts (black)

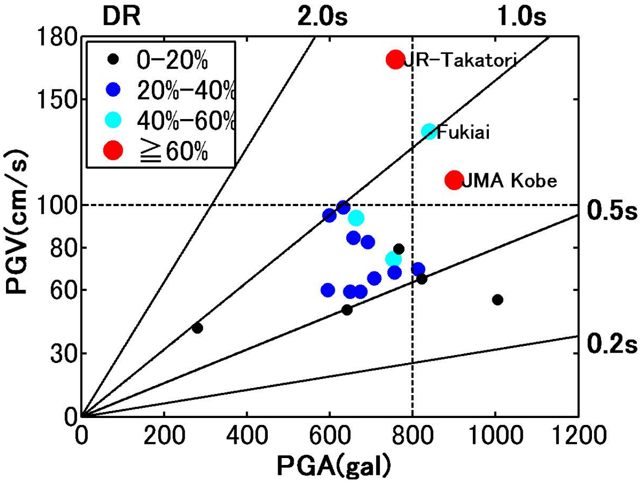

Fig. 4.13 Equivalent predominant period ($T_{eq} = 2\pi PGV/PGA$) of estimated ground motions in the subdistricts. PGA and PGV in this figure denote the maximum for the vector summation in three components. Three heavy damaged sites, JR-Takatori, Fukiai and JMA-Kobe in the 1995 Kobe earthquake are included.

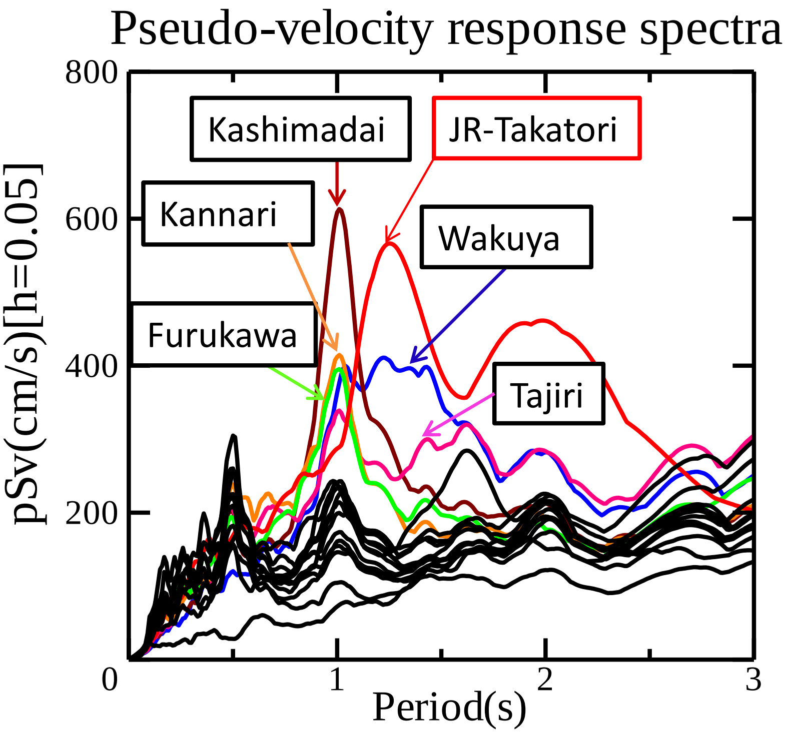

Fig. 4.14 Pseudo-velocity response spectra of estimated ground motions in stricken subdistricts. Red curve is the pseudo-velocity spectrum of the observed ground motions at JR-Takatori in the 1995 Kobe earthquake; others are the pseudo-velocity spectra of estimated ground motions during the mainshock

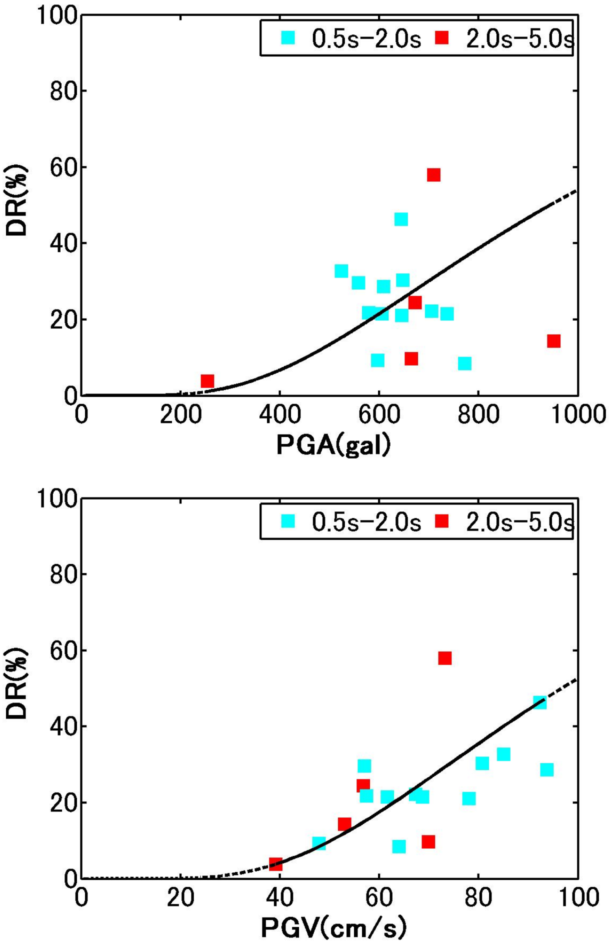

Fig. 4.15 Sensitivity of PGA or PGV to predominant period of pseudo-velocity response spectra for the estimated ground motions during the mainshock

4.4 Summary

Microtremor measurement was performed at the damaged sites in the subdistricts of the Osaki and Kurihara cities, and Wakuya town, near the source fault area of mainshock. The underground velocity structures are identified from the observed microtremor H/V spectral ratios, followed by the calculation of the transfer functions for S- and P-wave in the subdistricts. We then apply the estimation method to estimate the ground motions in the subdistricts during the mainshock by use of the synthesized bedrock motions at MYG006. Finally we construct the fragility curves based on the estimated ground motions and damage ratios in the studied subdistricts and compare them with the ones constructed in chapter 2.

We find that the estimated ground motions correlates with the damage ratios. It may imply that the estimated ground motions are reliable.

PGAs at the damaged sites do not vary significantly in the studied subdistricts, while PGV and SI vary in a wide range.

Compared to chapter 2, I_{JMA}, PGV and SI have a better correlation with damage ratios. Especially the correlation between TCR and ground motion indices gets remarkably improved. It suggest that TCRs are more accurate than those in administrative districts and also estimated ground motions are more representative for subdistricts.

SI has a good correlation with PGV for the estimated ground motions. It may suggest that the fragility curves for SI and PGV is equivalent to each other.

The less correlation for PGA versus damage ratios can be partly explained by the sensitivity of PGA to short predominant period of pseudo-velocity response spectra.

The short equivalent predominant period and low PGV, PGA can be used to account for the relatively small damage ratios, compared with the heavy damaged sites in the 1995 Kobe earthquake.

Damage ratios increase quickly as PGA approaches 500 gal, PGV approaches 60 cm/s, SI approaches 60 cm/s and I_{JMA} approaches to 6.0. These values are expected to be used as the threshold for damage assessment and aseismic design of buildings.

Chapter 5

Conclusions

During the 2011 Tohoku Earthquake, a large amount of buildings in inland of east Tohoku and Kanto regions were damaged due to ground shaking. In order to facilitate damage assessment and disaster mitigation for future disastrous earthquakes, it is necessary to clarify the relationships between the damage ratios and characteristics of ground motion during this earthquake. Three kinds of damage ratios, i.e., TCR, CR, and DR, calculated from the damage data in administrative districts (*shi, cho, mura in Japanese*), are related with four ground motion indices, i.e., PGA, PGV, I_{JMA} and SI. Then one method of estimating ground motions at damaged sites in subdistricts is proposed and verified. After applying the proposed method at damaged sites of subdistricts, the fragility curves based on damage ratios and estimated ground motions in subdistricts in Osaki, Kurihara and surrounding cities are constructed.

1. We found that the transfer function calculated with the identified underground velocity structures from microtremor H/V spectral ratio is almost the same as that calculated with the identified underground velocity structures from earthquake H/V spectral ratio, although the identified underground velocity structures are not always the same as each other. It suggests that the underground velocity structures can be identified from either earthquake or microtremor H/V spectral ratios.

2. We confirmed that the underground velocity structures identified from microtremor H/V spectral ratios can be used to estimate ground motions during small earthquakes.

3. We verified that the ground motions during the mainshock can be estimated by use of short-period source model and the underground velocity structures.

4. The uncertainties for fragility curves constructed based on estimated ground motions and damage ratios in subdistricts are smaller than that constructed based on observed ground motions and damage ratios in districts. The correlation about damage ratios and ground motion indices (except PGA) for fragility curves in subdistricts is improved, especially for TCR, compared with that for fragility curves in districts. It can be explained by the representativeness of both ground motions and TCR for the subdistricts.
5. I_{JMA}, PGV and SI have a better correlation with any damage ratios than PGA. The less correlation for PGA can be attributed to sensitivity of PGA to short predominant period of pseudo-velocity response spectra.
6. The correlation for PGV versus damage ratios is almost the same as that for SI versus damage ratios, it can be attributed to the linear relationship between SI and PGV.
7. The equivalent predominant periods of the observed ground motions in stricken districts are around 0.5 s, while they varies from 0.5 s to 1.0 s for the estimated ground motions in the subdistricts. The short predominant period characteristics can be regarded as one of the reasons for relatively low damage ratios. On the other hand, the short predominant period of pseudo-velocity response spectra and low amplitude of pseudo-velocity response spectra (pSv) over 1.0 s $\sim$ 2.0 s can also account for the relatively low damage ratios compared with that of pSv in the heavy damaged sites during the 1995 Kobe earthquake.
8. Damage ratios increase quickly as PGA approaches 500 gal, PGV approaches 60 cm/s, SI approaches 60 cm/s and I_{JMA} approaches to 6.0. These values are expected to be used as the threshold for damage assessment and aseismic design of buildings.

At last, we anticipate the fragility curves can be improved further by collecting the damage data classified by construction age, structural type and so on. Uncertainty of ground motions in each subdistrict should also be discussed. The estimation of ground motions involving the nonlinear effect are expected to be applied at the sites with soft layers near the surface during the mainshock afterwards.

Appendix A

Damage data and ground motion indices in stricken districts

Table A.1 Damage data and ground motion indices in stricken districts

District[1]	PGA (gal)	PGV (cm/s)	I_{JMA}	SI (cm/s)	Total[2] Number	TCR (%)	CR (%)	DR (%)
Kitakami-shi	493.4	35.3	5.7	38.2	27,400	0.113	1.675	4.620
Ichinoseki-shi	783.8	34.0	5.7	32.4	39,010	0.136	1.615	9.228
Oshu-shi	342.0	26.5	5.2	27.1	40,040	0.095	0.367	1.928
Shiroishi-shi	364.6	40.1	5.5	43.9	12,630	0.309	4.703	21.639
Kakuda-shi	349.3	48.1	5.8	54.4	9,680	0.134	1.767	12.056
Tome-shi	650.9	44.0	5.8	42.4	23,740	0.834	7.624	21.491
Osaki-shi	417.4	72.5	5.8	75.9	41,200	1.417	7.184	28.876
Taiwa-cho	548.0	39.0	5.5	41.5	5,820	0.704	5.206	51.753
Kami-machi	487.7	36.5	5.4	39.1	7,380	0.108	0.583	10.732
Fukushima-shi	326.6	24.9	5.1	24.2	85,410	0.215	4.215	9.994
Aizuwakamatsu-shi	450.8	41.5	5.8	43.4	39,270	0.010	0.155	11.446
Koriyama-shi	1069.3	52.8	5.9	49.7	88,490	2.600	23.995	60.377
Shirakawa-shi	1295.1	57.0	6.1	49.1	18,510	1.275	10.627	44.603
Sukagawa-shi	672.5	56.3	6.0	55.5	20,960	5.315	21.861	71.302
Nihonmatsu-shi	403.5	28.0	5.5	23.5	17,060	0.059	2.298	30.539
Tamura-shi	1011.8	38.1	5.7	29.7	12,250	0.114	1.437	24.212
Date-shi	556.9	31.0	5.4	24.7	20,150	0.124	1.191	41.226
Kawamata-machi	288.7	21.6	5.2	17.8	4,920	0.569	1.016	16.911
Inawashiro-machi	275.6	45.1	5.5	53.5	5,350	0.336	1.514	13.963

Continued on next page...

Table A.1 – Continued

District	PGA (gal)	PGV (cm/s)	I_{JMA}	SI (cm/s)	Total Number	TCR (%)	CR (%)	DR (%)
Nishigo-mura	1062.4	36.1	6.0	34.1	5,120	1.797	7.617	42.109
Yabuki-machi	492.3	51.5	5.8	55.7	5,000	5.760	36.060	69.380
Tanagura-machi	275.2	16.8	4.9	17.0	4,270	0.023	0.585	14.496
Miharu-machi	577.6	44.2	6.0	34.7	6,200	0.484	2.952	19.855
Tsuchiura-shi	496.2	33.4	5.6	38.9	42,490	0.014	0.614	12.026
Koga-shi	199.7	21.7	4.8	19.3	43,740	0.018	0.055	6.802
Ishioka-shi	302.4	37.9	5.5	42.0	24,630	0.085	0.666	14.076
Shimotsuma-shi	408.3	35.5	5.5	30.3	13,230	0.333	2.404	22.562
Kasama-shi	967.4	57.6	6.1	56.6	26,190	0.065	0.588	26.197
Toride-shi	516.7	25.5	5.5	24.7	29,670	0.084	1.041	12.093
Tsukuba-shi	342.9	41.8	5.6	48.2	46,070	0.017	0.571	7.526
Hitachiomiya-shi	1031.9	35.4	5.8	31.1	15,100	0.073	0.609	29.649
Chikusei-shi	290.3	33.5	5.3	33.4	33,320	0.015	0.471	16.579
Bando-shi	321.1	30.2	5.3	24.4	15,870	0.025	0.158	15.104
Inashiki-shi	304.2	43.4	5.3	37.5	15,850	0.826	3.502	25.823
Utsunomiya-shi	254.3	18.1	4.9	20.1	138,720	0.006	0.180	12.918
Moka-shi	422.2	35.1	5.7	42.6	18,500	0.065	0.697	77.654
Ohtawara-shi	600.3	47.0	5.7	45.1	21,700	0.028	0.562	11.756
Yaita-shi	290.4	29.5	5.2	25.9	10,780	0.473	1.308	25.325
Nasushiobara-shi	411.6	38.5	5.5	45.0	38,530	0.031	0.127	2.938
Haga-machi	1196.7	76.9	6.5	78.5	4,590	0.349	3.159	54.532
Nakagawa-machi	608.5	71.6	6.0	64.1	6,080	0.115	1.217	53.224
Ichikawa-shi	201.7	25.5	5.0	21.4	87,900	0.010	0.052	0.594
Matsudo-shi	284.0	22.6	5.0	19.7	101,520	0.008	0.138	1.647
Narita-shi	243.1	23.7	5.1	20.1	27,500	0.015	0.240	3.858
Sakura-shi*	1036.2	35.4	5.5	28.4	50,220	0.064	0.392	3.204
Togane-shi	214.7	24.9	5.1	23.5	20,250	0.020	0.094	0.775
Morioka-shi	248.7	12.6	4.8	8.9	76,660	0.001	0.013	0.678
Tono-shi	438.4	30.4	5.4	22.5	9,990	0.000	0.040	5.295
Ninohe-shi	161.4	12.5	4.6	12.6	10,820	0.028	0.028	0.102
Shizukuishi-cho	154.8	19.0	4.8	20.3	5,520	0.000	0.000	0.036
Kanegasaki-cho	188.0	27.2	4.9	25.5	4,290	0.000	0.000	0.000

Continued on next page. . .

Table A.1 – Continued

District	PGA (gal)	PGV (cm/s)	I_{JMA}	SI (cm/s)	Total Number	TCR (%)	CR (%)	DR (%)
Yamatsuri-machi	227.0	23.2	5.0	21.8	2,078	0.000	2.936	14.244
Hirata-mura	417.8	32.7	5.6	27.7	1,992	0.050	0.602	20.733
Furudono-machi	353.4	26.1	5.3	22.5	1806	0.000	1.550	38.649
Ono-shi	793.2	44.3	5.5	35.8	3,502	0.114	1.314	39.235
Kawauchi-mura	451.5	32.2	5.5	33.0	976	0.205	24.385	33.094
Katsurao-mura	525.4	42.8	5.9	38.9	469	0.000	0.213	8.955
Iitate-mura	568.4	22.0	5.4	16.8	1,709	0.000	0.000	0.000
Daigo-machi	399.6	31.6	5.6	31.4	7,750	0.013	0.026	9.006
Kanuma-shi	310.7	25.1	5.2	18.4	31,800	0.000	0.028	4.044
Oyama-shi	419.6	31.3	5.4	33.3	46,830	0.000	0.002	4.544
Motegi-machi	801.9	43.1	5.7	41.2	4,740	0.000	0.253	42.595
Nikko-shi	539.1	24.6	5.2	19.7	31,720	0.000	0.022	1.718
Shiroi-shi	472.7	30.5	5.6	31.6	11,350	0.000	0.000	3.718
Noda-shi	374.1	26.2	5.3	24.9	48,260	0.002	0.015	3.657
Ichihara-shi	129.6	26.8	4.8	22.3	78,280	0.000	0.001	0.089
Mobara-shi	80.3	23.2	4.5	20.0	32,060	0.000	0.003	0.131
Minamiaizu-machi	70.4	8.2	3.7	5.4	6,770	0.000	0.000	0.000
Aizumisato-machi	177.2	14.3	4.8	15.2	6,980	0.000	0.029	4.198
Joso-shi	295.4	34.5	5.5	38.1	18,060	0.000	0.349	44.103
Sakuragawa-shi	827.0	56.9	6.2	54.3	13,270	0.264	4.484	9.955
Kasumigaura-shi	472.2	26.7	5.3	25.0	12,900	0.054	0.202	9.814
Katsuura-shi	39.9	16.1	3.7	7.5	9,510	0.000	0.000	0.000
Kisarazu-shi	142.4	31.4	5.1	32.7	41,210	0.000	0.000	0.000
Futtsu-shi	93.9	20.8	4.4	14.2	17,320	0.000	0.000	0.046
Isumi-shi	98.3	23.6	4.8	24.0	16,860	0.000	0.006	0.231
Kimitsu-shi	108.5	25.6	4.5	15.2	26,370	0.000	0.000	0.034
Sakura-shi	466.2	43.8	5.5	48.9	12,520	0.016	0.224	15.375
Shiwa-cho	239.3	18.2	5.1	19.7	9,920	0.000	0.000	0.806
Wakuya-cho	263.4	48.7	5.4	41.6	5,830	2.453	14.923	31.509
Misato-machi	571.5	96.4	6.1	110.2	7,330	1.760	10.259	52.988
Shikama-cho	487.7	36.5	5.4	39.1	1,981	0.000	0.707	11.307
Ohira-mura	548.0	39.0	5.5	41.5	1,700	0.000	1.000	45.941

Continued on next page. . .

Table A.1 – Continued

District	PGA (gal)	PGV (cm/s)	I_{JMA}	SI (cm/s)	Total Number	TCR (%)	CR (%)	DR (%)
Tomiya-machi	548.0	39.0	5.5	41.5	12,990	0.123	4.149	44.065
Kagamiishi-machi	582.4	53.9	5.9	55.6	4,143	4.152	22.399	61.332
Ichikai-machi	1196.7	76.9	6.5	78.5	4,105	0.390	2.071	45.457
Iwafune-machi	158.8	9.2	4.4	6.2	5,760	0.000	0.000	2.639
Kamagaya-shi	244.4	25.9	4.9	18.2	28,020	0.000	0.032	4.083
Sodegaura-shi	129.6	26.8	4.8	22.3	17,690	0.000	0.006	0.085
Shioya-machi	290.4	29.5	5.2	25.9	4,036	0.000	0.000	5.971
Tomisato-shi	241.7	20.1	5.0	19.0	20,854	0.053	0.086	2.829
Abiko-shi	516.7	25.5	5.5	24.7	32,960	0.407	0.707	8.917
Shisui-machi	1036.2	35.4	5.5	28.4	5,970	0.017	0.034	4.087
Hiraizumi-cho	997.8	42.5	5.9	47.4	2609	0.000	0.000	0.000

---

[1] The administrative unit *shi in Japanese* is approximately equivalent to a city, *cho and machi in Japanese* is approximately equivalent to a town, and *mura in Japanese* village

[2] Generally, it denotes the total number of buildings in a district, but in some small districts, we use the numbers of households instead as the total number of buildings are not available

Appendix B

The dispersive curves and response functions of surface waves at the damaged sites of the subdistricts in Osaki and Kurihara cities, as well as Wakuya town

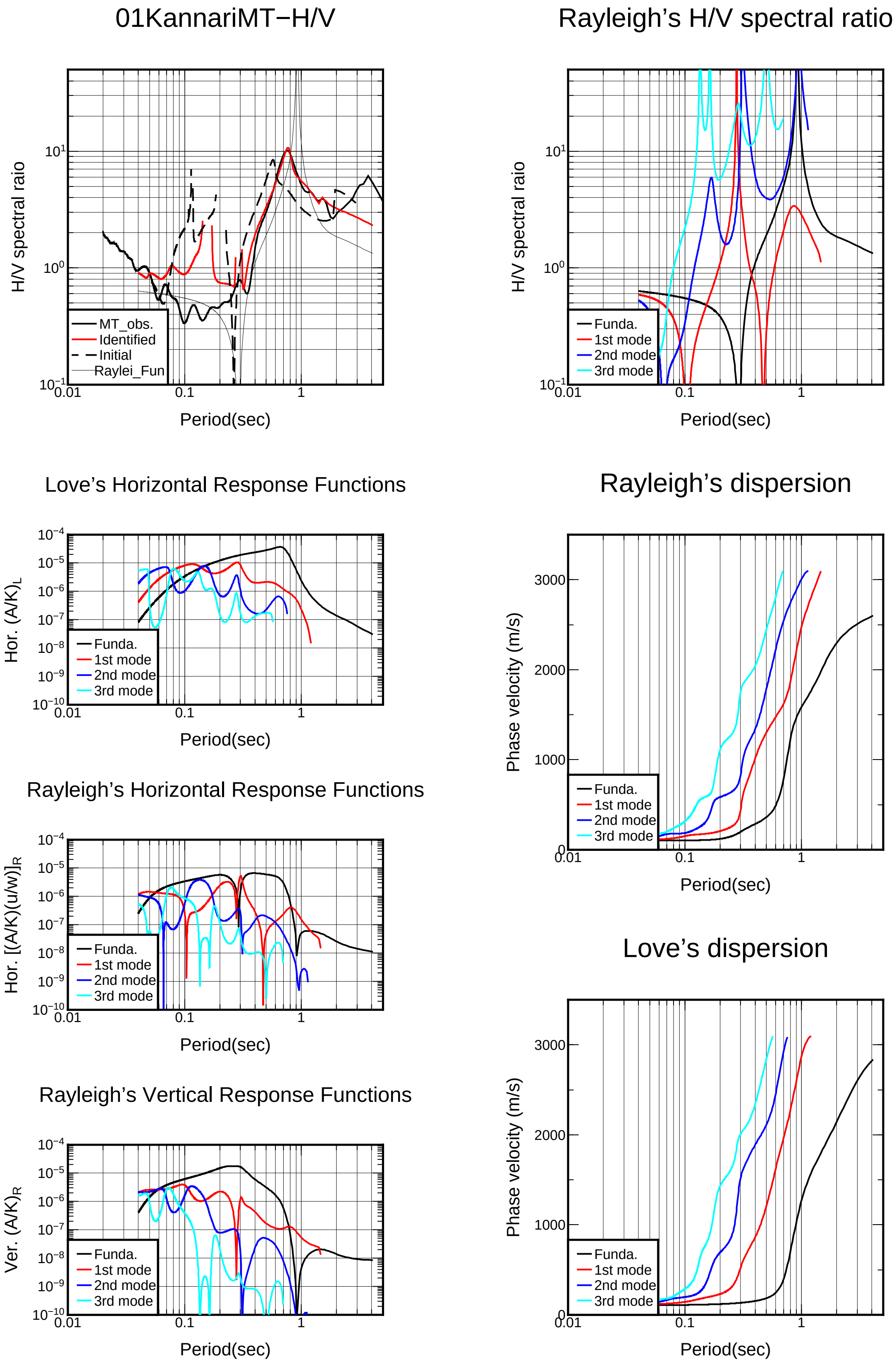

(a) Kannari

Fig. B.1 The dispersive curves and response functions of surface waves

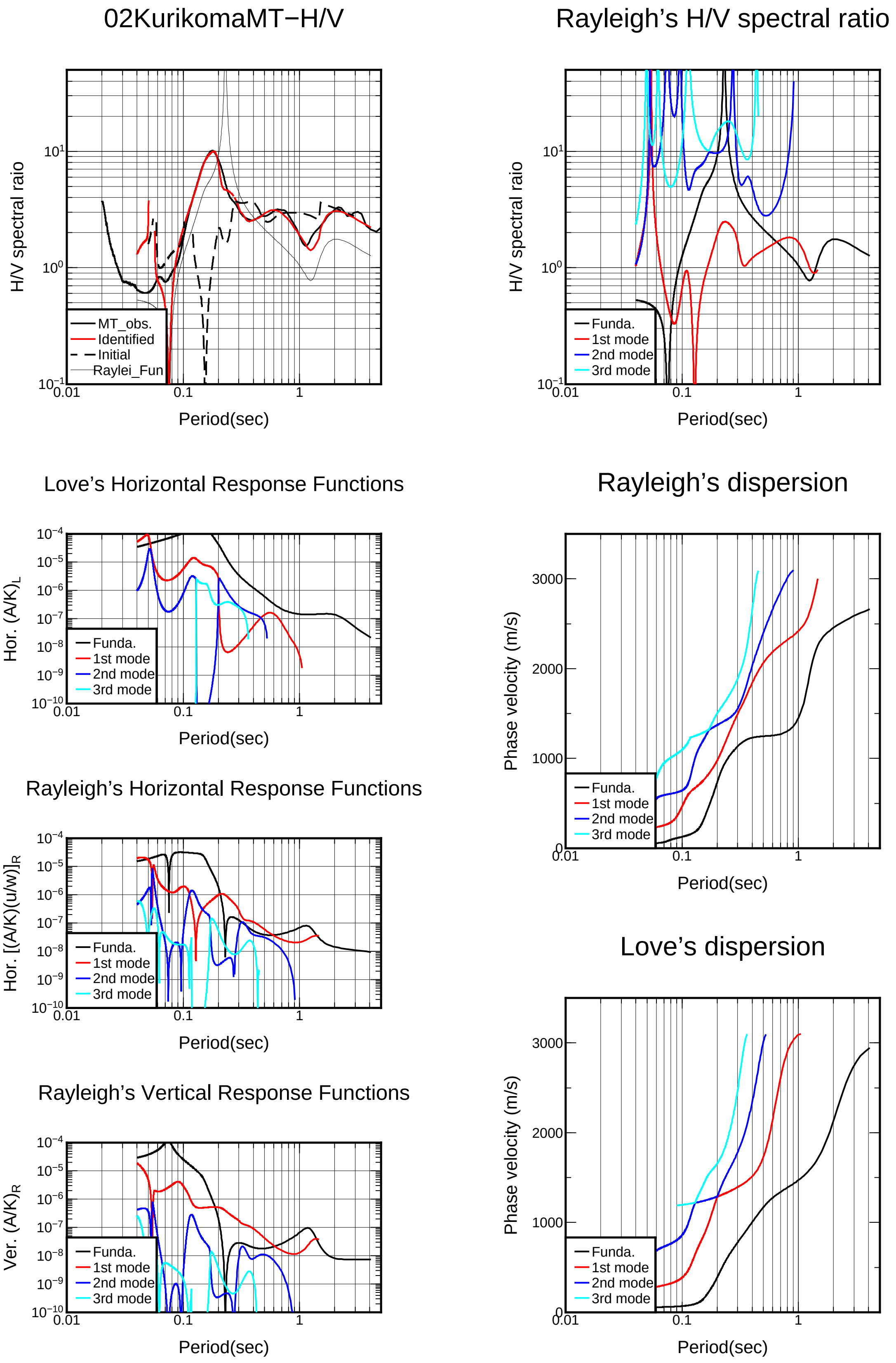
02KurikomaMT−H/V
H/V spectral raio
10^{1}
10^{0}
10^{-1}
0.01
0.1
1
Period(sec)
MT_obs.
Identified
Initial
Raylei_Fun
Rayleigh's H/V spectral ratio
Funda.
1st mode
2nd mode
3rd mode
Love's Horizontal Response Functions
Hor. $(A/K)_L$
10^{-4}
10^{-5}
10^{-6}
10^{-7}
10^{-8}
10^{-9}
10^{-10}
Rayleigh's dispersion
Phase velocity (m/s)
3000
2000
1000
0
Rayleigh's Horizontal Response Functions
Hor. $[(A/K)(u/w)]_R$
Love's dispersion
Rayleigh's Vertical Response Functions
Ver. $(A/K)_R$

(a) Kurikoma

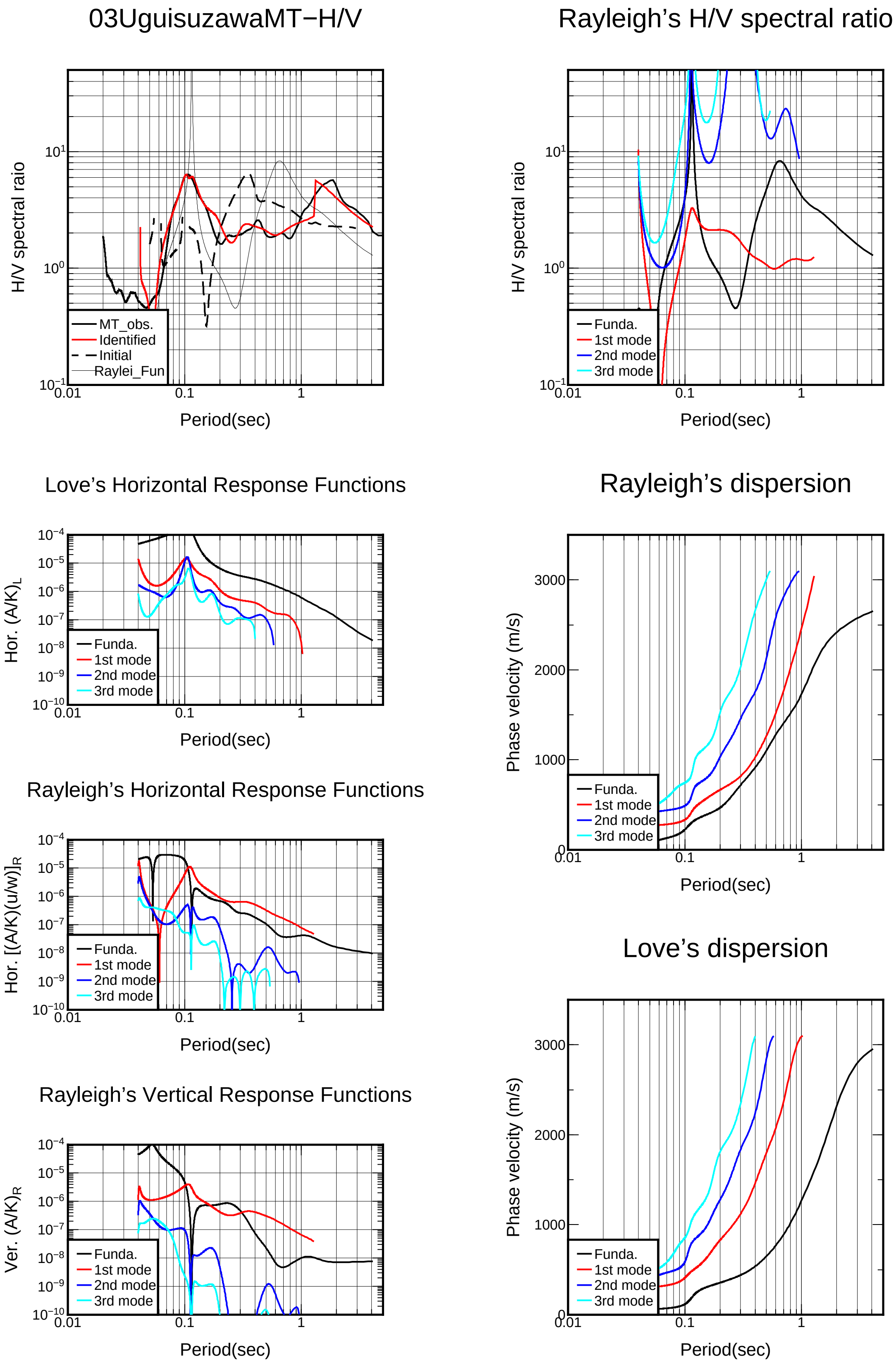

(b) Uguisuzawa

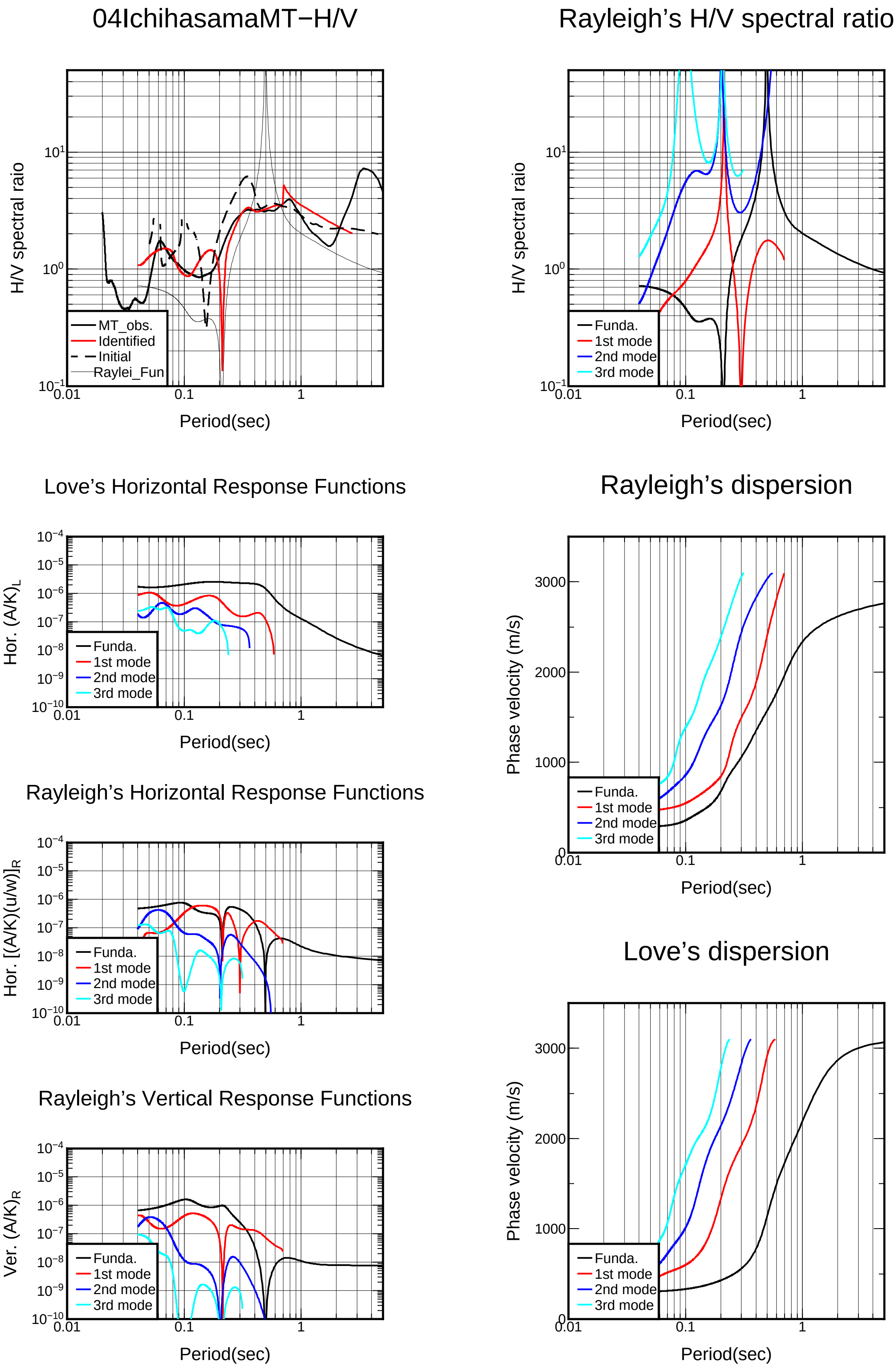

(c) Ichihasama

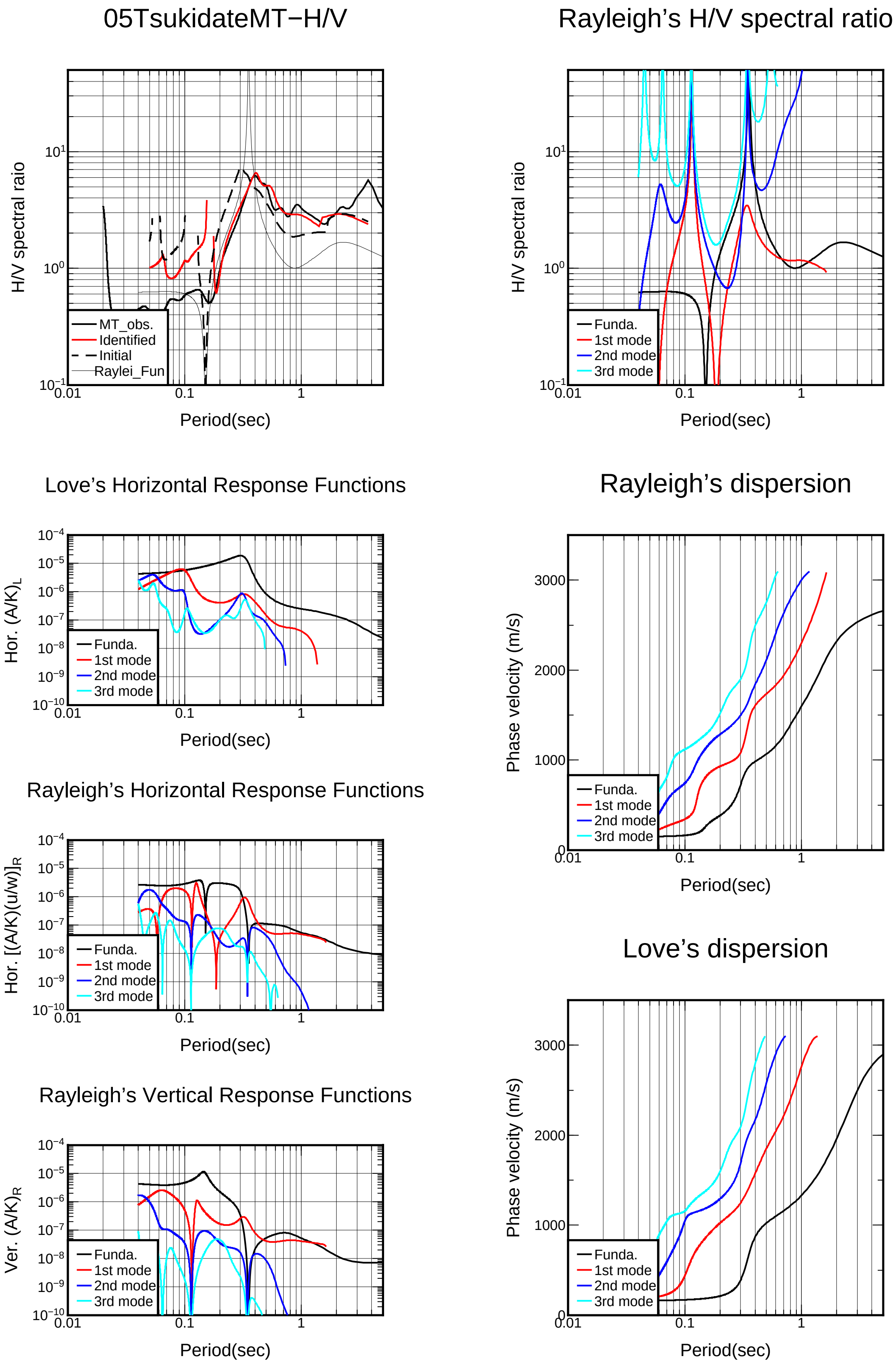
05TsukidateMT−H/V
H/V spectral raio
10^1
10^0
10^{-1}
0.01
0.1
1
Period(sec)
MT_obs.
Identified
Initial
Raylei_Fun
Rayleigh's H/V spectral ratio
H/V spectral raio
Funda.
1st mode
2nd mode
3rd mode
Period(sec)
Love's Horizontal Response Functions
Hor. $(A/K)_L$
10^{-4}
10^{-5}
10^{-6}
10^{-7}
10^{-8}
10^{-9}
10^{-10}
Funda.
1st mode
2nd mode
3rd mode
Period(sec)
Rayleigh's Horizontal Response Functions
Hor. $[(A/K)(u/w)]_R$
Funda.
1st mode
2nd mode
3rd mode
Period(sec)
Rayleigh's Vertical Response Functions
Ver. $(A/K)_R$
Funda.
1st mode
2nd mode
3rd mode
Period(sec)
Rayleigh's dispersion
Phase velocity (m/s)
3000
2000
1000
0
Funda.
1st mode
2nd mode
3rd mode
Period(sec)
Love's dispersion
Phase velocity (m/s)
Funda.
1st mode
2nd mode
3rd mode
Period(sec)

(d) Tsukidate

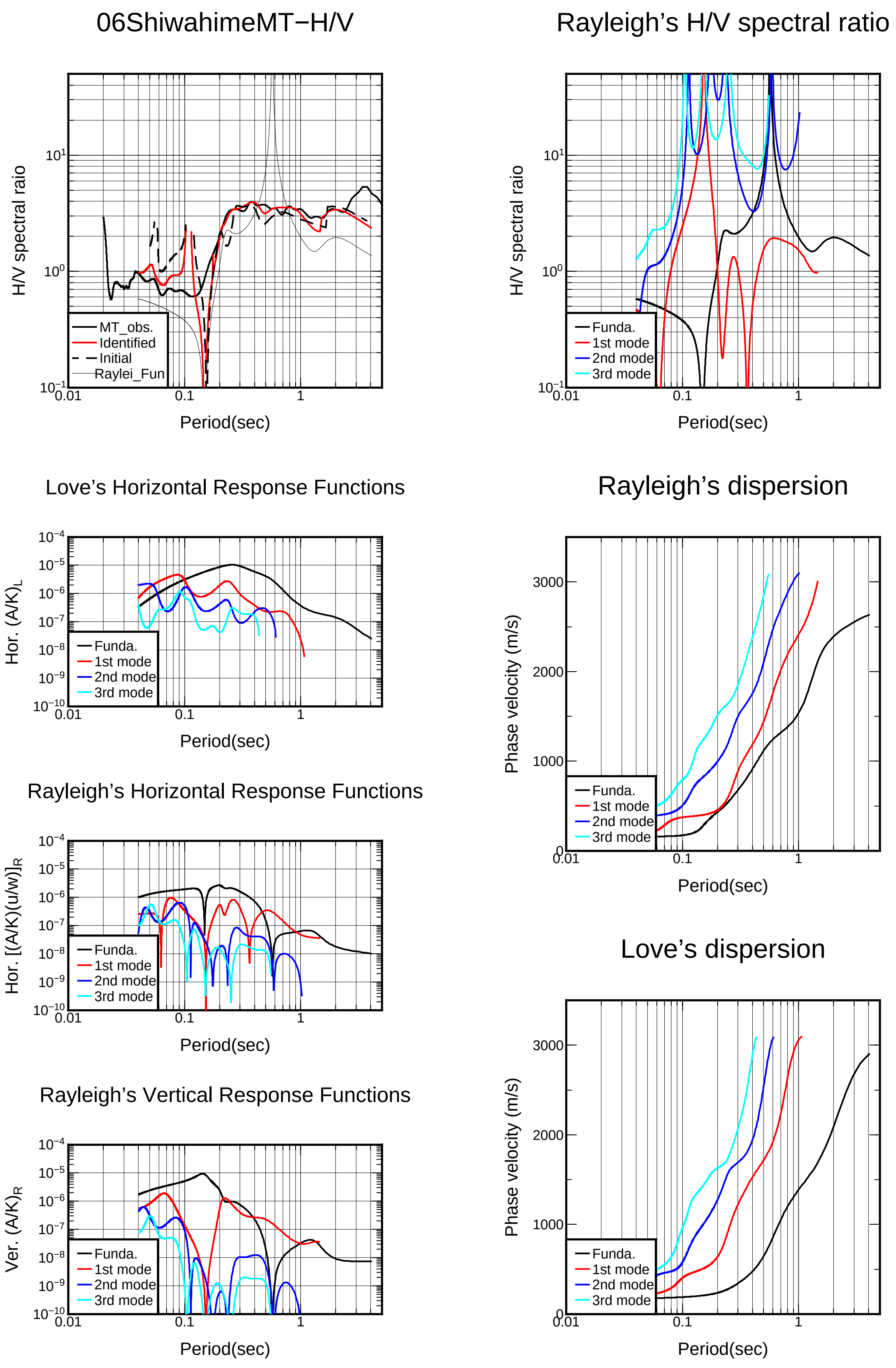
06ShiwahimeMT−H/V
H/V spectral raio
10^{1}
10^{0}
10^{-1}
0.01
0.1
1
Period(sec)
MT_obs.
Identified
Initial
Raylei_Fun
Rayleigh's H/V spectral ratio
H/V spectral raio
Funda.
1st mode
2nd mode
3rd mode
Love's Horizontal Response Functions
Hor. $(A/K)_L$
10^{-4}
10^{-5}
10^{-6}
10^{-7}
10^{-8}
10^{-9}
10^{-10}
Rayleigh's dispersion
Phase velocity (m/s)
3000
2000
1000
0
Rayleigh's Horizontal Response Functions
Hor. $[(A/K)(u/w)]_R$
Love's dispersion
Rayleigh's Vertical Response Functions
Ver. $(A/K)_R$

(e) Shiwahime

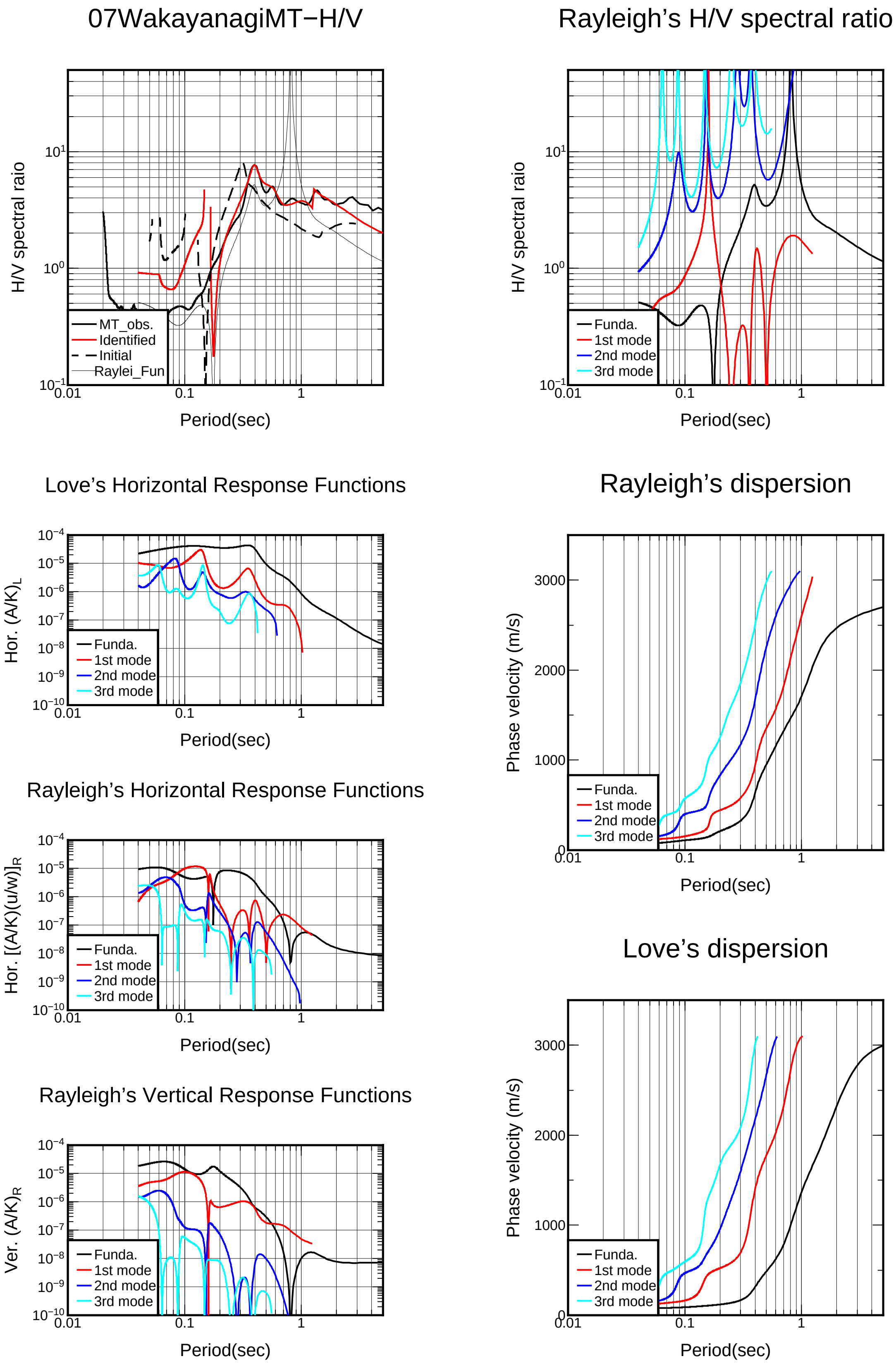

(f) Wakayanagi

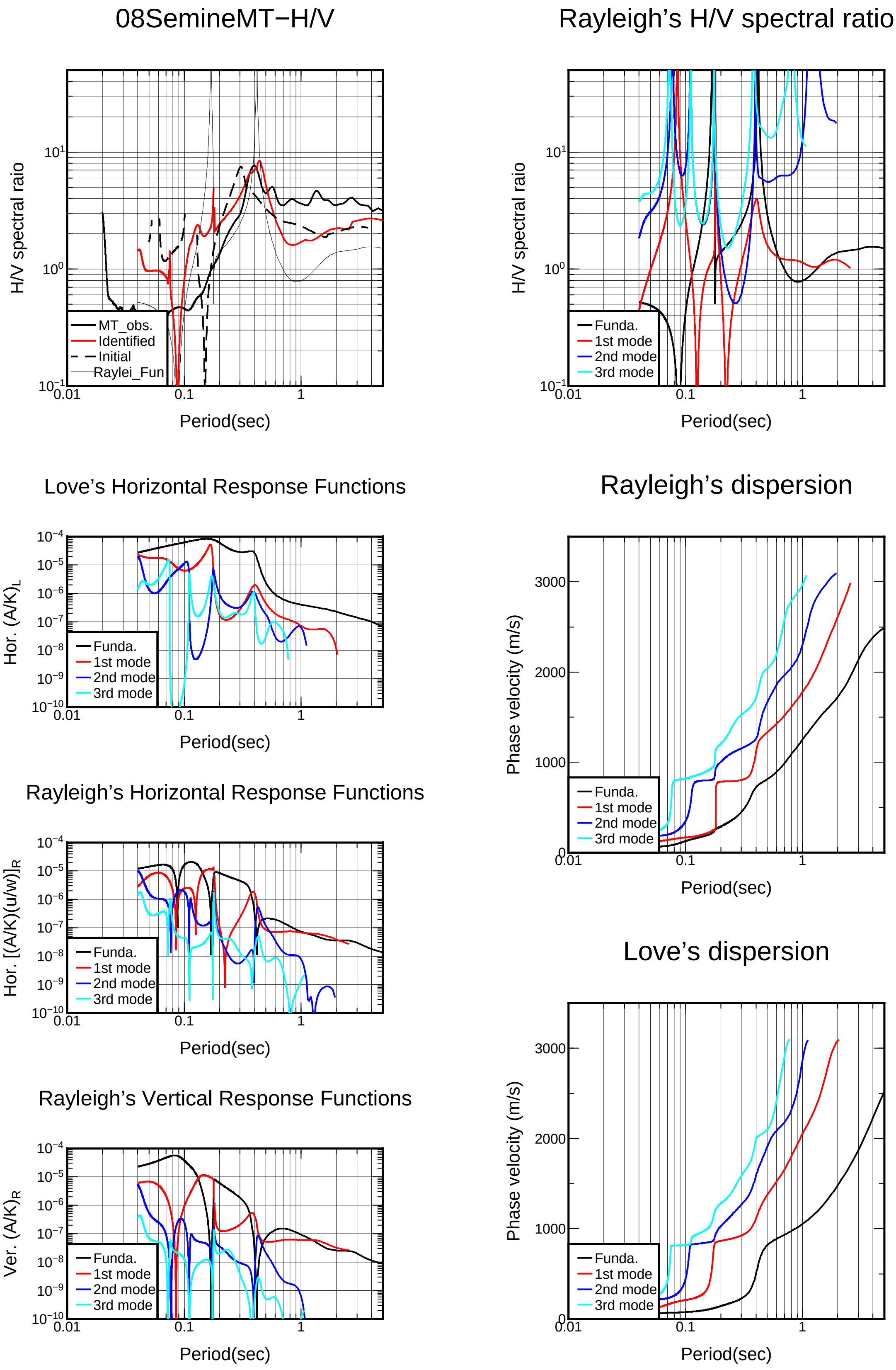
08SemineMT−H/V
H/V spectral raio
10^1
10^0
10^{-1}
0.01
0.1
1
Period(sec)
MT_obs.
Identified
Initial
Raylei_Fun
Rayleigh's H/V spectral ratio
H/V spectral raio
Funda.
1st mode
2nd mode
3rd mode
Love's Horizontal Response Functions
Hor. $(A/K)_L$
10^{-4}
10^{-5}
10^{-6}
10^{-7}
10^{-8}
10^{-9}
10^{-10}
Rayleigh's dispersion
Phase velocity (m/s)
3000
2000
1000
0
Rayleigh's Horizontal Response Functions
Hor. $[(A/K)(u/w)]_R$
Love's dispersion
Rayleigh's Vertical Response Functions
Ver. $(A/K)_R$

(g) Semine

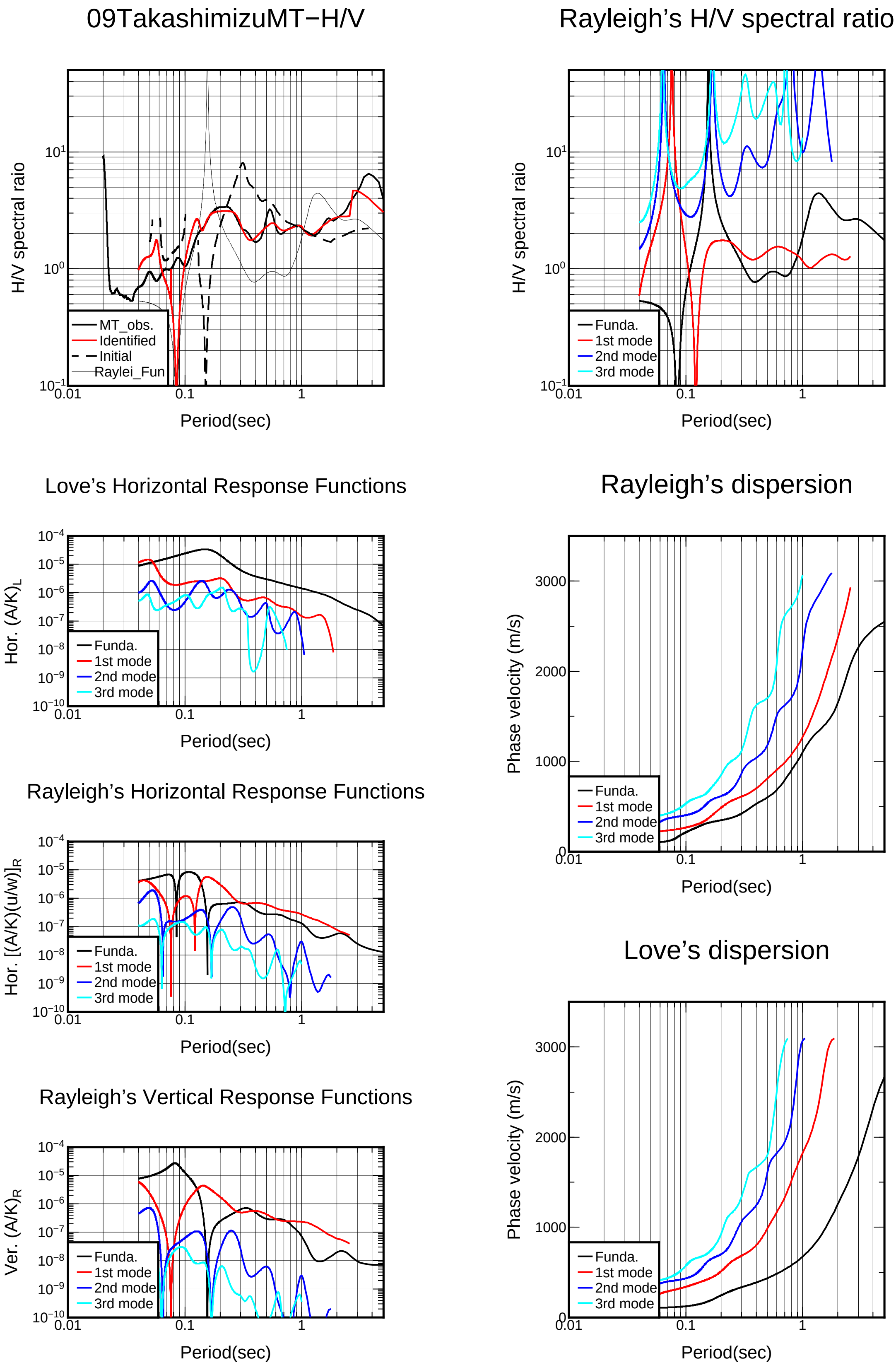

(h) Takashimizu

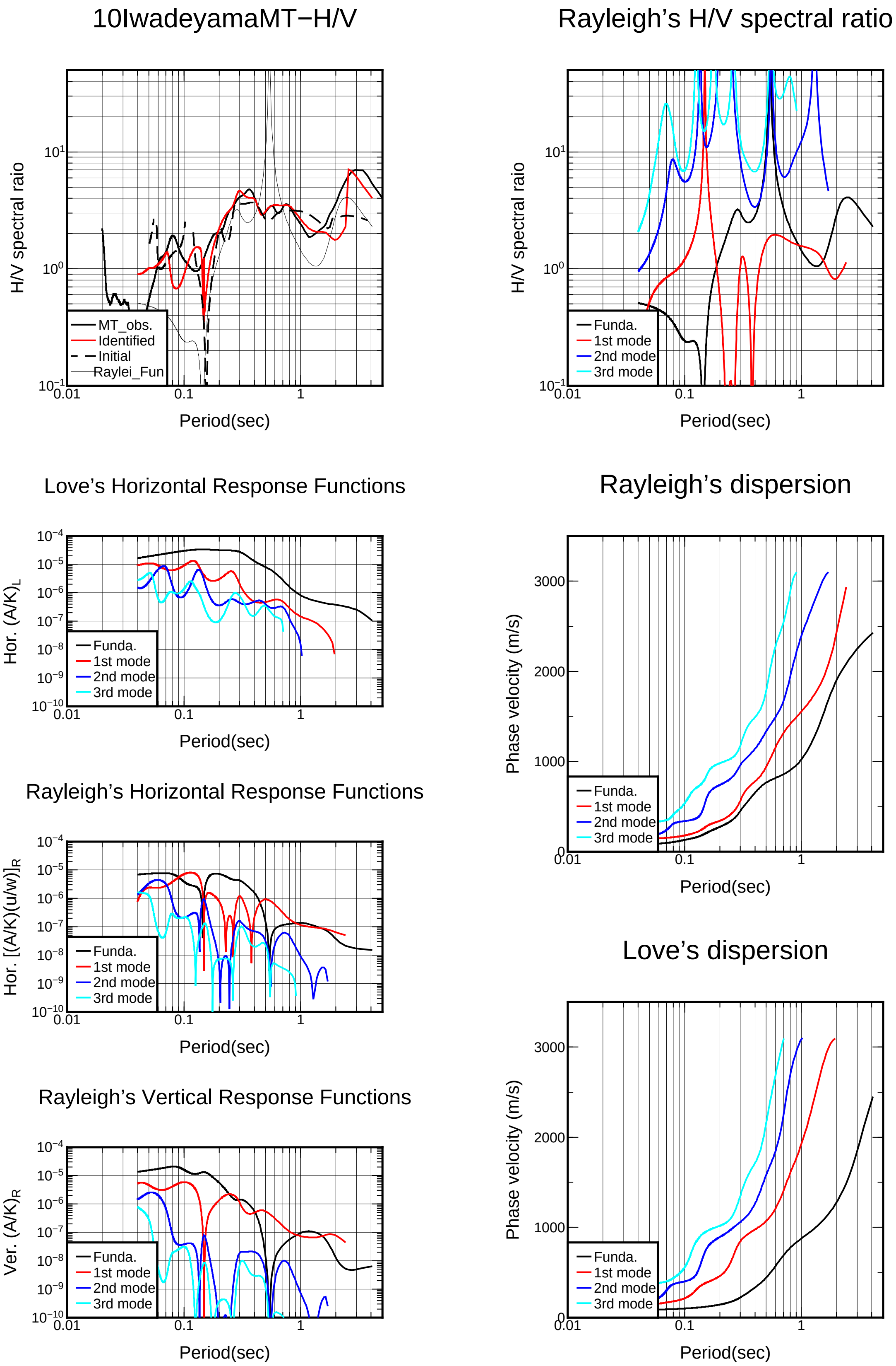
10IwadeyamaMT−H/V
H/V spectral raio
Period(sec)
MT_obs.
Identified
Initial
Raylei_Fun
Rayleigh's H/V spectral ratio
Love's Horizontal Response Functions
Hor. (A/K)L
Rayleigh's dispersion
Phase velocity (m/s)
Rayleigh's Horizontal Response Functions
Hor. [(A/K)(u/w)]R
Love's dispersion
Rayleigh's Vertical Response Functions
Ver. (A/K)R
Funda.
1st mode
2nd mode
3rd mode
0.01
0.1
1
1000
2000
3000

(i) Iwadeyama

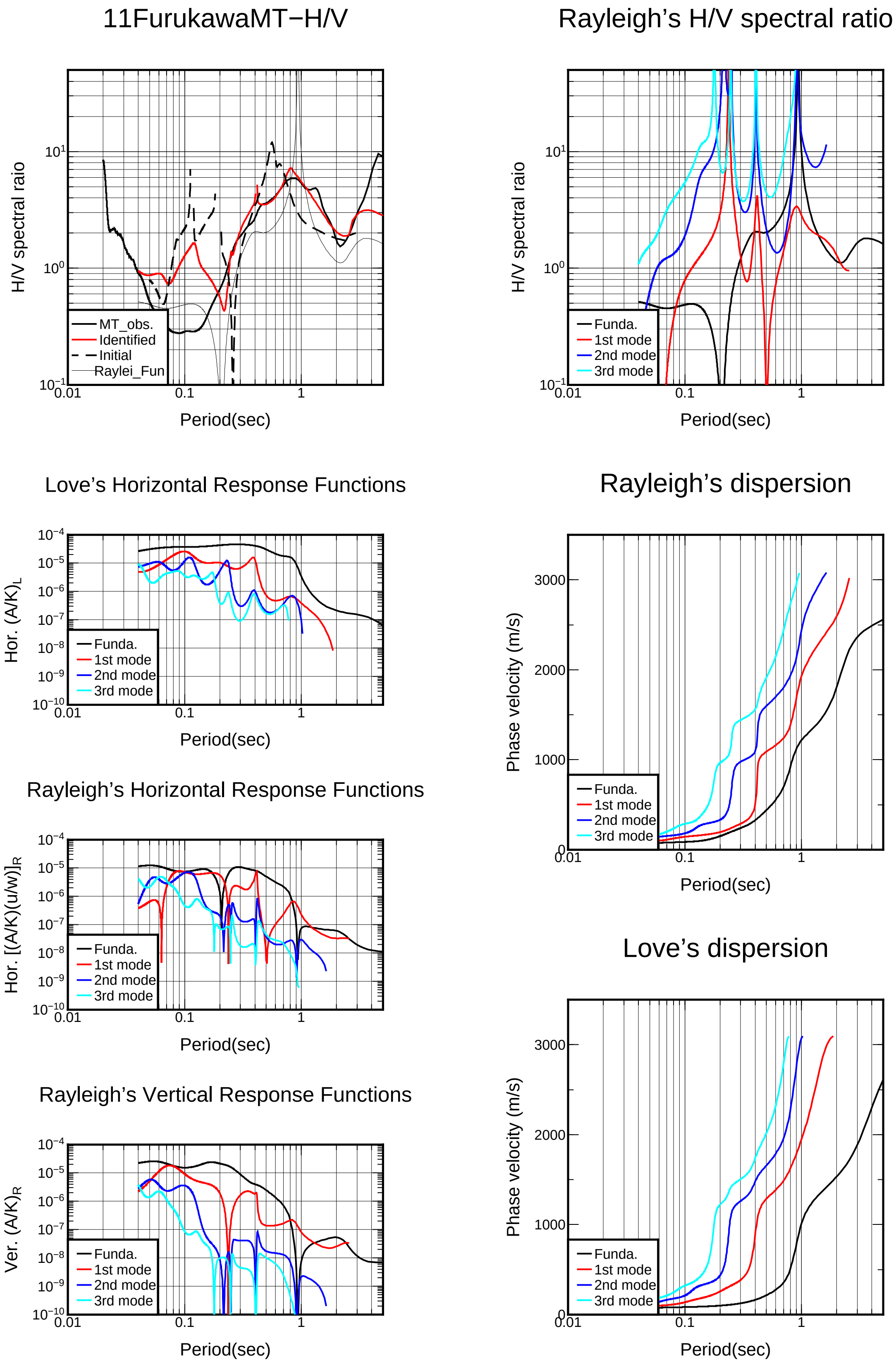
11FurukawaMT−H/V
H/V spectral raio
10¹
10⁰
10⁻¹
0.01
0.1
1
Period(sec)
MT_obs.
Identified
Initial
Raylei_Fun
Rayleigh's H/V spectral ratio
H/V spectral raio
Funda.
1st mode
2nd mode
3rd mode
Love's Horizontal Response Functions
Hor. (A/K)L
10⁻⁴
10⁻⁵
10⁻⁶
10⁻⁷
10⁻⁸
10⁻⁹
10⁻¹⁰
Rayleigh's Horizontal Response Functions
Hor. [(A/K)(u/w)]R
Rayleigh's Vertical Response Functions
Ver. (A/K)R
Rayleigh's dispersion
Phase velocity (m/s)
0
1000
2000
3000
Love's dispersion

(j) Furukawa

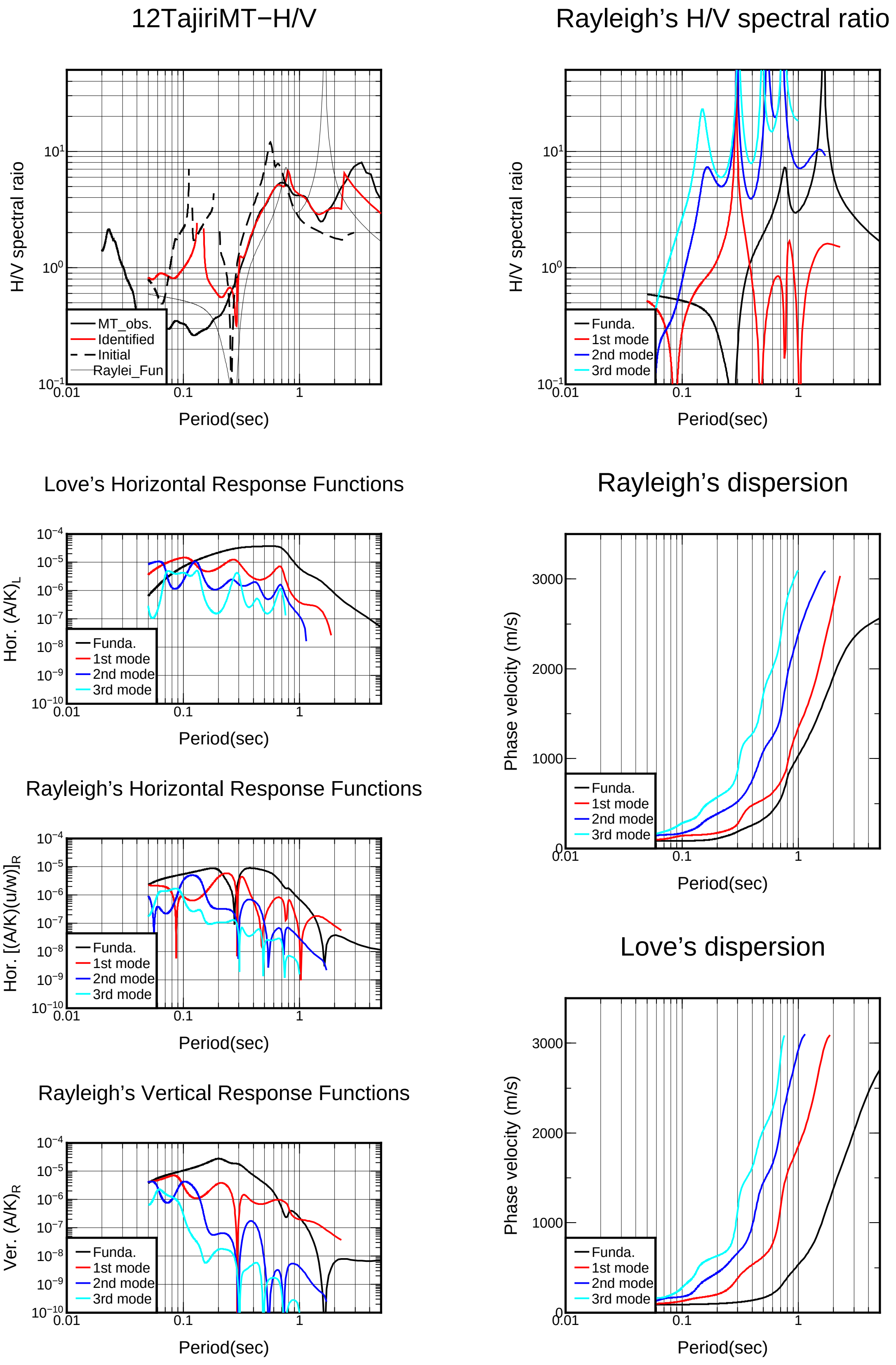
12TajiriMT−H/V
H/V spectral raio
Period(sec)
MT_obs.
Identified
Initial
Raylei_Fun
Rayleigh’s H/V spectral ratio
H/V spectral raio
Period(sec)
Funda.
1st mode
2nd mode
3rd mode
Love’s Horizontal Response Functions
Hor. (A/K)L
Period(sec)
Rayleigh’s dispersion
Phase velocity (m/s)
Period(sec)
Rayleigh’s Horizontal Response Functions
Hor. [(A/K)(u/w)]R
Period(sec)
Love’s dispersion
Phase velocity (m/s)
Period(sec)
Rayleigh’s Vertical Response Functions
Ver. (A/K)R
Period(sec)
0.01
0.1
1
10^1
10^0
10^-1
10^-4
10^-5
10^-6
10^-7
10^-8
10^-9
10^-10
0
1000
2000
3000

(k) Tajiri

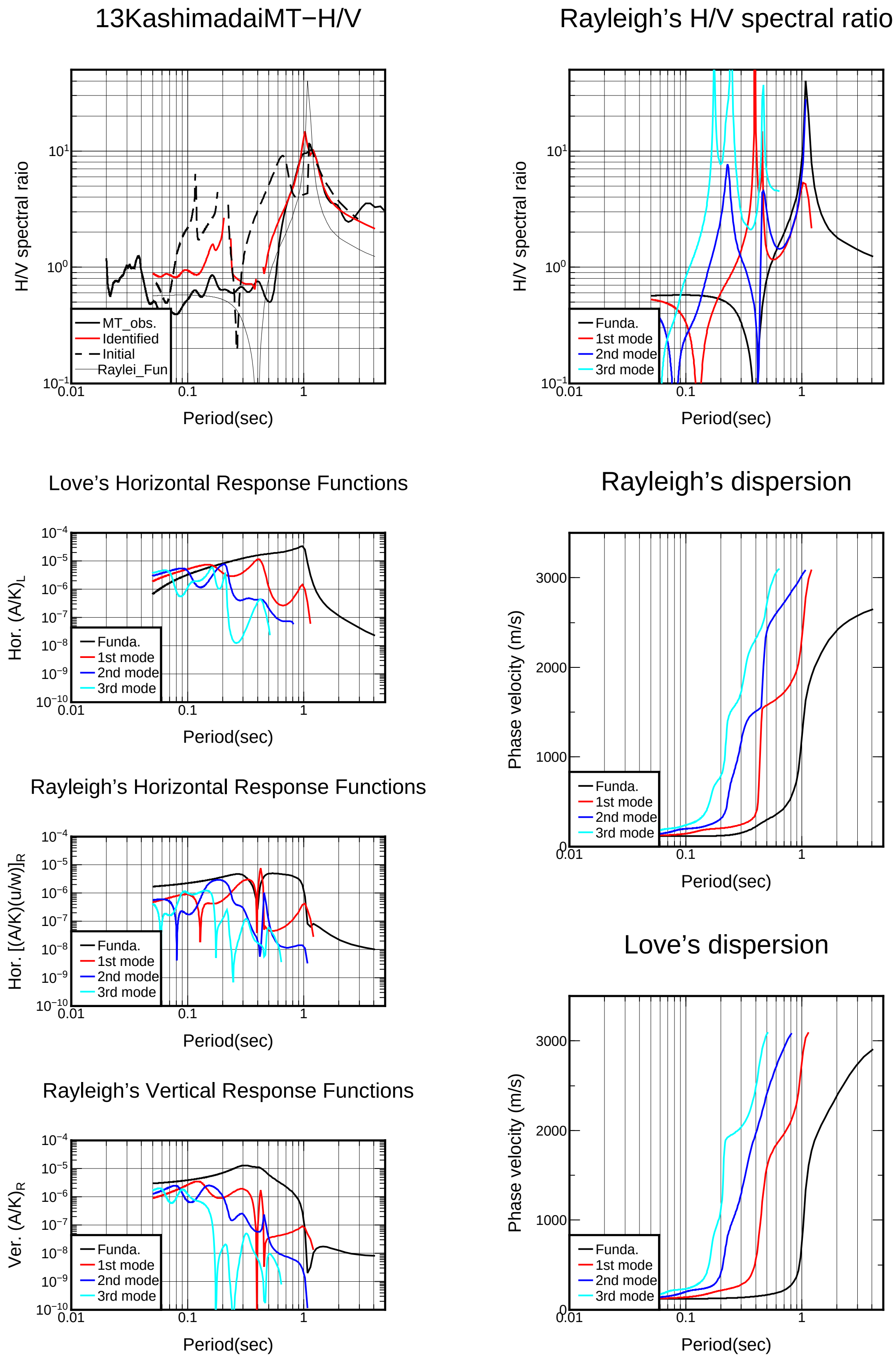

13KashimadaiMT−H/V

Rayleigh's H/V spectral ratio

Love's Horizontal Response Functions

Rayleigh's dispersion

Rayleigh's Horizontal Response Functions

Love's dispersion

Rayleigh's Vertical Response Functions

(l) Kashimadai

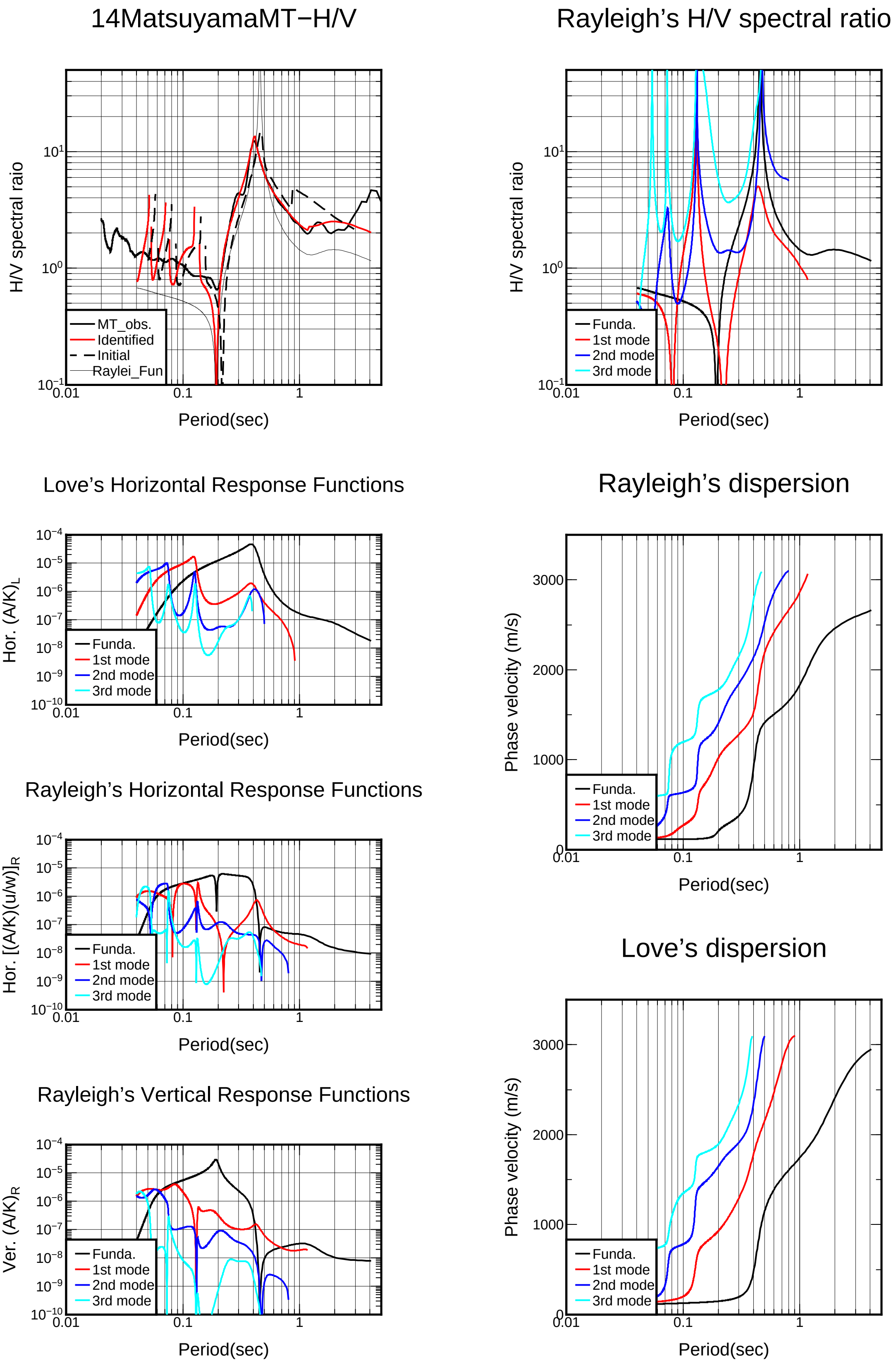
14MatsuyamaMT−H/V
H/V spectral raio
Period(sec)
MT_obs.
Identified
Initial
Raylei_Fun
Rayleigh’s H/V spectral ratio
Love’s Horizontal Response Functions
Hor. (A/K)L
Rayleigh’s dispersion
Phase velocity (m/s)
Rayleigh’s Horizontal Response Functions
Hor. [(A/K)(u/w)]R
Love’s dispersion
Rayleigh’s Vertical Response Functions
Ver. (A/K)R
Funda.
1st mode
2nd mode
3rd mode
0.01
0.1
1
10⁻¹
10⁰
10¹
10⁻¹⁰
10⁻⁹
10⁻⁸
10⁻⁷
10⁻⁶
10⁻⁵
10⁻⁴
0
1000
2000
3000

(m) Matsuyama

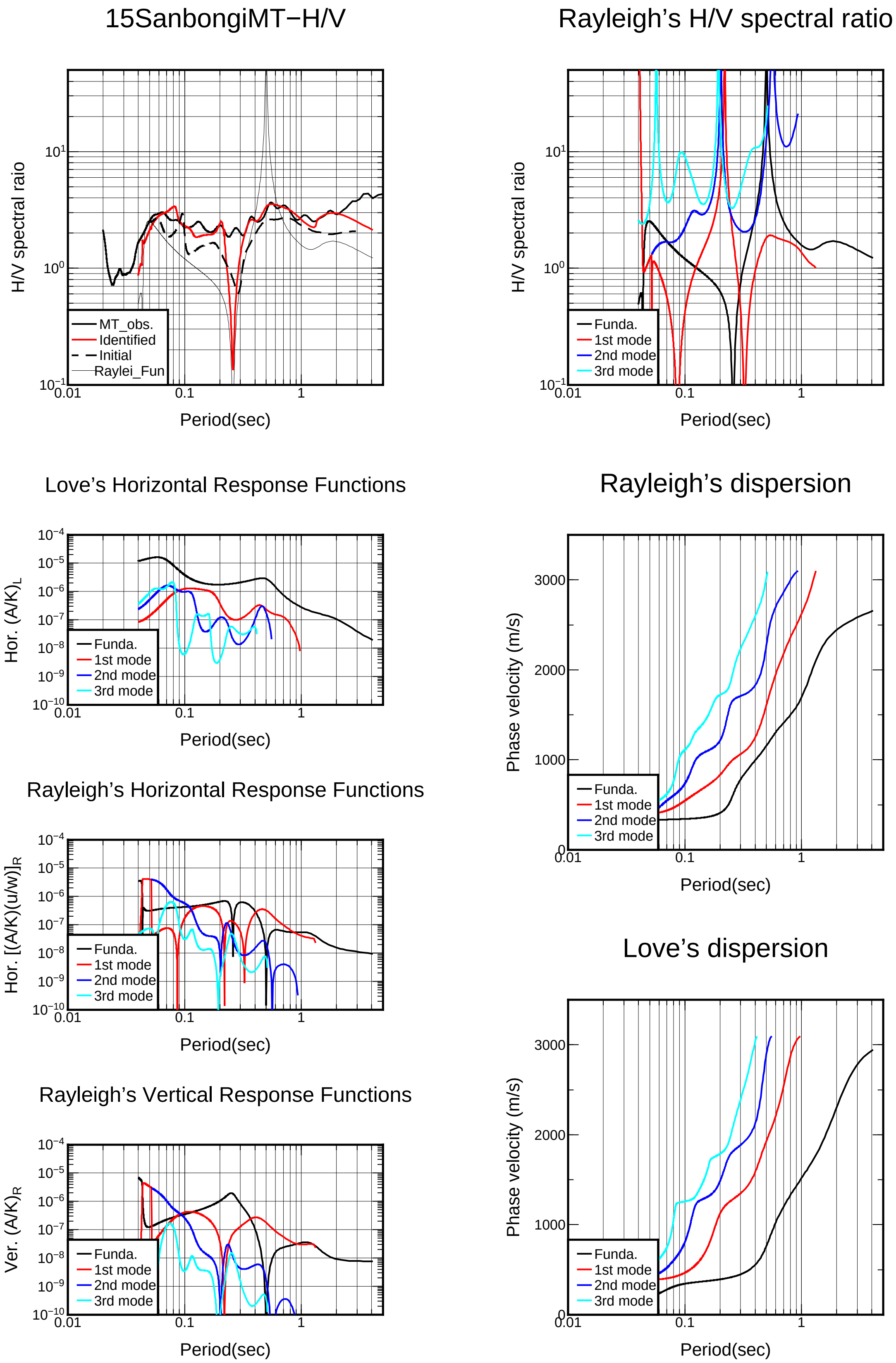
15SanbongiMT−H/V
H/V spectral raio
Period(sec)
MT_obs.
Identified
Initial
Raylei_Fun
Rayleigh’s H/V spectral ratio
H/V spectral raio
Period(sec)
Funda.
1st mode
2nd mode
3rd mode
Love’s Horizontal Response Functions
Hor. (A/K)L
Period(sec)
Rayleigh’s dispersion
Phase velocity (m/s)
Period(sec)
Rayleigh’s Horizontal Response Functions
Hor. [(A/K)(u/w)]R
Period(sec)
Love’s dispersion
Phase velocity (m/s)
Period(sec)
Rayleigh’s Vertical Response Functions
Ver. (A/K)R
Period(sec)
0.01
0.1
1
0
1000
2000
3000

(n) Sanbongi

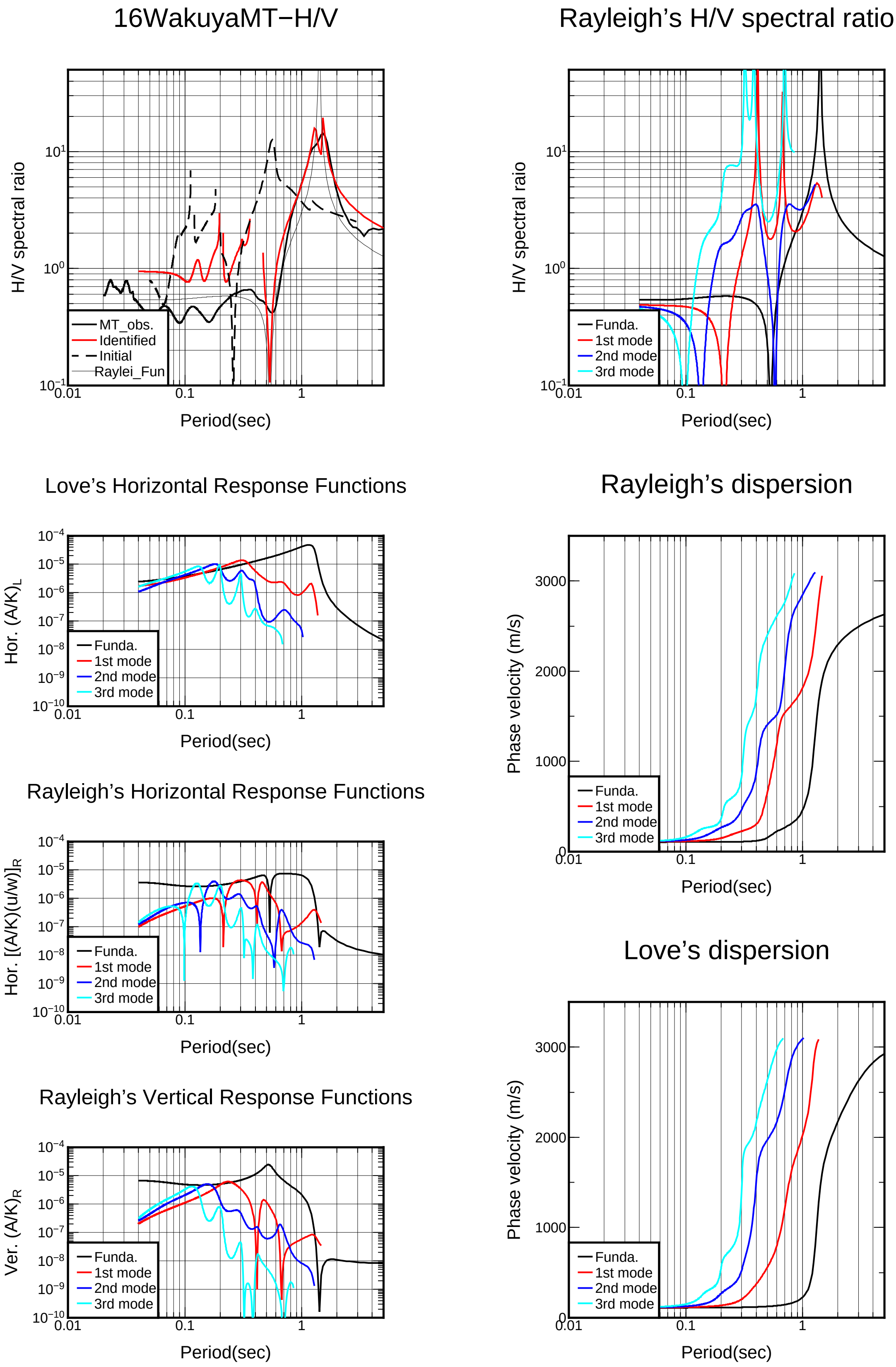
16WakuyaMT−H/V

Rayleigh's H/V spectral ratio

Love's Horizontal Response Functions

Rayleigh's dispersion

Rayleigh's Horizontal Response Functions

Love's dispersion

Rayleigh's Vertical Response Functions

(o) Wakuya

Fig. B.16 The dispersive curves and response functions of surface waves

Bibliography

AIJ (1996). Reconnaissance Report of Reinforced Concrete Buildings during the 1995 Hyogoken-Nanbu Earthquake. (in Japanese).

Aoi, S. (2000). New strong-motion observation network: KiK-net, *EOS Trans. Am. Geophys. Union* .

Arai, H. and Tokimatsu, K. (2000). Effects of Rayleigh and Love waves on microtremor H/V spectra, *Proc. 12th World Conf. on Earthquake Engineering*, pp. 2232–2240.

Arai, H. and Tokimatsu, K. (2004). S-wave velocity profiling by inversion of microtremor H/V spectrum, *Bulletin of the Seismological Society of America* **94**(1): 53–63.

Asano, K. and Iwata, T. (2012). Source model for strong ground motion generation in the frequency range 0.1–10 hz during the 2011 tohoku earthquake, *Earth, Planets, and Space* **64**: 1111–1123.

BRI (1996). Final Reconnaissance Report of the 1995 Hyogoken-Nanbu Earthquake. (in Japanese).

Ducellier, A., Kawase, H. and Matsushima, S. (2012). Velocity structure inversion from H/V spectral ratios of earthquake data: Application to the Tohoku region, Japan, *15th World Conference on Earthquake Engineering*.

Ducellier, A., Kawase, H. and Matsushima, S. (2013). Validation of a New Velocity Structure Inversion Method Based on Horizontal-to-Vertical (H/V) Spectral Ratios of Earthquake Motions in the Tohoku Area, Japan, *Bulletin of the Seismological Society of America* **103**(2A): 958–970.

Fäh, D., Kind, F. and Giardini, D. (2001). A theoretical investigation of average H/V ratios, *Geophysical Journal International* **145**(2): 535–549.

FDMA (2012). Fire and Disaster Management Agency. `http://www.fdma.go.jp/bn/higaihou_new.html`.

Fujimoto, K. and Midorikawa, S. (2006). Relationship between Average Shear-Wave Velocity and Site Amplification Inferred from Strong Motion Records at Nearby Station Pairs, *Journal of Japan Association for Earthquake Engineering* **6**(1): 11–22. (in Japanese with English abstract).

GSI (2012). Geospatial Information Authority of Japan. http://www.gsi.go.jp/.

Hasegawa, K. (1998). *Seismic risk mapping of buildings in large area using the grid-square statistics*, PhD thesis, Tokyo Institute of Technology. (in Japanese).

Hayashi, Y., Miyakoshi, J. and Tamura, K. (1997). Study on the distribution of peak ground velocity based on building damage during the 1995 Hyogo-Ken Nanbu Earthquake, *Journal of Structural and Construction Engineering, AIJ* **502**: 61–68. (in Japanese with English abstract).

Hayashi, Y., Miyakoshi, J., Tamura, K. and Kawase, H. (1997). Peak Ground Velocity Evaluated from Damage Ratio of Low-rise Buildings during the Hyogo-ken Nambu Earthquake of 1995, *Journal of Structural and Construction Engineering, Architectural Institute of Japan* **494**: 59–66. (in Japanese with English abstract).

Housner, G. W. (1952). Spectrum Intensities of Strong Motion Earthquakes , *Proceedings of the Symposium on Earthquake and Blast Effects on Structures*, Earthquake Engineering Research Institute,Los Angeles.

Ingber, L. (1989). Very fast simulated re-annealing, *Mathematical and computer modelling* **12**(8): 967–973.

Irikura, K. (1986). Prediction of strong acceleration motion using empirical Greenfs function, *Proc. 7th Japan Earthq. Eng. Symp*, pp. 151–156.

J-SHIS (2013). National Research Institute for Earth Science and Disaster Prevention. http://www.j-shis.bosai.go.jp/map.

JMA (1996). *On JMA Seismic Intensity – basic knowledge and its Application –*, Gyosei Incorporation. (in Japanese).

Kawabe, H., Kamae, K. and Uebayashi, H. (2012). Source modelling and strong ground motion simulation of the 2011 tohoku earthquake, *Proc. 15th World Conf. on Earthquake Engineering*.

Kawase, H. (1998). Metamorphosis of Near-Field Strong Motions by Underground Structures and Their Destructiveness to Man-made Structures – Learned from the

Damage Belt Formation during the Hyogo-ken Nanbu Earthquake of 1995 –, *Proceedings of the 10th Annual Meeting of Japan Association for Earthquake Engineering*, pp. 29–34. (in Japanese).

Kawase, H., Sánchez-Sesma, F. J. and Matsushima, S. (2011). The optimal use of horizontal-to-vertical spectral ratios of earthquake motions for velocity inversions based on diffuse-field theory for plane waves, *Bulletin of the Seismological Society of America* **101**(5): 2001–2014.

KenMap (2011). http://www5b.biglobe.ne.jp/t-kamada/CBuilder/kenmap.htm.

Kinki brach of AIJ (1995). The 1995 Hyogoken-Nanbu Earthquake–Damage of Wooden Houses–. (in Japanese).

Kinoshita, S. (1998). Kyoshin net K-NET, *Seismological Research Letters* **69**(4): 309–332.

Kitsunezaki, C., Goto, N., Kobayashi, Y., Ikawa, T., Horike, M., Salto, T., Kurota, T., Yamane, K. and Okuzumi, K. (1990). Estimation of P- and S- Wave Velocities in Deep Soil Deposits for Evaluating Ground Vibrations in Earthquake, **9**(3). (in Japanese with English abstract).

Konno, K. and Ohmachi, T. (1998). Ground-motion characteristics estimated from spectral ratio between horizontal and vertical components of microtremor, *Bulletin of the Seismological Society of America* **88**(1): 228–241.

Kurahashi, S. and Ikikura, K. (2013). Short-Period Source Model of the 2011 Mw9.0 Off the Pacific Coast of Tohoku Earthquake, *Bulletin of the Seismological Society of America* **103**(2B): 1373–1393.

Kurahashi, S. and Irikura, K. (2011). Source model for generating strong ground motions during the 2011 off the pacific coast of tohoku earthquake, *Earth, Planets and Space* **63**(7): 571–576.

Lachet, C. and Bard, P.-Y. (1994). Numerical and theoretical investigations on the possibilities and limitations of nakamura's technique, *Journal of Physics of the Earth* **42**(5): 377–397.

Lermo, J. and Chávez-García, F. J. (1993). Site effect evaluation using spectral ratios with only one station, *Bulletin of the Seismological Society of America* **83**(5): 1574–1594.

Midorikawa, S., Ito, Y. and Miura, H. (2011). Vulnerability Functions of Buildings based on Damage Survey Data of Earthquakes after the 1995 Kobe Earthquake, *Journal of Japan Association for Earthquake Engineering* **11**(4). (in Japanese with an English abstract).

Miyakoshi, J. and Hayashi, Y. (2000). Correlation of Building Damage with Indices of Seismic Ground Motion Intensity During the 1999 Chi-Chi, Taiwan earthquake, *Proceedings of the International Workshop on Annual Commemoration of Chi-Chi Earthquake*, pp. 18–20.

Miyakoshi, J., Hayashi, Y., Tamura, K. and Fukuwa, N. (1997). Damage ratio functions of buildings using damage data of the 1995 Hyogo-Ken Nanbu earthquake, *Proceeding of International Conference on Structural Safety and Reliability*, Vol. 1, pp. 349–354.

Motosaka, M. and Tsamba, T. (2011). Investigation of High Acceleration Records at K-NET Tsukidate Station During the 2011 off the Pacific Coast Tohoku Earthquake, *Proceedings of the 8th Annual Meeting of Japan Association for Earthquake Engineering*, pp. 24–25.

Muraibo, K., Takino, A., Murakami, M., Nakaji, H., Suzuki, S. and Ooka, Y. (2011). Field survey of building damage during the 2011 off the pacific coast of Tohoku Earthquake, *Proceedings of the 8th Annual Meeting of Japan Association for Earthquake Engineering*, pp. 70–71. (in Japanese with an English abstract).

Murao, O. (1999). *Study on Building Damage Estimation based on the Actual Data due to the 1995 Hyogoken Nanbu Earthquake*, PhD thesis, University of Tokyo. (in Japanese).

Nakamura, Y. (1989). A method for dynamic characteristics estimation of subsurface using microtremor on the ground surface, *Railway Technical Research Institute, Quarterly Reports* **30**(1).

Nakamura, Y. (2000). Clear identification of fundamental idea of Nakamurafs technique and its applications, *Proceedings of the 12th world conference on earthquake engineering*, Auckland New Zealand.

NIED (2012). National Research Institute for Earth Science and Disaster Prevention. `http://www.kyoshin.bosai.go.jp/kyoshin/`.

Nishi, H. (2012). Damage on hazardous materials facilities, *Proceedings of the international symposium on engineering lessons learned from the 2011 Great East Japan Earthquake*.

Okada, H. and Suto, K. (2003). *The microtremor survey method*, Vol. 12, Society of Exploration Geophysicists with the cooperation of Society of Exploration Geophysicists of Japan [and] Australian Society of Exploration Geophysicists.

Okada, S. and Kagami, H. (1991). Inventory Vulnerability Functions for Earthquake Damage Evaluation in Terms of Intensity Scale of the Japan Meteorological Agency, **44**(2). (in Japanese with English abstract).

Phinney, R. A. (1964). Structure of the Earth's crust from spectral behavior of long-period body waves, *Journal of Geophysical Research* **69**(14): 2997–3017.

Saguchi, K., Masaki, K. and Irikura, K. (2009). Estimation of strong motions on free rock surface-Identification of Soil Structures and Strong Motions on Free Rock Surface in Kashiwazaki-Kariwa Nuclear Power Plant During the 2007 Niigataken Chuetsu-Oki Earthquake. (in Japanese with English abstract).

Sánchez-Sesma, F. J., Rodríguez, M., Iturrarán-Viveros, U., Luzón, F., Campillo, M., Margerin, L., García-Jerez, A., Suarez, M., Santoyo, M. A. and Rodríguez-Castellanos, A. (2011). A theory for microtremor H/V spectral ratio: application for a layered medium, *Geophysical Journal International* **186**(1): 221–225.

Satoh, T. (2006). Inversion of Qs of deep sediments from surface-to-borehole spectral ratios considering obliquely incident SH and SV waves, *Bulletin of the Seismological Society of America* **96**(3): 943–956.

Satoh, T., Kawase, H. and Matsushima, S. (2001). Differences between site characteristics obtained from microtremors, S-waves, P-waves, and Codas, *Bulletin of the Seismological Society of America* **91**(2): 313–334.

STAT (2012). Statistics Japan. `http://www.stat.go.jp/`.

Tobita, K., Kawase, H. and Matsushima, S. (2012). A study on the estimation method for underground structure using microtremors and its application to the osaka plain, *Proc. 15th World Conf. on Earthquake Engineering*.

Tokimatsu, K. and Miyadera, Y. (1992). Characteristics of Rayleigh waves in microtremors and their relation to underground structures, *J. Struct. Constr. Eng. Trans. Architectural Inst. Japan* **439**: 81–87. (in Japanese).

Tong, H., Yamazaki, F., Sasaki, H. and Matsumoto, S. (1994). A relationship between seismic ground motion severity and house damage ratio, *9th symposium of Japan Association for Earthquake Engineering*. (in Japanese with English abstract).

Wakamatsu, K., Matsuoka, M., Kubo, S., Hasegawa, K. and Sugiura, M. (2004). Development of GIS-Based Japan Engineering Geomorphologic Classification Map, *Proceedings-Japan Society Of Civil Engineers*, Dotoku Gakkai, pp. 213–232. (in Japanese with English abstract).

Wang, X., Masaki, K. and Irikura, K. (2011). Building damage criteria from strong ground Motion characteristics during the 2008 Wenchuan Earthquake, *Journal of Earthquake Engineering* **15**(7): 1117–1137.

Wessel, P. and Smith, W. H. (1998). New, improved version of Generic Mapping Tools released, *Eos, Transactions American Geophysical Union* **79**(47): 579–579.

Wu, Hao, Masaki, K., Irikura, K., Saguchi, K., Kurahashi, S. and Wang, X. (2012). Relationship between Builidng Damage Ratios and Ground Motion Characteristics during the 2011 Tohoku Earthquake, *Journal of Natural Disaster Science* **34**(1): 59–78.

Wu, Yih-Min, Hsiao, N.-C., Teng, T.-L. and Shin, T.-C. (2002). Near Real-time Seismic Damage Assessment of the Rapid Reporting System, *Terrestrial Atmospheric and Oceanic Sciences* **13**(3): 313–324.

Yamaguchi, N. and Yamazaki, F. (1999). Estimation of strong ground motion in the 1995 Hyogoken-Nanbu Earthquake based on building damage data, *Proceedings-Japan Society of Civil Engineers*, pp. 325–336. (in Japanese with an English abstract).

Yamaguchi, N. and Yamazaki, F. (2000). Fragility curves for buildings in Japan based on damage surveys after the 1995 Kobe earthquake, *Proceedings of the 12th conference on earthquake engineering, Auckland, New Zealand.*

Yoshida, H. and Kobayashi, K. (2002). Relationship between Qp and Qs Values in Sedimentary Layers , *Summaries of Technical Papers of Annual Meeting, Architectrual Institute of Japan*, pp. 183–184. (in Japanese).